UNIVERSITÉ DE STRASBOURG

ÉCOLE DOCTORALE : ED182

[UMR 7504]

THÈSE présentée par :

Sayali Ganesh SHEVATE soutenue le :

04 Fevrier 2021

pour obtenir le grade de : **Docteur de l'université de Strasbourg**

Discipline/Spécialité : Physics

Preparation and Rydberg excitation of large arrays of microscopic atomic ensembles

THÈSE dirigée par :

M. WHITLOCK Shannon	Professeur, Université de Strasbourg

RAPPORTEURS :

M. BROWAEYS Antoine	Professeur, Institut d'Optique, Palaiseau
M. GERRITSMA Rene	Professeur, Van der Waals-Zeeman Instituut, Amsterdam

---

AUTRES MEMBRES DU JURY :

Mme. HUELGA Susana	Professeur, University of Ulm
M. PUPILLO Guido	Professeur, Université de Strasbourg

Preparation and Rydberg excitation of large arrays of microscopic atomic ensembles

Abstract :

Ultracold atoms in optical tweezer arrays have emerged as one of the most versatile platforms for quantum many-body physics, quantum simulation and quantum computation. In this thesis, I report a way to achieve fully occupied tweezer arrays to sizes well beyond 200 sites by exploiting elastic collisions as compared to light-assisted inelastic collisions and along the way greatly advance the feasibility of quantum simulations based on trapped atomic ensembles with programmable geometries. We demonstrate, for the first time, fully filled versatile arrays of atomic ensembles > 400 tweezers prepared using a digital micromirror device, where each tweezer contains ~ 60 atoms in a microscopic volume, high atom number and remarkably low atom number fluctuations. As a necessary pre-requisite to performing the coherent manipulation of the Rydberg excitation of these atomic ensembles, I present experiments on narrow linewidth two-photon Rydberg excitation of these large arrays of atomic ensembles. I also discuss an analysis of the effects causing spectral broadening. This work paves the way towards detailed analysis of many-body effects in a structured Rydberg gas-an important step towards building a quantum simulator based on trapped atomic ensembles in optical tweezer arrays. This opens up applications ranging from quantum simulation of exotic quantum spin models, quantum dynamics including transport and many-body localization and quantum cellular automata with programmable spatial configurations and versatile Rydberg mediated interactions.

Preparation and Rydberg excitation of large arrays of microscopic atomic ensembles

Résumé :

Des atomes froids dans des réseaux de pinces optiques sont apparus comme l'un des plates-formes les plus polyvalent es pour la physique quantique à N-corps, la simulation et l'informatique quantiques. Dans cette thèse, je rapporte un moyen de réaliser des réseaux de pièges optiques occupés uniformément, de tailles bien supérieures à ~200 sites, en utilisant des collisions élastiques par opposition aux collisions inélastiques assistées par la lumière et je fais progresser considérablement la faisabilité des qubits basés sur des ensembles atomiques piégés. Nous démontrons, pour la première fois, des réseaux polyvalents entièrement remplis d'ensembles atomiques de plus de 400 pièges optiques préparés à l'aide d'une matrice de micro-miroirs, où piège microscopiques contient ~60 atomes, un nombre d'atomes élevé et des fluctuations étonnamment faibles du nombre d'atomes. En utilisant des atomes de Rydberg en forte interaction, j'étudie la dynamique d'excitation de Rydberg et les interactions à longue distance dans les grands réseaux d'ensembles atomiques. Cela ouvre la voie à la réalisation de simulateurs quantiques basés sur des ensembles atomiques.

Mot-clés : atomes-froids, Rydberg, la physique quantique à N-corps, simulateurs quantiques, ensembles atomiques, pinces optiques

Acknowledgments

My biggest thanks to my advisor Prof. Shannon Whitlock for an amazing encouragement during the three years of my PhD and especially for his tremendous patience towards my learning of our complex experiment. Besides that, I owe him my love for a nice summer barbeque and a beer :).

I would like to thank Prof. Antoine Browaeys and Prof. Rene Gerritsma for kindly agreeing to be the referees of my thesis. I also convey my thanks to my committee members Prof. Susana Huelga and Prof. Guido Pupillo.

To my amazing colleague Dr. Yibo Wang who joined the group as a Post-Doc at the same time when I joined as a PhD student, who supported me all along and tolerated my unending series of questions, scientific arguments in the lab and infinite fruitful discussions, I owe a big thank you.

To Dr. Graham Lochead, my another amazing colleague, who suffered reading my thesis (Yibo did too), I owe a great thanks for all the cheerful discussions about science, politics, English literature, India, England, his failed attempts of trying to speak Hindi :D and for his nice bicycle which I have been using for a year to go to Kehl for groceries and for long rides :).

To Tobias, for introducing me to the German dish 'Maultaschen' and to Manuel for some fierce arguments :), thanks to both of you. My other colleagues Dr. Alda Arias and Dr. Stephan Helmrich with whom I had a short overlapping period of my PhD, I thank them for introducing me to the labs in Heidelberg.

To Mme Corinne Ledger, for helping me out with all the administrative glitches and making my life easier in bureaucratic France, I owe a big thanks as well.

My friends Gunther, Erika, Filipa, Rogéria, Yoseline, Guido, David, Michi, Ye,

Bleuenn and Jérome and many others with whom I spent a super nice time here in Strasbourg and built many nice memories which I will take along with me in my next endeavours.

In the end, I would like to convey my special thanks to my parents and my brother who listened to all my worries and my frustrations and cheered me up to stand-up again and lead the life with greater strength. I acknowledge my whole family and my friends for their love and care throughout my life. I thank Strasbourg for being a cheerful, happy place - a second home after all.

List of publications

The results presented in this thesis have led to the following manuscripts and peer-reviewed publications, which have been written and published during the course of my doctoral studies:

Preparation of hundreds of microscopic atomic ensembles in optical tweezer arrays
Y. Wang, S. Shevate, T. M. Wintermantel, M. Morgado, G. Lochead, and S. Whitlock
npj Quantum Information 6, 54 (2020).

Unitary and non-unitary quantum cellular automata with Rydberg arrays
T. M. Wintermantel, Y. Wang, G. Lochead, S. Shevate, G. K. Brennen, S. Whitlock
Phys. Rev. Lett. 124, 070503 (2020).

Epidemic growth and Griffiths effects on an emergent network of excited atoms
T. M. Wintermantel, M. Buchhold, S. Shevate, M. Morgado, Y. Wang, G. Lochead, S. Diehl, S. Whitlock
arXiv:2007.07697 (2020) (accepted in **Nature Communications**)

Résumé en Français

Richard Feynman a fait cette remarque célèbre en 1980 : ”La nature n'est pas classique, bon sang , et si vous voulez faire une simulation de la nature, vous feriez mieux de la faire avec la mécanique quantique et c'est un merveilleux problème, car il ne semble pas si facile”. Peu de temps après, il est devenu possible de concevoir des systèmes quantiques en laboratoire qui permettent de saisir la caractéristique essentielle du véritable corps complexe multiple des systèmes quantiques espérant observer et étudier de nouvelles propriétés émergentes dans des conditions expérimentales contrôlables. C'est un défi parce que le comportement collectif émergeant du système ne découle pas nécessairement des caractéristiques sous-jacentes de ses éléments constitutifs. Par exemple, pourquoi la dynamique quantique collective et les nouveaux phénomènes tels que la superfluidité [1–3] et la supraconductivité [4–7], se produisent dans certains matériaux à des températures assez basses est encore un défi majeur à expliquer de manière satisfaisante ?

Une étude approfondie des origines de ces effets aiderait à concevoir de nouveaux matériaux présentant les propriétés souhaitées et éventuellement de nouveaux effets physiques. Mais les méthodes conventionnelles de construction, les modèles théoriques permettant d'étudier cette physique pertinente sont limités en raison de l'échelle de la complexité avec le nombre croissant de particules et leurs degrés de liberté. Pour surmonter ce problème, des efforts considérables ont été déployés vers l'approche de la simulation quantique [8, 9]. L'objectif des simulations quantiques consiste à imiter le plus fidèlement possible l'Hamiltonien d'un système cible. Cela souligne la nécessité de développer des systèmes quantiques contrôlables/programmables systèmes. Cela permet d'étudier et de mesurer les paramètres du système dans un environnement plus contrôlé dans un laboratoire [10].

L'approche de la simulation quantique est appelée à devenir un outil indispensable pour acquérir de nouvelles connaissances dans le large spectre des études compliquées, des problèmes réels de nombreux corps dans divers domaines, en intégrant des condensés la physique de la matière, la chimie, la physique nucléaire et des hautes énergies, la physique atomique, la chimie quantique et la cosmologie, etc. [10]. Au cours des dernières décennies, de nombreux systèmes

ont été étudiés, allant des ions [11] aux photons [12], en passant par les atomes ultrafroids de réseaux optiques [13], les circuits supraconducteurs [14] et les réseaux de Rydberg [15].

Cette thèse porte sur les atomes ultrafroids piégés, car il est prouvé qu'ils constituent un stade idéal pour la simulation quantique [16] avec le haut degré de contrôle sur ces systèmes et une grande variété de physique qui est explorée, par exemple l'unité Gaz Fermi dans le croisement BCS-BEC [17–21], systèmes Bose-Hubbard [22–24], Transition BKT [25–27] et gaz Tonks-Girardeau [28, 29].

Grands réseaux d'atomes ultrafroids

Avec les techniques de refroidissement et de piégeage par laser [30], un grand niveau de contrôle a été réalisé sur les propriétés de l'état de base des atomes ultrafroids englobant le mouvement des atomes, la géométrie spatiale flexible, l'isolation de l'environnement, le temps de cohérence long et les propriétés d'interaction [31]. Le site le confinement spatial d'atomes de géométries différentes en 1D, 2D et 3D a été atteint avec certains degrés de désordre en utilisant des réseaux optiques [13] et pincettes [32–34]. Les atomes neutres des réseaux de pincettes optiques en particulier ont émergé comme l'une des plateformes les plus polyvalentes pour la physique quantique à plusieurs corps, la simulation et l'informatique quantiques [32, 35–43]. Les raisons principales sont la plus grande extensibilité, le long temps de cohérence, l'adressabilité d'un seul site et des interactions contrôlables en utilisant des états de Rydberg très excités [44–50].

Quelques exemples d'atomes neutres piégés optiquement dans des réseaux de pincettes programmables sont présentés dans la figure 0.1 extraite de [15]. À ce jour, d'importants efforts expérimentaux ont été consacrés à la création de réseaux atomiques entièrement occupés avec 1 atome dans chaque pincette en exploitant les collisions inélastiques assistées par la lumière [53–55] et le réaménagement pour remplir les sites vides [32, 33, 38, 52, 56, 57]. Jusqu'à présent, cependant, les tailles de réseaux réalisables sont limitées à ~ 200 [58] sites entièrement occupés (y compris pour les systèmes 2D et 3D), en partie en raison des besoins élevés en énergie par pince le piège et la complexité croissante associés au processus de réarrangement pour les grands tableaux [33,

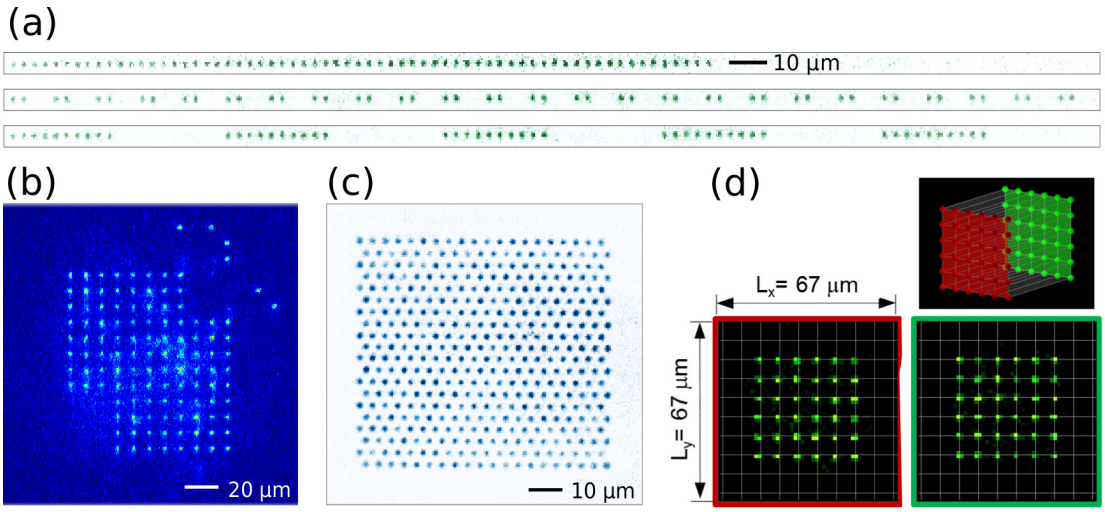

Fig. 0.1: Exemples d'atomes neutres piégés optiquement dans des réseaux de pincettes programmables (reproduit à partir de [15]). **(a)** Images de fluorescence de réseaux unidimensionnels chargés de façon déterministe contenant plus de 50 atomes dans des géométries périodiques, dimérisées et en grappes. Reproduit de [32]. **(b)** Image de fluorescence d'un réseau carré bidimensionnel chargé de façon déterministe, comportant 111 atomes. Reproduit de [33]. **(c)** Image d'absorption d'un réseau triangulaire d'ensembles atomiques microscopiques contenant plus de 400 sites. Reproduit de [51]. **(d)** Image de fluorescence d'un réseau bicouche chargé de façon déterministe de 72 sites. Reproduit de [52].

52, 57]. Au cours de cette thèse, une réalisation majeure a été une autre approche pour surmonter ce défi de l'extensibilité en démontrant la préparation de grands ensembles de centaines de pincettes optiques à remplissage uniforme avec un grand nombre d'occupations en une seule étape (par rapport à un seul atome) et faire progresser considérablement la faisabilité des qubits basés sur des ensembles atomiques [51].

Les atomes de Rydberg pour la simulation quantique

L'interaction dominante régissant la dynamique induite par les électrons dans les matériaux réels sont des interactions de type Coulomb qui s'étendent sur de grandes distances [59]. Par conséquent, il est évident que la simulation quantique doit imiter une telle distance des interactions aussi proches que possible des matériaux naturels réels. Il y a eu des efforts de certaines plateformes atomiques et moléculaires pour la simulation des interactions telles que les espèces atomiques magnétiques, à savoir l'Erbium, le Chromium et le Dysprosium [60–62] qui présentent des interactions dipôle-dipôle magnétiques. Une autre plateforme utilise des molécules polaires à l'état de traces qui interagissent par la dynamique dipolaire déphasante collective [63–67].

Mais l'excitation des atomes de Rydberg Ultrafroids présente des avantages (par rapport à ces autres particules qui interagissent à longue distance) qui sont des interactions adaptables en termes de force et de signe, ainsi que la mise en pause complète du système d'excitation, ce qui le rend plus flexible que d'autres approches. Les atomes de Rydberg démontrent de fortes interactions Van der Waals qui perpétuent bien au-delà des distances interatomes typiques Cela donne lieu à d'intéressants phénomènes collectifs tels que le blocus de Rydberg [68–71]. Dans le blocus, les interactions suppriment les excitations, permettant au maximum une seule excitation dans un rayon de blocage partagé collectivement par tous les atomes dans le volume sur le blocus [72]. Ceci a été utilisé dans l'information quantique pour réaliser des états enchevêtrés adressables [68, 69, 73–75], pour générer de nouvelles phases de la matière [76–83] et pour simuler les effets magnétiques [84–87]. En combinant des atomes de Rydberg [49, 69, 88–93], ces systèmes atomiques piégés ont été récemment utilisées pour démontrer une dynamique quantique cohérente allant jusqu'à 51 qubits [94] et des états enchevêtrés jusqu'à 20 qubits dans une chaîne unidimensionnelle (1D) [95].

Aperçu de la thèse

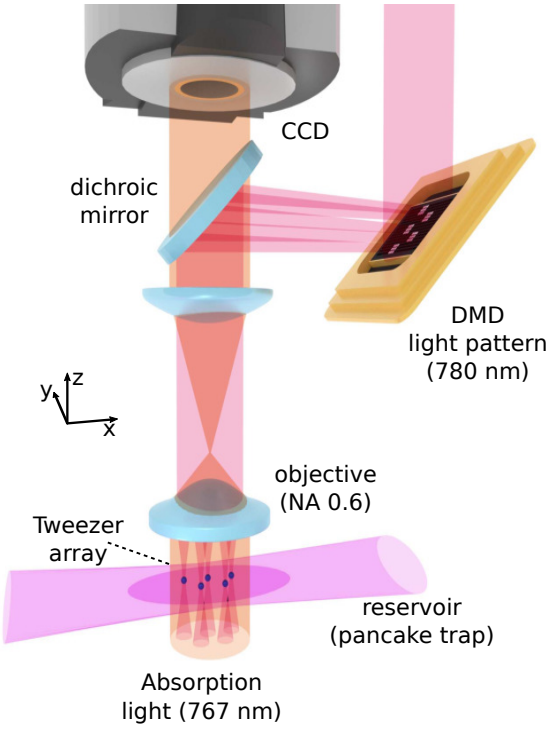

Fig. 0.2: Schéma de l'installation de notre laboratoire à Strasbourg utilisée pour produire et charger les réseaux de pincettes en projetant la lumière d'un dispositif numérique à micromiroirs directement sur les atomes confinés dans un piège à réservoir optique (reproduite de [51]).

Dans cette thèse, je me concentre sur une mise à niveau substantielle de notre système atomique ultrafroid actuel, plate-forme expérimentale impliquant la génération de grands réseaux d'ensembles atomiques piégés (voir la figure 0.2 reproduite de [51])]).

Notre approche consiste à préparer des réseaux polyvalents d'ensembles atomiques en les transférant d'un piège optique à dipôle en forme de crêpe à un réseau de pinces optiques créée par projection directe de motifs lumineux produits par un dispositif numérique à micro-miroirs [51]). La taille de chaque ensemble est inférieure à celle du Rayon du blocus de Rydberg, de sorte que chacun peut transporter soit 0 ou 1 excitations (collectives) qui peuvent alors fortement interagir avec les ensembles voisins. Cela en fait une plateforme prometteuse pour réaliser l'expérience des super-atomes de Rydberg exprimant une haute fidélité d'excitation Rydberg unique par micropiège. Dans un premier temps, il fournit une stratégie pour réaliser potentiellement des milliers de qubits atomiques pour l'application de la simulation quantique. Je présente ensuite le schéma d'excitation Rydberg à deux photons et le système Rydberg

que nous utilisons pour l'excitation Rydberg de ces atomes des ensembles.

Je discute des résultats des expériences sur la largeur de ligne étroite Rydberg l'excitation de l'ensemble des ensembles atomiques et décrire la compréhension des mécanismes d'élargissement tels que l'élargissement Doppler, l'élargissement de la puissance et l'inhomogénéité du faisceau laser d'excitation qui pourrait éventuellement élargir la largeur spectrale de la transition de Rydberg. Plus tard, comme perspective, je discute de certaines applications potentielles de l'utilisation de la plateforme Rydberg présentées dans cette thèse qui sont (1) la simulation quantique de type Förster transport d'excitation (entre les sites de pinces bloqués du Ryberg), (2) une expérience réalisation mentale d'automates cellulaires quantiques (QCA) [96], (3) Démonstration de la dynamique de facilitation dans l'ensemble des pièges à pince pour étudier les effets de troubles comme récemment étudiés expérimentalement dans notre groupe dans un milieu atomique ultrafroid [97].

La structure de cette thèse est la suivante :
le chapitre 1 donne une introduction à la plate-forme de grands réseaux d'atomes ultrafroids et un aperçu des récentes études de systèmes à plusieurs corps utilisant des atomes de Rydberg ultrafroids.

Le Chapitre 2 développe une partie du cadre théorique des pièges à dipôle optique, à savoir nécessaire à la construction de grands réseaux de pièges à pince et aussi comprennent les propriétés importantes des atomes de Rydberg nécessaires pour comprendre les effets de l'interaction Rydberg-Rydberg entre les pièges à pince.

Le Chapitre 3 concerne la caractérisation de l'intégration du micro-miroir numérique (DMD) dans notre appareil atomique ultra froid existant de 39 K pour générer des centaines de pinces optiques piègeant les potentiels et présentant les géométries exotiques de pièges à pincettes.

Le chapitre 4 décrit une étape expérimentale de la réalisation de grands réseaux d'ensembles atomiques avec plus de 400 sites et décrit également la caractérisation de cette approche. Veuillez vous référer à la figure 0.3.

Le chapitre 5 décrit les résultats récents de l'excitation Rydberg à deux photons

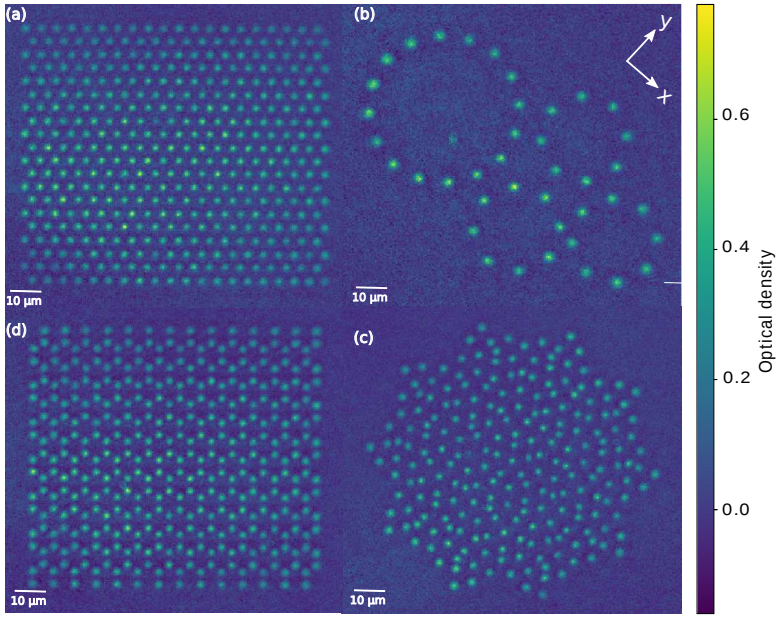

Fig. 0.3: Réalisation de grands réseaux de pincettes avec un grand nombre d'occupation dans chaque pincette. (a) Image expérimentale d'absorption d'un réseau triangulaire de 400 sites, où chaque point correspond à un ensemble microscopique d'atomes $\approx$ 30 ultracold ^{39}K. L'espacement entre les treillis est de 4 µm et la taille apparente de chaque point est de 0.75 µm (rayon de 1.5 µm), principalement limité par le flou du recul pendant l'imagerie. (b) Structure annulaire à 40 sites (c) Réseau quasi-cristallin de Penrose à 226 sites. Pour améliorer le rapport signal/bruit, chaque image est une moyenne de 20 images d'absorption (d) réseau alvéolaire de 196 sites (voir figure 4.3 a pour une image typique en une seule prise).

de ces ensembles atomiques présentant le spectre d'excitation Rydberg à largeur de raie étroite et présente une analyse des mécanismes qui peuvent contribuer à l'élargissement de la largeur spectrale.

Enfin, le chapitre 6 présente les remarques finales résumant la thèse et présente une perspective d'utilisation de cette plateforme polyvalente de grands réseaux de Rydberg atomique pour étudier la dynamique quantique à plusieurs corps dans les domaines quantiques et classiques pour concevoir des états quantiques fortement enchevêtrés et pour parvenir à une approche du traitement et de l'informatique quantique de l'information quantique.

Améliorations possibles du dispositif expérimental actuel

Afin d'obtenir une excitation Rydberg de faible largeur, les améliorations telles que l'utilisation d'un faisceau d'excitation à sommet plat avec une intensité uniforme dans sa section transversale pourraient être utiles pour obtenir un couplage Rabi uniforme subi par les atomes dans la section transversale du faisceau. En outre, la température des ensembles atomiques devrait être réduite à $\sim 2\ \mu$k pour obtenir une largeur de raie limitée par Doppler de ~ 80 kHz qui est approximativement égale à la largeur de raie du laser d'excitation.

Les prochaines étapes de l'expérience seront probablement une étude expérimentale plus systématique des divers effets de décohérence résumés dans le tableau 5.1 pour observer les oscillations de Rabi entre l'état fondamental et l'état de Rydberg en utilisant le schéma d'excitation à deux photons (figure 5.2) en s'asseyant à l'un des pics de résonance indiqués dans le spectre de la figure 5.6. La réalisation globale permettrait d'explorer expérimentalement la dynamique quantique cohérente dans ce dispositif pour l'excitation Rydberg à la fois résonnante et hors résonnance.Il serait utile d'étudier le bruit de phase du laser, car cela pourrait également contribuer à la décohérence de notre système.

Il y a eu de nombreuses idées pour lesquelles un tel système de réseaux de pièges à pinces pourrait être utilisé, comme les capteurs atomiques, les interactions lumière-matière, les bits quantiques, la matière quantique habillée de Rydberg - tous avec des géométries atomiques programmables [15]. J'aborderai

dans le dernier chapitre trois applications plus spécifiques que nous avons développées à Strasbourg.

Conclusion

Dans les remarques finales de cette thèse, je souligne la démonstration réussie d'une plate-forme de grands réseaux de centaines d'ensembles atomiques microscopiques piégé dans des pièges à pince optique où chaque pince a environ remplissage uniforme, faible étendue spatiale et faibles fluctuations du nombre d'atomes ber entre les réalisations. Avec cette approche, il est possible de passer à l'échelle des centaines, voire des milliers de pinces comme le grand volume du réservoir permet de remplir simultanément plusieurs pinces en parallèle sans la nécessité de disposer de lasers supplémentaires et de protocoles de réarrangement complexes pour remplir les sites vides. Les ensembles atomiques offrent également un couplage Rabi amélioré et une la robustesse contre la perte de particules, puisque la perte d'une ou plusieurs particules de chaque micropiège n'entraîne pas de défauts qui seraient autrement difficiles à réparer.

Comme condition préalable nécessaire pour atteindre l'objectif de la manipulation cohérente des excitations de Rydberg parmi ces ensembles atomiques, ont également présenté les expériences concernant le Rydberg à largeur de bande étroite l'excitation de ces réseaux d'ensembles atomiques microscopiques. J'attends avec impatience de voir comment ces contributions contribuent à faire progresser le domaine, notamment en ce qui concerne ouvrir de nouvelles voies de recherche qui pourraient éventuellement inclure : l'étude des le couplage lumière-matière dans des ensembles atomiques en interaction, ou pour mieux construire qubits qui exploitent ces effets collectifs, simulation de modèles de spin quantique et des systèmes complexes à désordre programmable, en explorant le rôle des quantique cohérence des tumeurs dans la dynamique quantique moléculaire grâce à la simulation quantique, et l'exploitation de la dynamique quantique pour l'ingénierie d'états quantiques intéressants pour la métrologie et l'informatique avec des configurations spatiales programmables et des interactions polyvalentes sous la médiation de Rydberg.

Contents

1 Introduction **1**

1.1 Large arrays of ultracold atoms 2

1.2 Ultracold Rydberg atoms for quantum simulation 3

1.3 Thesis overview 4

2 Principles of optical dipole trapping and Rydberg atoms **7**

2.1 Optical dipole potential 8

2.1.1 Interaction of an induced dipole with a driving field . . . 8

2.1.2 Polarizability of atoms 10

2.1.3 Scattering rate and dipole trap potential 11

2.2 Rydberg atoms: giants of the atomic world 12

2.2.1 Two-photon Rydberg excitation 14

2.2.2 Rydberg blockade and anti-blockade 17

2.3 Summary 20

3 Experimental setup for producing large arrays of tweezer traps **21**

3.1 Requirements for ultracold atomic experiments 22

3.2 The ultracold atomic apparatus 22

3.2.1 The vacuum system 23

3.2.2 Laser cooling and trapping of ^{39}K 25

3.2.3 Optical dipole trap 29

3.3 Digital micromirror Device 31

3.3.1 Why we use a DMD ? 31

3.3.2 Working principles of DMD 32

3.4 Integration of DMD in the high resolution imaging system 35

3.4.1 Imaging configurations of DMD 35

3.4.2 Estimating the resolution of the imaging system 36

3.4.3 The pattern creator for DMD 37

3.4.4 Characterisation of an individual intensity pattern created by DMD . . . 39
3.4.5 DMD pattern adaptation . . . 39
3.5 Estimation of microtrap parameters . . . 41
3.6 Summary . . . 43

4 Characterisation of hundreds of microscopic atomic ensembles 45
4.1 Optimization of atom loading in tweezer traps . . . 46
4.1.1 Estimation of atom number per tweezer . . . 47
4.1.2 Single shot detection sensitivity . . . 50
4.1.3 Analysis of atom loading into a single tweezer trap . . . 51
4.2 Uniform loading across the tweezer array . . . 53
4.3 Towards single Rydberg excitation within a microscopic atomic ensemble . . . 56
4.3.1 Infidelity of single Rydberg excitation within a single tweezer . . . 58
4.3.2 Estimation of effects of fluctuations in atom number over the infidelity of single Rydberg excitation . . . 59
4.4 Summary . . . 60

5 Rydberg excitation of microscopic atomic ensembles 63
5.1 Two-photon excitation scheme . . . 64
5.2 Rydberg ion detection scheme . . . 66
5.3 Rydberg excitation spectroscopy of $69S_{1/2}$ state in ^{39}K . . . 68
5.3.1 Rydberg excitation from pancake-shaped optical dipole trap . . . 69
5.3.2 Rydberg excitation from array of microscopic atomic ensembles . . . 71
5.4 Estimation of the factors responsible for the spectral broadening 72
5.4.1 Broadening due to the Rydberg interactions between the tweezer traps . . . 76
5.5 Summary . . . 78

6 Conclusion and outlook 81
6.1 Summary: . . . 81
6.2 Outlook: . . . 83
6.2.1 Possible improvements in the current experimental set-up 83
6.2.2 Complex system dynamics by Rydberg facilitation: . . . 83

6.2.3 Quantum simulation of energy transport 85
6.2.4 Experimental realisation of quantum cellular automata (QCA): 86

List of Figures

0.1 Examples of optically trapped neutral atoms in programmable tweezer arrays x
0.2 Schematic of setup used to produce large tweezer traps in Strasbourg xii
0.3 Realization of large tweezer arrays xiv

1.1 Examples of optically trapped neutral atoms in programmable tweezer arrays 3
1.2 Schematic of setup used to produce large tweezer traps in Strasbourg 4

2.1 Schematic representation of the array of optical dipole traps . . . 9
2.2 Visualisation of a Rydberg atom and associated level structure and the interaction strength between two Rydberg atoms compared to the ground state atoms and the ions 13
2.3 Representation of the two-photon excitation scheme 15
2.4 Dynamics of three level system 18
2.5 Illustration of Rydberg blockade and anti-blockade effects 19

3.1 Overview of the experimental apparatus 23
3.2 Level scheme of potassium 39 and laser beam frequencies for the MOT 26
3.3 Laser system for laser cooling and trapping 27
3.4 Potassium 39 in an ODT 30
3.5 Schematic of DMD 31
3.6 DMD as a blazed grating 34
3.7 Imaging configurations of DMD 35
3.8 Experimental set-up of high resolution imaging system 38
3.9 Patterns generated by a user interface based on Python 39

3.10 Point spread function and intensity profile width of DMD Pattern Size by varying the DMD pixels 40
3.11 DMD pattern adaptation 40
3.12 Intensity profiles with and without Gaussian compensation . . . 41
3.13 Intensity patterns produced by DMD 42
3.14 Estimation of microtrap parameters 42

4.1 Realization of large tweezer arrays 46
4.2 Estimation of number of atoms in each tweezer 48
4.3 Estimation of single shot sensitivity 50
4.4 Characterization of the loading process and lifetime of atoms in a single tweezer 52
4.5 Uniformity of occupation across tweezer array 53
4.6 Comparison between patterns with and without gradient 55
4.7 small spatial extent of micro-traps 57
4.8 Infidelity of single Rydberg excitation within a tweezer 60

5.1 Excitation lasers setup around science chamber 64
5.2 Tow-photon Rydberg excitation level scheme 67
5.3 Excitation sequence for Pancake 69
5.4 Rydberg Spectrum for Pancake atoms 70
5.5 Excitation sequence for tweezer traps 71
5.6 Rydberg Spectrum for tweezer traps 73
5.7 Simulation of the three level Optical Bloch Equations for different Rabi frequencies of the upper transition 75
5.8 Effects of variation of lattice period on spectral width 77
5.9 Density effects on spectral broadening 79

6.1 Physical system for studying epidemic growth and dynamics on complex networks 84
6.2 Scematic of energy transport 85
6.3 Quantum cellular automata 87

List of Tables

5.1 Summary of spectral broadening mechanisms 79

Chapter 1

Introduction

Richard Feynman famously remarked in 1980, "Nature isn't classical, dammit, and if you want to make a simulation of nature, you'd better make it quantum mechanical, and by golly it's a wonderful problem, because it doesn't look so easy". Not long after it became possible to design quantum systems in the laboratory that capture the key feature of the real complex many-body quantum systems hoping to observe and to study new emergent properties under controllable experimental conditions. This is challenging because the collective emergent behaviour of the system does not necessarily follow from the underlying characteristics of its building blocks. For example, why a collective quantum dynamics and new phenomena such as superfluidity [1–3] and superconductivity [4–7] occur in some materials at quite low temperatures is still a major challenge to explain satisfactorily. A thorough study of origins of such effects would help to engineer new materials with desired properties and possibly new physical effects. But the conventional methods of constructing theoretical models to study such relevant physics are limited due to exponential scaling of the complexity with the increasing number of particles and their degrees of freedom. To overcome this issue, there have been substantial efforts towards the approach of quantum simulation [8, 9]. The goal of quantum simulation is to mimic the Hamiltonian of a target system as closely as possible. This highlights on the need to develop controllable/programmable quantum systems. This allows to study and measure the system parameters in more controlled environment in a laboratory [10].

The approach of quantum simulation is set to become an indispensible tool

for gaining new insights in the broad spectrum of studying complicated, real-world many-body problems from various fields incorporating condensed matter physics, chemistry, nuclear and high-energy physics, atomic physics, quantum chemistry and cosmology, etc. [10]. In past decades, many systems have been studied ranging from ions [11], photons [12], ultracold atoms in optical lattices [13], superconducting circuits [14] and Rydberg arrays [15]. This thesis focuses on trapped ultracold atoms as they are proven to be an ideal stage for quantum simulation [16] with the high degree of control over these atomic systems and great variety of physics that is being explored, e.g. the unitary Fermi gas in the BCS-BEC crossover [17–21], Bose-Hubbard systems [22–24], BKT transition [25–27] and Tonks-Girardeau gases [28, 29].

1.1 Large arrays of ultracold atoms

With the successful techniques of laser cooling and trapping [30], a great level of control has been realised over ground state properties of ultracold atoms encompassing the motion of atoms, flexible spatial geometry, isolation from the environment, long coherence time and interaction properties [31]. The spatial confinement of atoms with different geometries in 1D, 2D and 3D have been achieved with certain degrees of disorder using optical lattices [13] and tweezers [32–34]. Neutral atoms in optical tweezer arrays in particular have emerged as one of the most versatile platforms for quantum many-body physics, quantum simulation and quantum computation [32, 35–43]. This is largely because of the higher scalability, long coherence time, single site addressability and controllable interactions using highly excited Rydberg states [44–50]. Some examples of optically trapped neutral atoms in programmable tweezer arrays are shown in figure 1.1 reproduced from [15]. To date, substantial experimental efforts have been devoted to create fully occupied atomic arrays with $\simeq$1 atom in each tweezer by exploiting light-assisted inelastic collisions [53–55] and rearrangement to fill empty sites [32, 33, 38, 52, 56, 57]. So far however, achievable array sizes are limited to $\sim$ 200 [58] fully occupied sites (including for 2D and 3D systems), in part due to high power requirements per tweezer trap and increasing complexity associated with the rearrangement process for larger arrays [33, 52, 57]. During this thesis, a major achievement was an alternative approach to overcome this scalability challenge by demonstrating the preparation of large and uniformly filled arrays of hundreds of tweezers

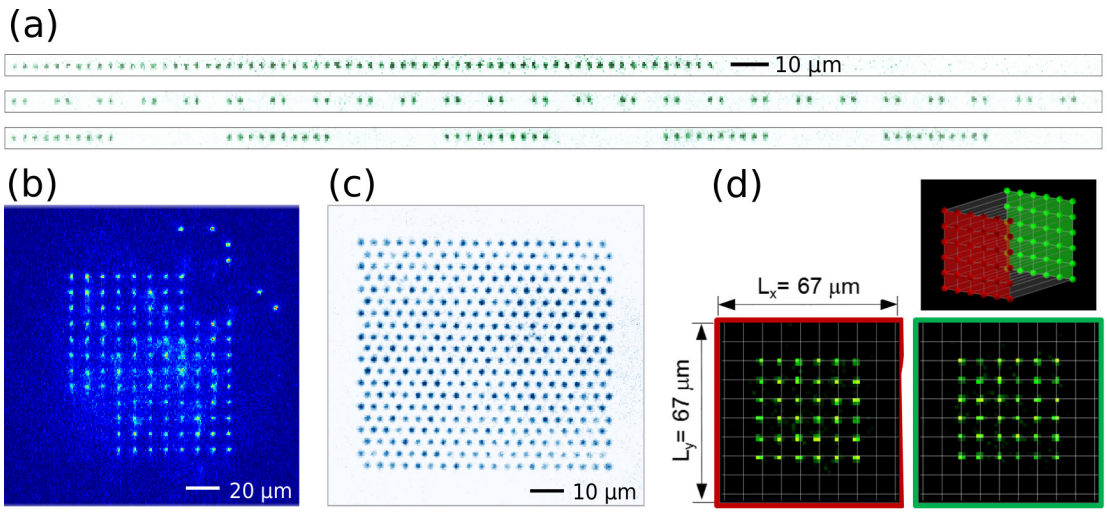

Fig. 1.1: Examples of optically trapped neutral atoms in programmable tweezer arrays (reproduced from [15]). **(a)** Fluorescence images of deterministically loaded one dimensional arrays containing more than 50 atoms in periodic, dimerized and cluster geometries. Reproduced from [32]. **(b)** Fluorescence image of a deterministically loaded two-dimensional square lattice with 111 atoms. Reproduced from [33]. **(c)** Absorption image of a triangular lattice of microscopic atomic ensembles containing more than 400 sites. Reproduced from [51]. **(d)** Fluorescence image of a deterministically loaded bilayer lattice of 72 sites. Reproduced from [52].

with large occupation number in a single step (as compared to a single atom) and along the way greatly advance the feasibility of qubits based on trapped atomic ensembles [51].

1.2 Ultracold Rydberg atoms for quantum simulation

The dominant interaction governing the dynamics mediated via electrons in real materials is Coulomb type interaction that ranges over large distances [59]. Hence, it is an obvious desire for quantum simulation to mimic such long range interactions as closely as possible to real natural materials. There have been efforts towards certain atomic and molecular platforms for simulating long-range interactions such as magnetic atomic species namely Erbium, Chromium and Dysprosium [60–62] which exhibit magnetic dipole-dipole interactions. Another platform is utilising ground state polar molecules which interact through collective dephasing dipolar dynamics [63–67]. But highly excited ultracold Rydberg atoms have advantages (over these other long-range interacting particles)

which are tunability of interactions in terms of its strength and sign and to be able to switch it completely off, making it more flexible than other approaches. Rydberg atoms demonstrate strong Van der Waals interactions that perpetuate well beyond typical inter-atomic distances. This gives rise to interesting collective phenomenon such as Rydberg blockade [68–71]. In the blockade effect, the interactions suppress the excitations, allowing at most one single excitation within a blockade radius which is collectively shared by all the atoms in the blockade volume [72]. This has been utilised in quantum information to realize addressable entangled states [68, 69, 73–75], to generate new phases of matter [76–83] and to simulate magnetic effects [84–87]. Combining high fidelity Rydberg blockade gates [49, 69, 88–93], these trapped atomic systems have been recently used to demonstrate coherent quantum dynamics of up to 51 qubits [94] and entangled states of up to 20 qubits in one dimensional chain (1D) [95].

1.3 Thesis overview

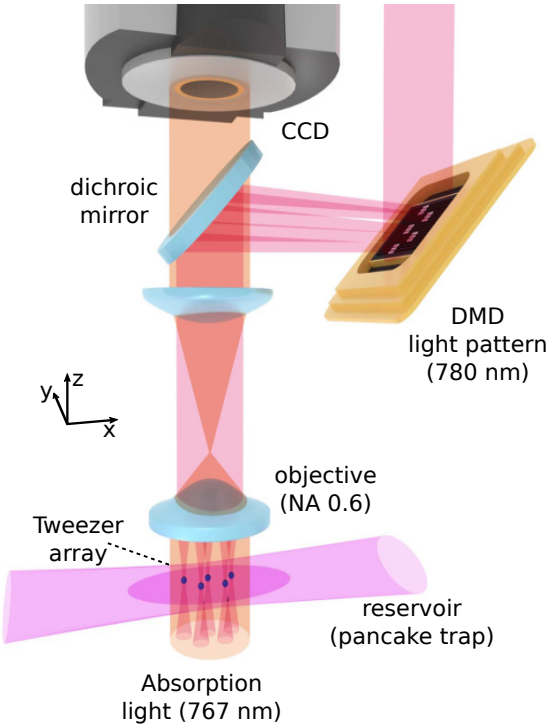

Fig. 1.2: Schematic of the setup from our lab in Strasbourg used to produce and load the tweezer arrays by projecting light from a digital micromirror device directly onto the atoms confined in an optical reservoir trap.

In this thesis, I focus on a substantial upgrade to our existing ultracold atomic experimental platform involving the generation of large arrays of optically trapped atomic ensembles (see figure 1.2 reproduced from [51]). Our novel

approach involves the preparation of versatile arrays of atomic ensembles by transferring them from a pancake shaped optical dipole trap to an array of optical tweezers created by direct projection of light patterns produced via a digital micromirror device [51]. The size of each ensemble is smaller than the Rydberg blockade radius, such that each one can carry either 0 or 1 (collective) excitations which can then strongly interact with the neighbouring ensembles. This makes it a promising platform to perform Rydberg superatom experiment expressing high single Rydberg excitation fidelity per microtrap. For the first time, it provides a strategy for potentially realizing thousands of atomic qubits for quantum simulation application.

I then present the two-photon Rydberg excitation scheme and the Rydberg detection assembly that we use for the Rydberg excitation of these atomic ensembles. I discuss the results of the experiments on the narrow linewidth Rydberg excitation of the array of atomic ensembles and describe the preliminary understanding of the broadening mechanisms such as Doppler broadening, power broadening and inhomogeneity of the excitation laser beam that could possibly broaden the spectral width of the Rydberg transition. Later as an outlook I discuss some potential applications of using the Rydberg array platform presented in this thesis which are (1) Quantum simulation of the Förster type excitation transport (between the Ryberg blockaded tweezer sites), (2) an experimental realisation of quantum cellular automata (QCA) [96], (3) Demonstration of facilitation dynamics across the array of tweezer traps to investigate effects of disorder as recently studied experimentally in our group in a non-structured ultracold atomic medium [97].

The structure of this thesis is as follows: Chapter 1 gives an introduction to the platform of large arrays of ultracold atoms and a survey of recent studies of many-body systems using ultracold Rydberg atoms. Chapter 2 develops some of the theoretical framework of optical dipole traps that is necessary towards the construction of large arrays of tweezer traps and also include the important properties of Rydberg atoms necessary to understand the Rydberg-Rydberg interaction effects between the tweezer traps. Chapter 3 concerns the characterisation of the integration of the digital micromirror device (DMD) into our existing ultracold atomic apparatus of ^{39}K to generate hundreds of optical tweezer trap potentials and presents the exotic geometries of tweezers traps. Chapter 4 describes an experimental milestone of achieving

large arrays of atomic ensembles with more than 400 sites and also describes the characterisation of this approach. Chapter 5 describes the recent results of the two-photon Rydberg excitation of these atomic ensembles presenting the narrow linewidth Rydberg excitation spectrum and presents an analysis of the mechanisms that can contribute to the broadening of the spectral width. Finally, chapter 6 presents the concluding remarks summarising the thesis and presents an outlook of utilising this versatile platform of large arrays of Rydberg atomic ensembles to study many-body quantum dynamics in quantum and classical regimes, to engineer highly entangled quantum states and towards a scalable approach to quantum information processing and computing.

Chapter 2

Principles of optical dipole trapping and Rydberg atoms

Techniques for the trapping of neutral particles have successfully served as the experimental key to great scientific advances in the field of ultracold atomic quantum matter [18, 98–100]. The ultralow-energy regime got experimentally accessible due to the dramatic developments in the area of laser cooling and trapping [101–103]. In case of neutral atoms, it has begun to be experimentally routine to generate atomic ensembles in the temperature range of micro-kelvin, and many experiments are being performed using laser-cooled atomic gases [18, 98–100]. Traps for neutral atoms can be broadly categorized in three classes such as radiation-pressure traps eg. magneto-optical trap (MOT) [104], magnetic traps [105] and optical dipole traps [106].

In the first half of this chapter, I focus on the principles of optical dipole traps [107] which depends on the electric dipole interaction with far-detuned light. Typical range of trap depths are of one milli-kelvin. The off-resonant excitation rate can be kept extremely low to avoid the limitations by the light-induced mechanisms that are present in radiation-pressure traps. With appropriate conditions, the trapping mechanism does not depend on a particular electronic ground state. Thus the dynamics of internal ground-state can be fully exploited in the experiments. Moreover, many different geometries of traps can be realized, e.g., multi-well or highly anisotropic potentials. The spatial confinement of atoms with different geometries in 1D, 2D and 3D have been achieved with certain degrees of disorder using optical dipole traps eg.

lattices [13] and tweezers [34]. In our experiments, the atoms are confined within tweezer traps separated by several micrometers as shown in figure 2.1.

To introduce long-range interactions that extend over micrometers of distances, we make use of particles with highly excited electronic states which are known as "Rydberg atoms". In the second half of this chapter, the theoretical framework is developed within the realm of Rydberg physics consisting of the relevant characteristics of single Rydberg atoms including their exaggerated properties. This part then includes the interaction of Rydberg atoms with external laser fields with the description of a two-photon excitation scheme. Later I discuss the Rydberg-Rydberg interactions that give rise to blockade effects leading to single Rydberg excitation in an ensemble of atoms, and also facilitation (anti-blockade) effects where Rydberg atoms separated by a certain distance can undergo pair-excitation in off-resonant conditions.

2.1 Optical dipole potential

The theoretical framework throughout this section is developed based on the [107]. In this section I introduce the basic principles of atom-traps created using optical dipole potentials that arise from the interaction of atoms with with far-detuned light [107]. In this case, the optical excitation rate is very low and thus the radiation force occurs due to photon scattering is negligible than the dipole force. The optical dipole force occurs from the dispersive interaction of the induced atomic dipole moment arose due to the intensity gradient of the light field [108]. The minima of the conservative force that is derived from a potential can be used to trap atoms. The performance of the optical dipole trap is limited by the absorptive part that is presented in the dipole interaction of atoms with far-detuned light fields that leads to the photon scattering of the trap light. In the following section, I consider the atom as a simple oscillator in the presence of a classical radiation field and derive the basic equations for the dipole potential and the scattering rate.

2.1.1 Interaction of an induced dipole with a driving field

In the presence of laser field $\boldsymbol{E}$, an atom gets induced dipole moment $\boldsymbol{d}$ that oscillates at the driving frequency ω. The electric field $\boldsymbol{E}$ has the form $\boldsymbol{E}(\boldsymbol{r},t) = \hat{\boldsymbol{e}}\tilde{E}(\boldsymbol{r})\exp(-i\omega t) + c.c.$ and $\boldsymbol{d}(\boldsymbol{r},t) = \hat{\boldsymbol{e}}\tilde{d}(\boldsymbol{r})\exp(-i\omega t) + c.c.$ where $\hat{\boldsymbol{e}}$ is the unit

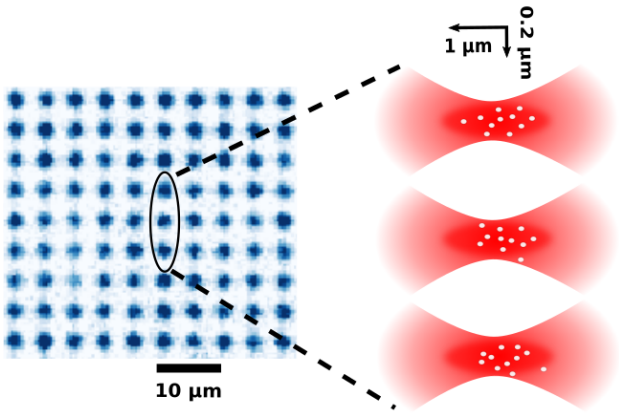

Fig. 2.1: Schematic representation of the array of optical dipole traps of atomic ensembles. In our experiments, the ensemble of atoms are confined within tweezer traps which are focused beams of Gaussian laser-light tuned far below atomic resonance separated by several micro-meters. Each blue dot in the array (left) represents an ensemble of ∼40 atoms trapped in a focused laser beam. The separation between the adjacent blue dots is ∼4 µm. On the right (zoomed-in), the illustration of ensembles of atoms trapped in focused laser beams has been shown.

polarization vector, the dipole moment amplitude $\tilde{d}$ is related to the amplitude of the field $\tilde{E}$ as

$$\tilde{d} = \beta \tilde{E}. \tag{2.1}$$

where β is the *complex polarizability* which is dependent upon the driving frequency ω. The interaction potential due to the induced dipole moment $\boldsymbol{d}$ in the presence of the driving field $\boldsymbol{E}$ is given by

$$U = -\frac{1}{2}\langle \boldsymbol{dE} \rangle = -\frac{1}{2\epsilon_0 c}\mathrm{Re}(\beta) I(\boldsymbol{r}). \tag{2.2}$$

where the angular brackets are used to indicate the time average over the fast oscillating terms, the intensity of the field is $I = 2\epsilon_0 c|\tilde{E}|^2$. Thus the potential energy of the atom in the presence of the external electric field is proportional to the intensity $I(r)$ and it is also proportional to the real part of the polarizability, that denotes the in-phase component of the oscillation of the dipole which is responsible for the dispersive nature of the interaction. The *dipole force* occurs from the gradient of the interaction potential

$$F(\boldsymbol{r}) = -\nabla U(\boldsymbol{r}) = -\frac{1}{2\epsilon_0 c}\mathrm{Re}(\beta)\nabla I(\boldsymbol{r}). \tag{2.3}$$

Hence it is a conservative force, which is proportional to the gradient of the intensity of the driving field.
The absorbed power by the oscillator from the driving field can be expressed as,

$$P = \langle \dot{\boldsymbol{d}} \boldsymbol{E} \rangle = 2\omega Im(\tilde{d}\tilde{E}) = \frac{\omega}{\epsilon_0 c}\mathrm{Im}(\beta) I(\boldsymbol{r}). \tag{2.4}$$

where $\dot{d}$ represents a time-derivative of an induced dipole moment. The absorption coming from the imaginary part of the polarizability indicates the out-of-phase component of the oscillation of the dipole. Assuming the light as a stream of photons $\hbar\omega$, the absorption can be expressed as scattering of photons in alternate cycles of absorption and spontaneous emission processes. The *scattering rate* is

$$\Gamma_{sc}(\boldsymbol{r}) = \frac{P}{\hbar\omega} = \frac{1}{\hbar\epsilon_0 c}\mathrm{Im}(\beta) I(\boldsymbol{r}). \tag{2.5}$$

Here the two main quantities for dipole traps, the interaction potential and the scattered radiation power are expressed, in terms of the the polarizability $\beta(\omega)$ and the position- dependent intensity $I(\boldsymbol{r})$ of the field. These expressions can be valid for any polarizable neutral particle that can be reduced to a two-level system in an oscillating electric field.

2.1.2 Polarizability of atoms

To determine the polarizability β, let us first consider the Lorentz's model of a classical oscillator for the atom. In this picture, an electron with mass m_e and elementary charge e is bound elastically to the core with an eigen-frequency ω_0 of the oscillation related to the frequency of the optical transition. By integrating the equation of motion $\ddot{x} + \Gamma_\omega \dot{x} + \omega_0^2 x = -eE(t)/m_e$ for the driven oscillation of the electron where $\beta = \frac{ex}{E(t)}$, we obtain,

$$\beta = \frac{e^2}{m_e}\frac{1}{\omega_0^2 - \omega^2 - \mathrm{i}\omega\Gamma_\omega}. \tag{2.6}$$

Here the classical damping rate because of the radiative energy loss is

$$\Gamma_\omega = \frac{e^2\omega^2}{6\pi\epsilon_0 m_e c^3}. \tag{2.7}$$

By substituting $e^2/m_e = 6\pi\epsilon_0 c^3 \Gamma_\omega/\omega^2$ and including the on-resonant damping rate $\Gamma \equiv \Gamma_{\omega_0} = (\omega_0/\omega)^2\Gamma_\omega$ the polarizability is obtained as,

$$\beta = 6\pi\epsilon_0 c^3 \frac{\Gamma/\omega_0^2}{\omega_0^2 - \omega^2 - \mathrm{i}(\omega^3/\omega_0^2)\Gamma}. \tag{2.8}$$

For high intensities (or too close to resonance) of the driving field, the excited state gets highly populated and the above result can no longer be valid. In our experiments of optical dipole trapping, we are mainly interested in the far detuned conditions associated with low saturation resulting in low rates of scattering ($\Gamma_{sc} << \Gamma$). Thus we can safely use the above expression.

2.1.3 Scattering rate and dipole trap potential

Using the expression for the polarizability of the atomic oscillator given by equation 2.8, we derive following expressions for the dipole potential and the scattering rate in the case of large detunings and low saturation:

$$U(\boldsymbol{r}) = -\frac{3\pi c^2}{2\omega_0^3}\left(\frac{\Gamma}{\omega_0 - \omega} + \frac{\Gamma}{\omega_0 + \omega}\right) I(\boldsymbol{r}). \tag{2.9}$$

$$\Gamma_{sc}(\boldsymbol{r}) = \frac{3\pi c^2}{2\hbar\omega_0^3}\left(\frac{\omega}{\omega_0}\right)^3 \left(\frac{\Gamma}{\omega_0 - \omega} + \frac{\Gamma}{\omega_0 + \omega}\right)^2 I(\boldsymbol{r}). \tag{2.10}$$

In many cases, the laser frequency is tuned close to the resonance at ω_0 so that the detuning $\Delta \equiv \omega - \omega_0$ satisfies $|\Delta| << \omega_0$. Here, following the rotating-wave approximation, the counter-rotating term $(\omega + \omega_0)$ can be neglected and thus $\omega/\omega_0 \approx 1$. Therefore the general expressions for the scattering rate and the dipole potential get simplified to

$$U(\boldsymbol{r}) = \frac{3\pi c^2}{2\omega_0^3}\frac{\Gamma}{\Delta} I(\boldsymbol{r}). \tag{2.11}$$

This shows that atoms are attracted towards the maximum intensity of the dipole trap laser when $\Delta < 0$ leading to negative U. For $\Delta > 0$, U is positive leading to repulsive interaction where atoms get trapped in minimum intensity region of the trapping laser.

$$\Gamma_{sc}(\boldsymbol{r}) = \frac{3\pi c^2}{2\hbar\omega_0^3}\left(\frac{\Gamma}{\Delta}\right)^2 I(\boldsymbol{r}). \tag{2.12}$$

In the scenario of far-detuned laser fields, the physics of dipole trapping can be understood based on these two equations. Thereby giving us a simple relation between the dipole potential and the scattering rate,

$$\hbar\Gamma_{sc} = \frac{\Gamma}{\Delta} U(\boldsymbol{r}). \tag{2.13}$$

The relation between the dispersive and absorptive response of the dipole oscillator leads to the result above. Therefore, the combination of different laser traps lead to the manipulation of potential landscapes. In our case, to create an optical dipole trap, we use a red-detuned $\Delta < 0$ laser. The scattering rate is proportional to I/Δ^2 and the dipole potential is proportional to I/Δ. Hence, high intensities and large detunings are usually involved in the generation of the optical dipole traps in order to have a low rate of scattering for a desired depth of the potential.

In our experiment, we use these principles of dipole trapping to create a pancake-shaped optical dipole trap. Later we re-shape the pancake-trap into exotic geometries of large arrays of microscopic optical dipole potentials which are focused Gaussian laser beams tuned far below the atomic resonance frequency. This represents the simplest way to create a dipole trap providing three-dimensional confinement (tweezer) shown in figure 2.1 to trap atomic ensembles by exploiting elastic collisions. The specific details of the generation of these arrays of tweezer traps are given in Chapter 3.

Now we need to address the important requirement of introducing long-range interactions between these micro-traps that are separated by several micrometers to produce a platform that can simulate real-life dynamics mediated via interactions such as Coulomb type. For this, we make use of Rydberg atoms and I discuss the important principles of Rydberg atoms and their interaction effects in the following sections.

2.2 Rydberg atoms: giants of the atomic world

This section summarizes some of the key concepts about Rydberg atoms. It is based on previous theses of the group [110, 111] with emphasis on the concepts used in particular for Ch 5.

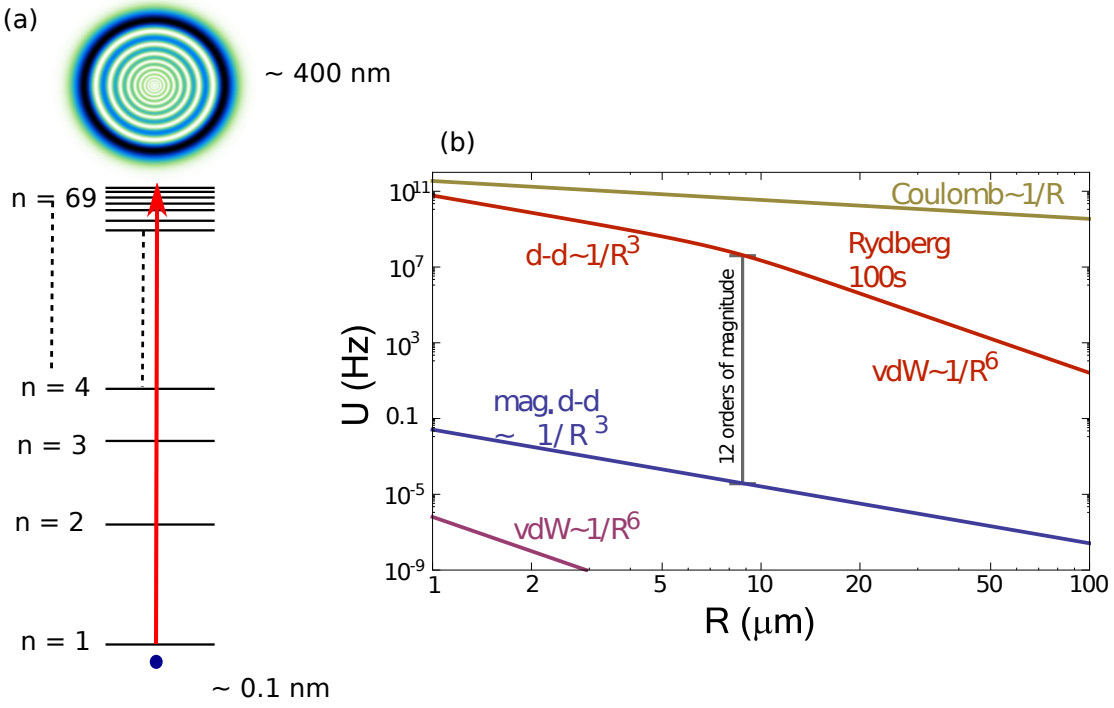

Fig. 2.2: Visualisation of giant size of Rydberg atom and interaction strength between two Rydberg atoms compared to the ground state atoms and the ions. (a) Rydberg atoms are atoms with their valence electron is excited to higher principal quantum number. They posses enormous dipole moment which results in the giant atomic size of $n = 69$ compared to the ground state atoms by 3 orders of magnitude. **(b)** (reproduced from [109]) This plot shows the interaction strength versus the distance between the two ground state atoms compared to the excited atoms to the 100s states and the ions. The interaction between two Rydberg atoms is $\approx$ 12 orders of magnitude larger than between the ground state atoms.

Rydberg atoms are atoms with the valence electron in a high principal quantum number n [72] as illustrated in figure 2.2a. This valence electron has the binding energy $E_n = -\frac{R_y}{n^{*2}}$ analogous to the hydrogen atom where n^* is the effective principal quantum number which includes the quantum defect due to the non-Hydrogenic core [72]. Here R_y is the Rydberg constant which is equal to $\frac{Z^2 e^4 m_e}{16\pi^2 \epsilon_0 \hbar^2}$. Rydberg atoms possess exaggerated properties that scale with the principal quantum number n. The relevant properties of Rydberg atoms with the corresponding scaling are given in [72]. Their dipole moment scales as n^2 resulting in the giant size of the Rydberg atom i.e. ~ 3 orders of magnitude larger for $n = 69$ compared to the ground state atoms as visualised in the figure 2.2a. Correspondingly Rydberg atoms also posses large electric transition dipole moments that mediate Rydberg-Rydberg interactions. This can be either of the Van der Waals form ($\propto \frac{1}{R^6}$) or dipole-dipole interactions ($\propto \frac{1}{R^3}$) which are strong long range interactions compared to the ground state atoms as shown in figure 2.2b (reproduced from [109]). The details of the origin of these interactions are discussed in [72]. The radiative lifetime of Rydberg atoms scales as n^3 [72] resulting in a higher lifetime of the atoms in the excited state compared to that of the ground state atoms.

2.2.1 Two-photon Rydberg excitation

Most commonly atoms can be excited to Rydberg state via a single-photon excitation or a two photon excitation scheme. In this thesis, our experiments primarily involve two-photon Rydberg excitation as represented in the figure 2.3. Here in the two-photon excitation scheme, the ground state is coupled to an intermediate via a laser field with Rabi coupling Ω_1 (shown in red arrow in the figure 2.3) and from intermediate state to the Rydberg state by a laser field with Rabi coupling Ω_2 (shown in blue arrow in the figure 2.3). The Δ_1 and Δ_2 are the detunings of the laser fields with respect to the intermediate state and the Rydberg state respectively. Hence the two-photon detuning is equal to $\Delta_1 + \Delta_2$. The Δ_1 is kept relatively large to avoid loss of atoms from the spontaneous decay from the first excitation step. For a single atom, the dynamics of this three level system can be obtained from the master equation $\dot{\hat{\rho}} = -\frac{i}{\hbar}\left[\hat{H}, \hat{\rho}\right]$, where $\hat{\rho}$ is the density operator [112] in which the diagonal terms describe the population of the basis states and the off-diagonal terms are the coherences between the states. For further development of the theoretical framework of three-level system described in this section, I follow the approach from [113].

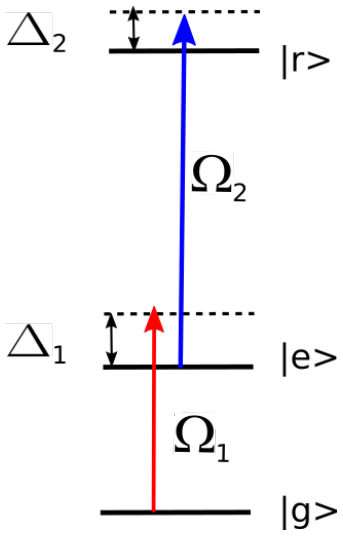

Fig. 2.3: Representation of the two photon excitation scheme Two-photon Rydberg excitation through an intermediate state ($|e\rangle$) in a three-level system. A laser field with Rabi coupling Ω_1 (shown in red arrow) drives the transition from ground state to the intermediate state and another laser field with Rabi coupling Ω_2 (shown in blue arrow) drives the transition from the intermediate state to the Rydberg state $|r\rangle$ in the three level system. The Δ_1 and Δ_2 are the detunings of the laser fields with respect to the intermediate state and the Rydberg state respectively. Hence the two-photon detuning is equal to $\Delta_1 + \Delta_2$.

To include the dissipation caused by spontaneous decay and the dephasing due to the laser noise, we use a quantum master equation in Lindblad form [114] that represents the time evolution for the three level atomic system as,

$$\dot{\hat{\rho}} = -\frac{i}{\hbar}\left[\hat{H}, \hat{\rho}\right] + \mathcal{L}[\hat{\rho}], \tag{2.14}$$

where $\mathcal{L}[\hat{\rho}]$ the Lindblad superoperator [115] that is used to model the decoherence due to spontaneous decay and the dephasing processes.

$$\mathcal{L}[\hat{\rho}] = \sum_i \mathcal{L}(\hat{\rho}, \sigma_i) + \mathcal{L}_d(\hat{\rho}). \tag{2.15}$$

where $\mathcal{L}(\hat{\rho}, \sigma_i) = \sum_i \sigma_i \hat{\rho} \sigma_i^\dagger - (\sigma_i^\dagger \sigma_i \hat{\rho} + \hat{\rho} \sigma_i^\dagger \sigma_i)/2$ is the Lindblad superoperator [115] that describes the spontaneous decay for the transitions coupled by the jump operators $\sigma_i, \sigma_i^\dagger$ and $\mathcal{L}_d$ is the matrix that describes the dephasing in the three level system due to the linewidths of the coupling laser fields. The

Hamiltonian for the three-level system can be expressed as,

$$\hat{H} = (\hbar/2)\begin{pmatrix} 0 & \Omega_1 & 0 \\ \Omega_1 & -2\Delta_1 & \Omega_2 \\ 0 & \Omega_2 & -2(\Delta_1+\Delta_2) \end{pmatrix} \tag{2.16}$$

which consists of the Rabi couplings Ω_1 and Ω_2 between the ground state $|g\rangle$ and the excited state $|e\rangle$ and the excited state $|e\rangle$ with the Rydberg state $|r\rangle$ respectively. The Δ_1 and Δ_2, are the detunings for each laser field as represented in figure 2.3. The spontaneous decay rate Γ_1 from state $|e\rangle$ to state $|g\rangle$ and the rate Γ_2 from state $|r\rangle$ to state $|e\rangle$ can be included using the operators $\sigma_1 = \sqrt{\Gamma_1}\,|g\rangle\langle e|$ and $\sigma_2 = \sqrt{\Gamma_2}\,|e\rangle\langle r|$. The Lindbladian superoperator that describes the spontaneous decay of the three level system can be expressed as,

$$\mathcal{L}(\hat{\rho},\sigma) = \begin{pmatrix} \Gamma_1\hat{\rho}_{ee} & -\frac{1}{2}\Gamma_1\hat{\rho}_{ge} & -\frac{1}{2}\Gamma_2\hat{\rho}_{gr} \\ -\frac{1}{2}\Gamma_1\hat{\rho}_{eg} & -\Gamma_1\hat{\rho}_{ee}+\Gamma_2\hat{\rho}_{rr} & -\frac{1}{2}(\Gamma_1+\Gamma_2)\hat{\rho}_{er} \\ -\frac{1}{2}\Gamma_2\hat{\rho}_{rg} & -\frac{1}{2}(\Gamma_1+\Gamma_2)\hat{\rho}_{re} & -\Gamma_2\hat{\rho}_{rr} \end{pmatrix} \tag{2.17}$$

where the $\hat{\rho}_{ij}$ is the ij element of the density matrix $\hat{\rho}$.
The dephasing matrix can be expressed as,

$$\mathcal{L}_d(\hat{\rho}) = \begin{pmatrix} 0 & -\gamma_1\hat{\rho}_{ge} & -(\gamma_1+\gamma_2)\hat{\rho}_{gr} \\ -\gamma_1\hat{\rho}_{eg} & 0 & -\gamma_2\hat{\rho}_{er} \\ -(\gamma_1+\gamma_2)\hat{\rho}_{rg} & -\gamma_2\hat{\rho}_{re} & 0 \end{pmatrix} \tag{2.18}$$

where γ_1 and γ_2 are linewidths of the coupling laser fields for lower excitation and upper excitation respectively.
Using equation 2.17 and equation 2.18 and substituting them into equation 2.14,

we obtain the optical Bloch equations as,

$$
\begin{aligned}
\dot{\hat{\rho}}_{gg} &= \Gamma_1\hat{\rho}_{ee} + \frac{i}{2}(\Omega_1\hat{\rho}_{ge} - \Omega_1^*\hat{\rho}_{eg}).\\
\dot{\hat{\rho}}_{ee} &= -\Gamma_1\hat{\rho}_{ee} + \Gamma_2\hat{\rho}_{rr} - \frac{i}{2}(\Omega_1\hat{\rho}_{ge} - \Omega_1^*\hat{\rho}_{eg}) + \frac{i}{2}(\Omega_2\hat{\rho}_{er} - \Omega_2^*\hat{\rho}_{re}).\\
\dot{\hat{\rho}}_{rr} &= -\Gamma_2\hat{\rho}_{rr} - \frac{i}{2}(\Omega_2\hat{\rho}_{er} - \Omega_2^*\hat{\rho}_{re}).\\
\dot{\hat{\rho}}_{ge} &= -(i\Delta_1 + \frac{\Gamma_1}{2} + \gamma_1)\hat{\rho}_{ge} - \frac{i\Omega_1^*}{2}(\hat{\rho}_{ee} - \hat{\rho}_{gg}) + \frac{i\Omega_2}{2}\hat{\rho}_{gr}.\\
\dot{\hat{\rho}}_{er} &= -(i\Delta_2 + \frac{\Gamma_1 + \Gamma_2}{2} + \gamma_2)\hat{\rho}_{er} - \frac{i\Omega_2^*}{2}(\hat{\rho}_{rr} - \hat{\rho}_{ee}) - \frac{i\Omega_1}{2}\hat{\rho}_{gr}.\\
\dot{\hat{\rho}}_{gr} &= -(i(\Delta_1 + \Delta_2) + \frac{\Gamma_2}{2} + \gamma_1 + \gamma_2)\hat{\rho}_{gr} + \frac{i\Omega_2^*}{2}\hat{\rho}_{ge} - \frac{i\Omega_1^*}{2}\hat{\rho}_{er}.
\end{aligned}
\tag{2.19}
$$

Exemplary simulations of these three-level optical Bloch equations are shown in figure 2.4. Population dynamics of ground state ρ_{gg} shown in red, of intermediate state ρ_{ee} shown in green and of Rydberg state ρ_{rr} shown in blue. The detuning of the lower transition is Δ_1 = -300 MHz and the detuning of the upper transition is Δ_2 = 300 MHz. At such a high detuning, the three level system effectively behaves as a two level system where population oscillates between ground state and the Rydberg state while hardly populating the intermediate state. The Rabi frequencies $\Omega_1 = 2\pi \times 13$ MHz and $\Omega_2 = 2\pi \times 30$ MHz are chosen based on the experimental estimates used in chapter 5. The spontaneous decay rate from the intermediate state is $2\pi \times 6$ MHz which is for the D2 transition of potassium-39 and the Rydberg state decay rate is taken as $\sim$ 10 kHz. The dephasing rates $\gamma_1 = 20$ kHz and $\gamma_2 = 60$ kHz are based on estimates of the laser linewidths. All these parameters are similar to our actual experimental parameters. The condition of two-photon resonance is met as $\Delta_1 + \Delta_2 = 0$. As we observe in the figure that the Rabi oscillations decay at ≈ 25 μs. The effective Rabi coupling of this three level system $\frac{\Omega_1\Omega_2}{2\Delta}$ is $\approx 2\pi \times 0.63$ MHz. Experimental studies of Rydberg excitation including a search for these Rabi oscillations in microscopic atomic ensembles is presented in chapter 5.

2.2.2 Rydberg blockade and anti-blockade

Based on pure two-level system, figure 2.5 shows a pair-state basis of two interacting atoms where the interaction strength scales with respect to the distance (R) between the atoms as $\propto 1/R^6$ which is the typical interactions observed in our experiment as Van der Waals interaction. As a convenient

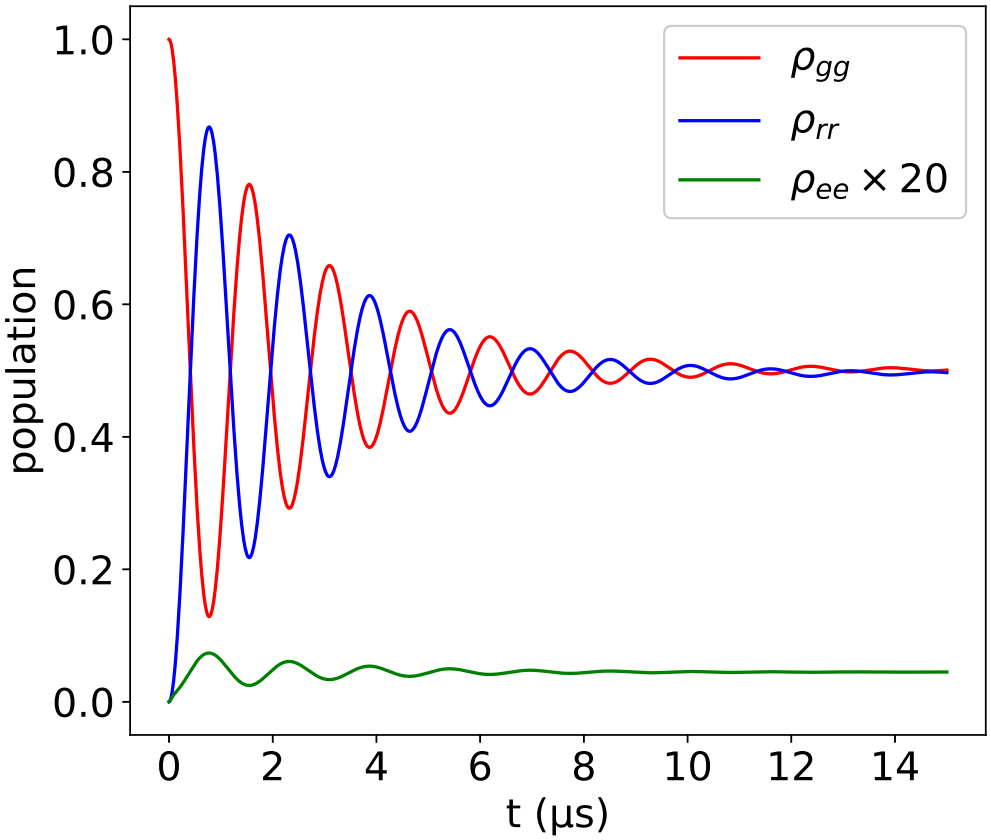

Fig. 2.4: Simulation of three level optical Bloch equations describing the time-evolution of the atomic system Population dynamics of ground state ρ_{gg} shown in red, of intermediate state ρ_{ee} shown in green and of Rydberg state ρ_{rr} shown in blue. The intermediate state detuning Δ_1 = -300 MHz and the detuning with respect to the Rydberg state Δ_2 = 300 MHz. At such a high detuning, the three level system effectively behaves as a two level system where population oscillates in between ground state and the Rydberg state without populating the intermediate state. Here $\Omega_1 = 2\pi \times 13$ MHz and $\Omega_2 = 2\pi \times 30$ MHz. The spontaneous decay rate from the intermediate state is equal to $2\pi \times 6$ MHz which is equal to that of the D2 transition of potassium-39 and that of the Rydberg state is $\sim$ 10 kHz. The laser linewidths $\gamma_1 = 20$ kHz and $\gamma_2 = 60$ kHz. All these parameters are similar to our actual experimental parameters. The condition of two-photon resonance is met as $\Delta_1 + \Delta_2 = 0$. As we observe in the figure that the Rabi oscillations decay at ≈ 15 μs. The effective Rabi coupling of this three level system $\frac{\Omega_1 \Omega_2}{2\Delta}$ is $\approx 2\pi \times 0.63$ MHz.

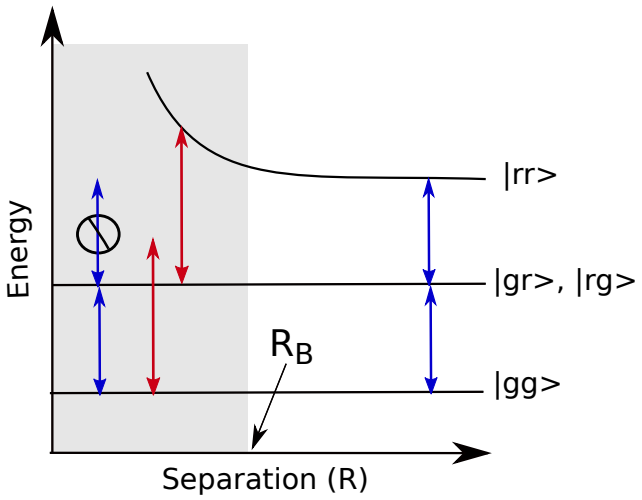

Fig. 2.5: Illustration of Rydberg blockade and anti-blockade effects. When the laser field is resonant with the Rydberg state (blue), an another Rydberg excitation is suppressed within the distance of the blockade radius R_B. The grey region represents the blockade area. At off-resonant laser frequency with respect to the Ryderg transition, an another Rydberg excitation can happen at a certain distance when the detuning is matched with energy shift of the Rydberg state.

basis, we use $\{|gg\rangle, |gr\rangle, |rg\rangle, |rr\rangle\}$ where the laser field couples the $|gg\rangle \leftrightarrow |gr\rangle + |rg\rangle$ and $|rr\rangle \leftrightarrow |gr\rangle + |rg\rangle$ transitions.

As visualized in the figure 2.5, when a laser field resonant with the $|g\rangle \leftrightarrow |r\rangle$ transition can excite a first atom (to the $|gr\rangle + |rg\rangle$ pair state). However the strong Rydberg-Rydberg interactions shift the $|rr\rangle$ state out of resonance, suppressing the excitation of both atoms within a certain distance which is known as blockade radius R_B [68–71]. The grey region represents the blockade area. The blockade radius R_B can be estimated according to the linewidth (Δ_ν) of the excitation laser,

$$\hbar\Delta_\nu = \frac{C_6}{R_B^6} \Rightarrow R_B = \left(\frac{C_6}{\hbar\Delta_\nu}\right)^{1/6} \tag{2.20}$$

where $C6$ is the interaction coefficient [72]. At off-resonant laser frequency with respect to the Rydberg transition $|rr\rangle$, an another Rydberg excitation can happen at a certain distance when the detuning is matched with the energy shift of the Rydberg state as shown in the figure 2.5. This is known as anti-blockade effect or facilitation effect [74, 116]. This effect is being investigated in a non-structured atomic medium in our group [97] (see figure 6.1 in chapter 6).

For N atoms within the blockade volume (typically the case in our experiment with the tweezer trap of atomic ensembles being located within the blockade radius), the excitation is shared among all the atoms in the blockade region and system undergoes a collective Rydberg excitation that can be expressed as $\frac{1}{\sqrt{N}} \sum_{j=1}^{N} |ggg..r_j..g\rangle$. The collective Rabi coupling is then equal to $\sqrt{N}\Omega$ that indicates the many-body character of the system. For more details of collective excitation within a microscopic atomic ensemble, see section 4.3 in chapter 4.

2.3 Summary

In the first half of this chapter, I have described the basic principles of optical dipole traps that are based on the electric dipole interaction of atoms with far-detuned light. I have considered the atom as a simple oscillator to derive the main equations for optical dipole interactions that include the dipole potential and the scattering rate. Based on these principles, we have built a platform of large arrays of tweezer traps where the ensembles of atoms are confined within the tweezer traps separated by several micro-meters. In the second half of this chapter, I describe the basic concepts of Rydberg atoms that help us introduce the long-range interactions between the tweezer traps that extend over the distance of several micro-meters. In the next chapter we will use these concepts to understand the preparation of large arrays of optical dipole traps created using digital micromirror device (DMD).

Chapter 3

Experimental setup for producing large arrays of tweezer traps

This chapter starts with a brief overview of our existing cold-atomic apparatus with the main components such as the vacuum system, atomic source of potassium-39 and the laser cooling and trapping referring to the PhD theses of my colleagues Dr. Stephan Helmrich [110] and Dr. Alda Arias [111] and master thesis [117] for some of the more technical details. I then focus on the successful integration of the digital micromirror device (DMD) to our existing cold-atomic apparatus which is used to create Rydberg ensembles with a particular focus on the realisation of structured optical fields using DMD. I introduce the DMD technology and the important characteristics of the large arrays of microtraps created using the DMD in terms of the three-dimensional shape of each tweezer trap (compared to the Rydberg blockade radius), trap depth, trap frequency and the scattering rate. The objectives that we address through the realisation of the tweezer platform include having the trap waist of the tweezer of ≈ 1 µm, trap depth of ≈ 1 mK, trap frequency of ≈ 100 kHz, fast switching rate, low noise over the trap potential to avoid atom heating and decoherence. The result is a versatile and controllable experimental platform to study quantum many body physics, to perform experiments related to quantum simulation and quantum computation.

3.1 Requirements for ultracold atomic experiments

For studying quantum dynamics in an atomic system, it is required to maintain coherence conditions by having a control over the atomic motion and advanced techniques, to manipulate, excite and to read-out the state of the particles. Following are four main criteria of an ultracold-atomic platform:

- Well isolated atomic system from the environment.
- Control over internal electronic states of atoms and their external degrees of freedom such as kinetic energy.
- Precise spatially resolved detection of atoms along with the discrimination between their different internal states.
- For making effective use of Rydberg interactions, the laser for Rydberg excitation should be powerful ($\sim$ 500 mW), tunable and with narrow linewidth ($< \sim$ 60 kHz).

These criteria are the key elements required for using ultracold, neutral atoms as a platform for quantum technology. Our focus in this direction is to use multi-site geometries created by arrays of optical tweezers to trap ensembles of ultra-cold atoms. This is largely because of the easy scalability of the tweezer traps, long coherence time, single site addressability and controllable interactions using highly excited Rydberg states. These requirements are potentially met by setups which are based on programmable optical elements such as spatial light modulators (SLMs) [37], microlens array [35], accousto-optic deflectors (AOD) [55] and digital micromirror device (DMD) [118] for trapping, guiding, and manipulating neutral atoms. In our experimental set-up, we make use of DMD to generate large arrays of microtraps.

3.2 The ultracold atomic apparatus

This section gives an overview of our existing cold-atomic apparatus. The experiments in this thesis start with an ultracold atomic sample of potassium atoms trapped in a pancake shaped optical dipole trap. The typical temperature achieved is $\approx 20\mu$K, with peak densities of $\approx\ 2 \times 10^{10}\text{cm}^{-3}$. This section is an introduction of the experimental platform and the presentation of the cooling and trapping techniques.

3.2.1 The vacuum system

To satisfy the requirement of good isolation from the environment, a vacuum chamber[1] has been used. This leads to the ultra high vacuum with quite low pressures of $\sim 10^{-10}$ mbar to reduce collisions between the trapped atoms and the background particles. Otherwise these collisions cause losses that could dominate over the actual system dynamics. Two vacuum pumps are necessary

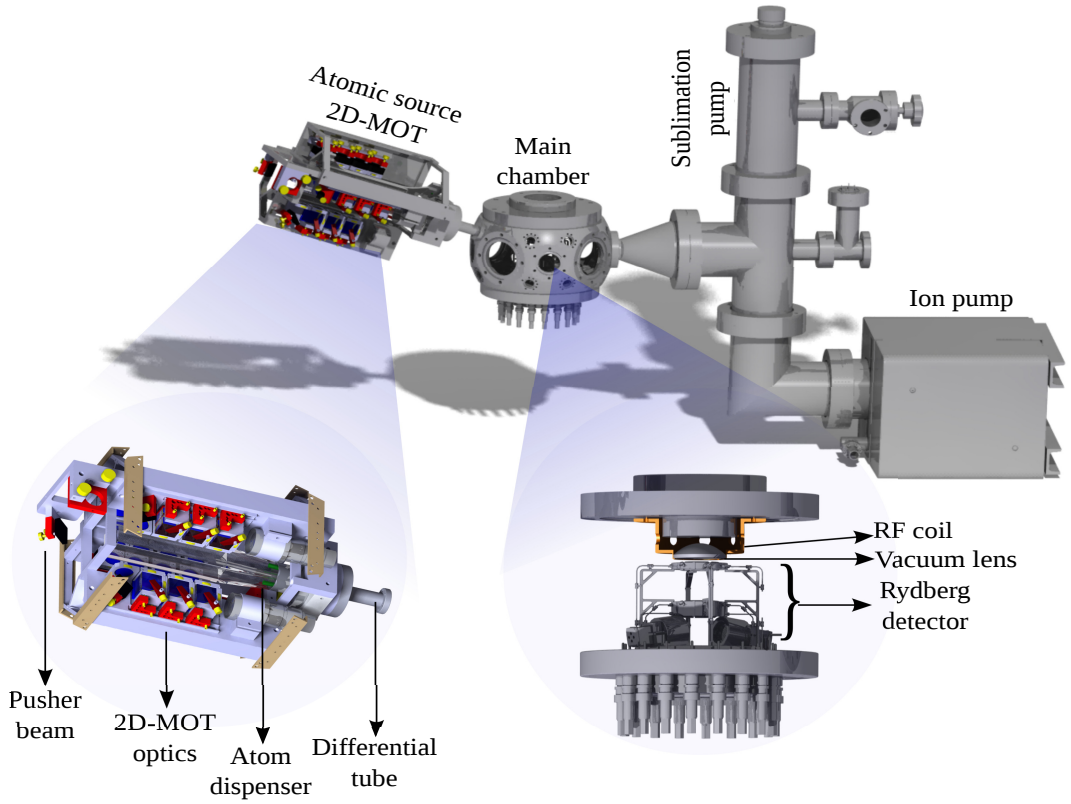

Fig. 3.1: Overview of the experimental apparatus. (Image reproduced from [111]) The main parts in the experimental setup are represented in here. The potassium dispenser-atom source (left) is placed inside a glass cell, and the surrounded optics constitute the 2D MOT (see zoom in) that creates a stream of atoms cold in the transversal directions that gets pushed towards the main chamber (center in the figure). The atoms go through a differential tube into the main chamber where they get further cooled and trapped. Inside the chamber a high resolution imaging lens, an MCP Rydberg ion detector and a radio-frequency antenna are placed for manipulation and state control. To maintain the high vacuum in the chamber, we have the ion pump and the sublimation pump on the right to the main vacuum chamber. Image adapted from [111]

(see figure 3.1) to achieve and maintain the low pressure inside the vacuum

[1] Kimball Physics. 8 Multi-Cf Spherical Square MCF800-SphSq-G2E4C4A16.

chamber. The first one is a 125 l/s ion pump[2] that ionizes the gas inside the chamber and using a high electrical potential, it attracts the ions towards the pump. The second is a titanium-sublimation pump[3] which sublimates a titanium filament using high current. The titanium gets attached to the inner surface of the walls of the chamber and because of its high reactivity, any particle touching the wall reacts with the titanium forming a solid component reducing the pressure inside the chamber.

The combination of the vacuum system made of non-magnetic stainless steel with viewports enables optical access for the different laser beams for cooling, trapping and Rydberg excitation. There are ten main viewports to the vacuum chamber that are located in the horizontal plane and the vertical axis. They are made of fused silica, vacuum sealed and anti-reflection coated based on the laser wavelength and the power that enter the chamber. These viewports allow sufficient optical access with high flexibility in the number of beams and their wavelength involved.

Three more elements have been included inside the vacuum chamber (see zoom in, figure 3.1). The first one is an aspheric lens[4] designed for high optical resolution imaging with a focal length of 32 mm, numerical aperture of 0.62 and a coating [5] to prevent charge accumulation on the surface of the lens which could interfere with any measurement due to the high sensitivity of the Rydberg atoms to electric fields (see chapter 2). The second one is a radio frequency antenna, which is mde of a coil wrapped around the lens holder of an aspheric lens situated inside the vacuum chamber as mentioned earlier. The third element is a detector for Rydberg atoms which is called as a micro-channel plate (MCP) which consists of a structure of split rings of electrodes which are used to compensate stray electric fields, to generate homogeneous electric field and the create high ionising electric fields for ionisation of the Rydberg atoms and to accelerate those ions towards the detector. Moreover two deflection rings are used to control the trajectory of the ions travelling towards the MCP. A combination of all these components allows a better control of the atoms as further explained in detail in the following sections.

[2]Agilent technologies. VacIon Plus 150 Ion Pump StarCell
[3]Agilent technologies. TSP Cartridge Filament Source
[4]Asphericon A45-32 HPX
[5]ITO (Indium tin oxide) coating

3.2.2 Laser cooling and trapping of ^{39}K

A necessary criteria for our ultracold atom platform is the control over the thermal motion and spatial confinement of atoms. In our group, we work with potassium due to its stable bosonic and fermionic isotopes, i.e. ^{39}K (bosonic), ^{40}K (fermionic) and ^{41}K (bosonic). This is important provided that the quantum dynamics is governed either by fermionic or bosonic statistics [119]. Along with Rydberg excitations, a competition between certain ground-state statistics and the long range interactions can give rise to new phases of quantum matter [76–79].

Energy level scheme of ^{39}K

Throughout this thesis, only ^{39}K has been used. Figure 3.2 shows energy level scheme for the valence shell electron of ^{39}K, including the ground state ($4S_{1/2}$) and the first two excited states ($4P_{1/2}$ and $4P_{3/2}$). The transition between the ground state $4S_{1/2}$ and the first excited state $4P_{1/2}$ is called the D1 transition and the transition between the ground state $4S_{1/2}$ and the second excited state $4P_{3/2}$ is called the D2 transition. To address the D1 and D2 transitions, we have two different diode lasers.

Laser system for cooling and trapping

We utilise the D1 and D2 transitions (see figure 3.2) for the preliminary stages of cooling and trapping. To address these transitions, two diode lasers[6] at the respective wavelengths (767 nm and 770 nm) are used. For locking the laser to the $|4s_{1/2}, F = 2\rangle \rightarrow |4p_{3/2}, F' = 3\rangle$ (D2) and from crossover between the $|4s_{1/2}, F = 2\rangle$ and $|4s_{1/2}, F = 1\rangle \rightarrow |4p_{1/2}, F' = 3\rangle$ (D1) transition of ^{39}K [122], we obtain an error signal using modulation transfer spectroscopy (MTS) [123, 124]. The laser light is coupled to a fiber and then enters into the first amplification stage based on a home built tapered amplifier [125]. The amplification of only one of the wavelengths is allowed at a time via an acuosto-optical modulator. As a result, the home-built amplifier get seeded with only one of the wavelengths at a time. This amplifies the seed light from 10 mW to 500 mW.This amplified light is the redistributed into three further amplification stages viz. 3D cooler, 2D cooler and another branch for repumping. (see figure 3.3). As shown in the figure, each light beam passes

[6] Toptica. Tunable diode laser, DL pro

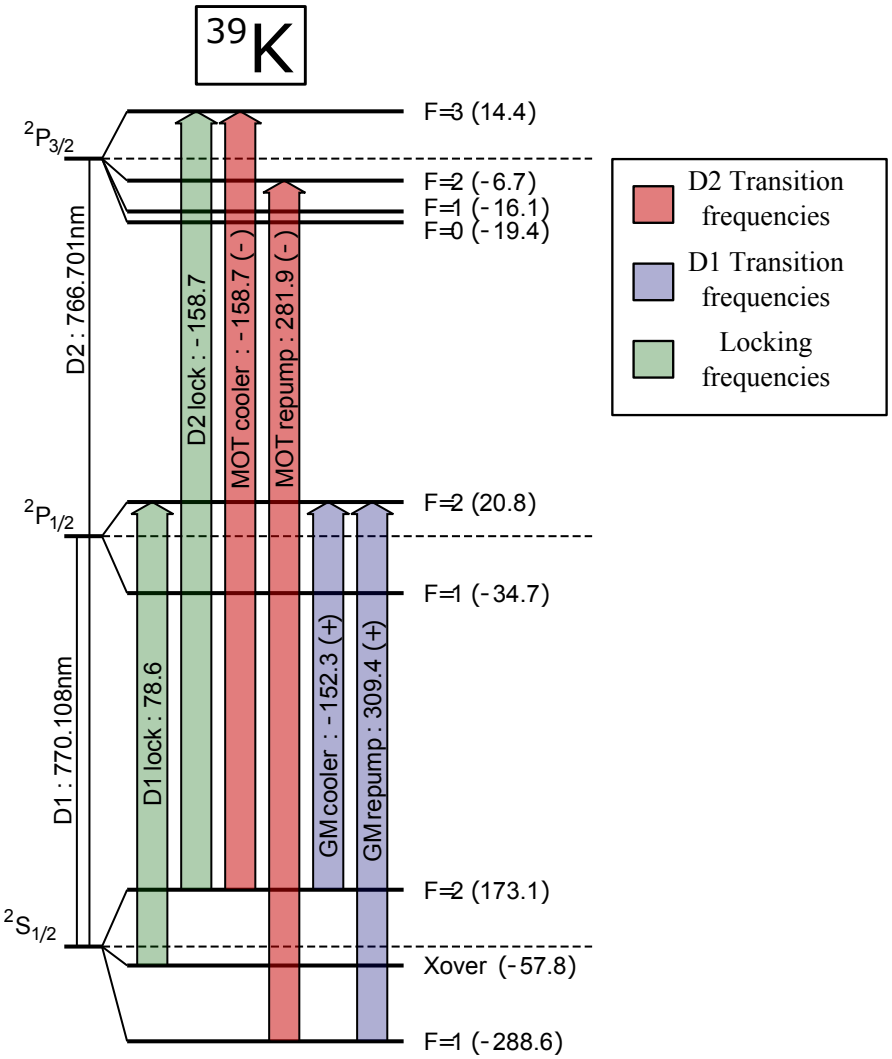

Fig. 3.2: Level scheme of potassium 39 and laser beam frequencies for the MOT and for the gray molasses. (Image reproduced from [111]) Two main transitions D1 and D2 transitions in ^{39}K respectively: $|4S_{1/2}\rangle \rightarrow |4P_{1/2}\rangle$ and $|4S_{1/2}\rangle \rightarrow |4P_{3/2}\rangle$ are represented with their corresponding hyperfine splitting. The blue arrows depict the cooling and repumping beam for the D1 transition while the red arrows represent the cooling and repumping beam frequencies for the D2 transition. The green arrows show the two frequencies (for the D1 and D2) that are used for locking the two lasers to the spectroscopy signal. Figure adapted from [120, 121]

through an acousto-optical modulator (AOM) which is aligned in a double pass configuration to shift the frequency of light to address the corresponding transitions (see schematic in figure 3.3). The ratio of the powers of cooler and repumper laser light is optimised using waveplates and beam splitters as described in [126]. The resultant light is then coupled to fibers that are aligned along the three axes of the vacuum chamber to cool and trap as explained in the following sections. The current setup is flexible for changing the frequencies by re-adjusting the diffraction order of some of the AOMs that are aligned in double pass configuration as described in [126].

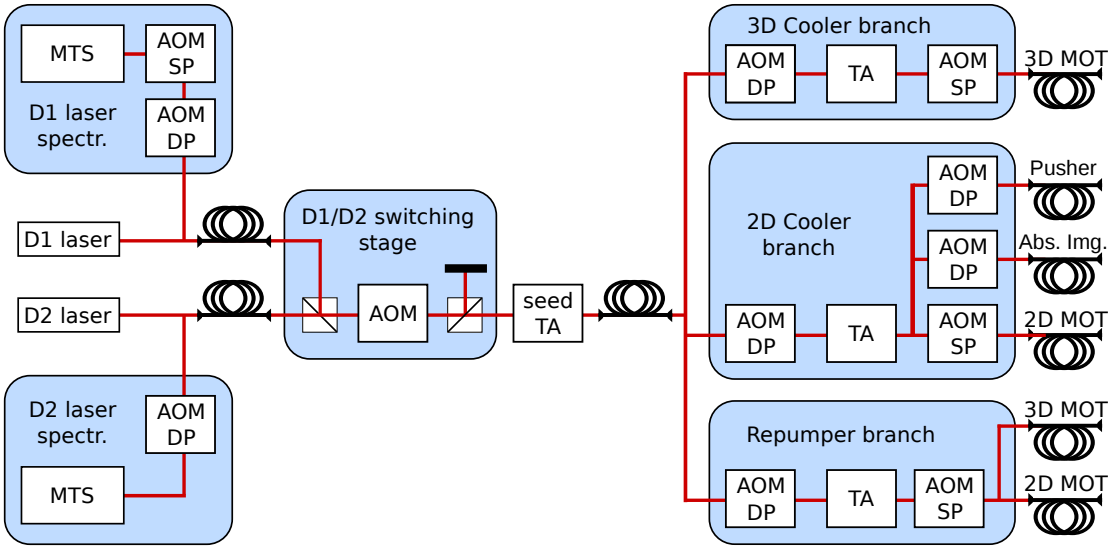

Fig. 3.3: A compact and versatile laser system for cooling and trapping. A schematic of the beam distribution of the laser system and the power amplification with all the necessary components such as tapered amplifiers, diode lasers and accousto-optical modulators for cooling and trapping in magneto optical trap (MOT). Image adapted from [121].

Atomic source

The potassium atomic source is a dispenser [7] fixed in a glass cell (shown in figure 3.1). It is heated by a DC current of ≈ 2 A, increasing the vapor pressure of atomic potassium inside the glass cell from the dispenser. Cooling of these atoms within the glass cell has been done using a two-dimensional magneto optical trap (2D MOT) and then pushed into the vacuum chamber to be trapped in a 3D MOT.

[7] Alvatec AS-3-K-100-F

Magneto-Optical Trap

Mechanism of the magneto optical trap (MOT) [127] utilises the velocity dependent absorption of photons by atoms. The spontaneous emission of these photons in turn reduces the kinetic energy of atoms. A combination of a magnetic field gradient with red-detuned circularly polarised light is used to confine the atoms spatially. The atoms that try to move out of the trap, the magnetic field gradient creates a Zeeman shift in the atomic states making them undergo a cooling transition on resonance which creates a scattering force that pushes the atoms towards the center of the MOT where the magnetic field value is zero. For this process, two different transitions are used: one is called as repumper i. e. $|4S_{1/2}, F = 1\rangle \rightarrow |4P_{3/2}, F = 2\rangle$ and the other is cooler i. e. $|4S_{1/2}, F = 2\rangle \rightarrow |4P_{3/2}, F = 3\rangle$ (see figure 3.2). This is to prevent the accumulation of atoms in one of the hyperfine ground states.

As mentioned in the previous section, the 2D-MOT consists of a glass cell where atoms are cooled down in transverse direction by four laser beams in each direction i.e. eight retro-reflected beams [128]. These relatively cool atoms are then directed into the 3D-MOT. To push the atoms towards the center of the vacuum chamber an additional beam resonant with cooling transition has been used which is called the pusher in figure 3.1. Later in the vacuum chamber, the atoms are exposed to six counter-propagating beams (that are obtained from the combination of both the repumper and cooler light using a homebuilt structure [126]). Additionally, a magnetic quadrupole fields, generated by a pair of coils in an anti-helmholtz configuration, is used to control the spatial confinement of the atoms. The temperature of atomic cloud at this stage is reduced to a few mk. A large spatial overlap between the MOT and the dipole trap is necessary to enhance the atom loading into the dipole trap. But the MOT is a few mm in size to enable fast, efficient loading from the 2D MOT. Unfortunately the optical dipole trap only has a size of hundreds of μm which makes the spatial overlap, and therefore transfer between the 3D MOT and the dipole trap very poor. Hence, an intermediate step has been added to reduce the MOT size by reducing the spatial distribution of atoms inside the MOT for their efficient loading into the dipole trap. This is done by ramping up the gradient of magnetic field making the spatial confinement of atoms inside the MOT tighter. Concurrently, the detunings of the cooler beam and the repumper beam have been adapted in order to compensate the additional

splitting of energy levels due to the increased magnetic field. This step is called the compressed MOT. Due to the finite trap depth of the dipole trap $\approx 50\ \mu$k, atoms coming from the compressed MOT need to be at lower temperatures in order to not leave the dipole trap. Therefore, we have introduced an additional cooling technique called the gray molasses in order to further cool the atoms which is described in section below.

Gray molasses

In this technique [129], the transitions are driven from ground states to excited states using blue detuned laser light where one of the ground states is dark meaning it gets decoupled from the light. For this, the total angular momentum of the two coupled hyperfine states should be such that $F \leq F'$, where $'$ denotes the excited state. The light field which addresses the transition between these hyperfine states should be circularly polarised and counter-propagating in order to have the bright states experiencing an oscillatory potential [130]. When an atom moves through this oscillatory potential, it increases the probability of being excited by climbing up the potential hill and losing its kinetic energy. Later, it decays either to the dark state or to one of the bright states to undergo the same cycle. This technique is also called the Sisyphus cooling [130]. Instead of getting accumulated in the dark state, the atoms can return to the oscillating potentials of bright states via motional coupling. A detailed development of this technique for ^{39}K is given in [131, 132]. The D1 transition has been used due to larger hyperfine splitting as compared to the D2 to be able to finely resolve the addressed states (see figure 3.2). The corresponding blue-detuned repumper and cooler transitions that have been involved to drive each of the hyperfine ground states are: $\left|F = 1, m_f\right\rangle \rightarrow \left|F' = 2, m_f\right\rangle$ (repumper light) and $\left|F = 2, m_f\right\rangle \rightarrow \left|F' = 2, m_f\right\rangle$ (cooler light), where: $F \leq F'$. With this process, we are able to further cool down the MOT atomic cloud to tens of μK. This allows us to maximise the loading of atoms into the dipole trap.

3.2.3 Optical dipole trap

As the trapping potential is directly proportional to the the laser intensity and inversely proportional to the laser detuning [107], it is necessary to compensate a large detuning (to reduce off-resonant scattering) with a high intensity laser. More details on this technique of optical dipole trap are given in chapter

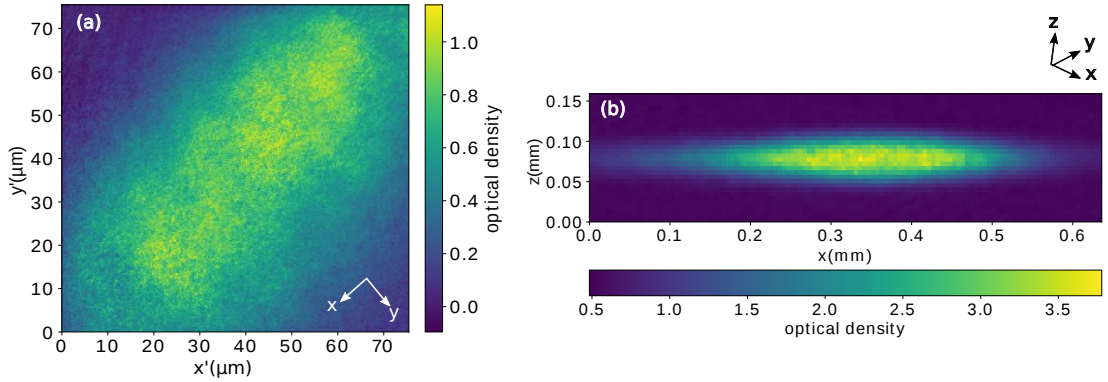

Fig. 3.4: Absorption image of ^{39}K in a pancake-shaped optical dipole trap: Atoms are loaded into the pancake-shaped optical dipole trap from the compressed MOT during the cooling stage through gray molasses. **(a)** High-resolution absorption image of the atom cloud trapped in the pancake shaped optical dipole trap trap. The image is taken from the top along the z axis. **(b)** Side absorption image of the atom cloud trapped in the pancake shaped optical dipole trap at the end of a time of flight. The image is taken along the y axis.

2. In our experiments we use a Mephisto MOPA laser, that includes four amplification stages, having an Nd:YAG crystal that works as a resonator with the end faces as mirrors and a stable low-power single-frequency laser diode. The maximum output power is $\approx$ 55 W and a wavelength of 1064 nm. We derive a part of the light from this 1064 nm laser system to produce a pancake shaped optical dipole trap to confine the atoms in the vertical direction in the focal plane. The optical setup of this pancake trap includes two cylindrical lenses to stretch the beam in z and x respectively and the two spherical lenses to collimate and focus this beam on to the atoms in the vacuum chamber. The Gaussian widths extracted of the atomic cloud from this pancake trap are σ_x = 29 μm and σ_y = 75 μm (details in [133, 134]). In this trap we perform the main experiments presented in the framework of this thesis. Figure 3.4 shows an absorption image of the atoms trapped in the optical dipole trap. To load the atoms into this trap, we use the gray molasses cooling technique to cool and load the atoms simultaneously. For the optimized atom loading, the detunings of cooler as well as repumper beams are scanned and we measure the optical density of the atomic cloud after the expansion for atomic cloud with trap-off for few ms. Detailed characterization of the gray molasses in our system is described in the master thesis [133, 134]. The final outcome is an atomic cloud with $\sim 10^5$ atoms, where atomic density is $\approx 2 \times 10^5$ cm^{-3} and at typical temperatures of $\approx$ 20 μK.

3.3 Digital micromirror Device

From this section onwards, I discuss in detail the integration of the DMD into our existing cold-atomic apparatus.

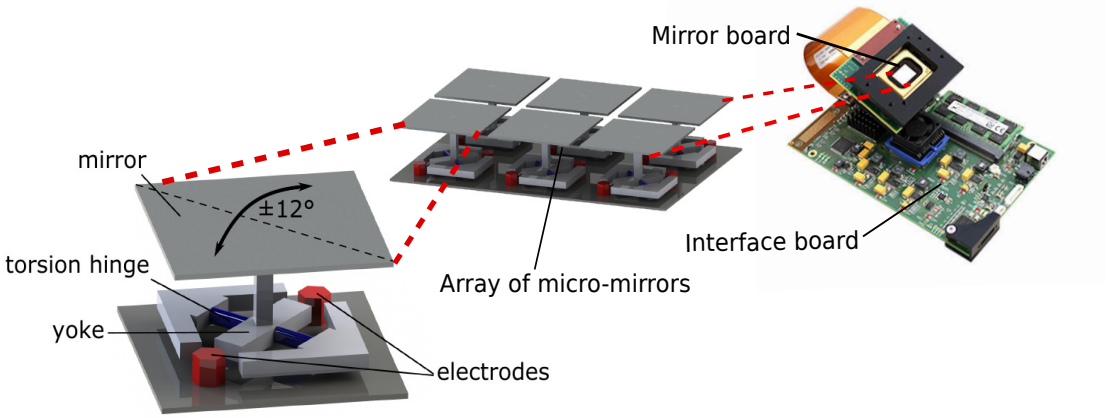

Fig. 3.5: Schematic of DMD Digital micromirror device where all of the 1024 × 768 mirrors are situated on a rectangular mirror board of about 1.5 cm^2 along with the zoomed-in part of the mirror array showing their tilt of $\pm 12^\circ$ across the diagonal axis of the micromirror referring to the ON/OFF state of the device (Image adapted from [135, 136])

3.3.1 Why we use a DMD ?

Basically, both SLMs and DMDs can create arbitrary traps and suitable for our application. However, DMD does not have any flickering problem which is helpful to avoid any noise on the created traps. DMD is free from phase errors per pixel and cross-talking between pixels. A DMD is static [136], once we set binary pattern it's fixed and we know exactly what pattern it is. Second, a DMD can switch at high rate, switching rate: DMD $\approx$ 20kHz [136].

The advantage of an SLM is the power efficiency if both an SLM and a DMD are used in Fourier frame. In such configuration, power efficiency of DMD is only a few percent. But that of an SLM can be $> 90\%$. That's why in our setup we planned to put DMD in image plane. This configuration has larger power efficiency (it depends on illumination ratio) and straightforward implementation. The imaged pattern is exactly printed on DMD. Of course we have to pay the price of no phase control and of no correction for aberration. The tweezer platform that we have realized using DMD addresses following advantages:

- High scalability: $>$ 450 microtrap sites
- Flexible control over spatial trap geometry in 2D
- Arbitrary tweezer trap separation as opposed to optical lattices which require interference effects
- Confinement of each trap within a Rydberg blockade radius.

In the previous chapter (section 2.1), I have described the mechanism to create a pancake-shaped optical dipole trap by exploiting the electric dipole interaction with far-detuned light. As DMD plays a crucial role in creating various exotic geometries of microtrap arrays, it is important to understand the functionality of DMD.

3.3.2 Working principles of DMD

As described in detail in [136], the DMD[8] consists of an array of about a million individual micromirrors shown in figure 3.5. The area of each micromirror is about 12.6 $\times$ 12.6 μm^2. Each micromirror is mounted on a yoke which is connected to a torsion hinge, see figure 3.5. DMD micromirrors have two tilt states i.e. the tilt of $\pm 12^\circ$ across the diagonal axis of the micromirror as shown in figure 3.5. These two angles indicate an ON and OFF configuration. Therefore the DMD is a binary device. The micromirrors reflect laser light in either of the two certain beam paths depending on the angle in which the mirrors are tilted. The position of the mirror is set through the two electrodes which are located under a diagonal of the micromirror. A dual CMOS memory is situated under each micromirror that complementorily defines the states of the two electrodes. As the memory gets loaded in the form of the state bits, one of the 2 electrodes gets assigned with bit 1 and another one with bit 0. Each micromirror and each yoke share a common potential that keeps the mirrors in its final position with the help of the electrodes, see [136, 137] for more technical details.

Once a mirror is set into its position, it will stay there until a new position is set. Depending on the model of the device, the maximum rate of switching for the micromirrors ranges from about 4 kHz to 32 kHz (in our case, it is $\approx$ 23

[8] Vialux V-7001 (micromirror array: 1024 $\times$ 768, micromirror pitch: 13.68 μm, Active mirror-array area: 14 $\times$ 10.5 mm^2, Damage threshold: 25 W/cm^2, Fill factor: 92 %)

kHz [135]). Depending on the model of the device, the maximum switching rate for the micromirrors ranges from 4 kHz to 32 kHz. The rectangular mirror board on which all the micromirros are placed has an area of ≈ 1.5 cm^2 that is termed as the ”active area”. To establish a communication between the mirror board and a computer, an another board called the ”interface board” is necessary. It consists of the required firmware and hardware with field programmable gate array (FPGA) that controls the behaviour of the entire device [136]. As the computer uploades pictures to DMD, it is this FPGA that receives them and translates the pictures into the required states of the micromirrors to set the micromirrors according to the generated states [136]. Generally, the interface board allows to save the pictures directly on the board itself using an on-board random access memory (RAM) [136]. This is necessary if the pictures are required to be displayed with a frame rate larger than allowed by the connection between the interface board and the computer [136].

Additionally an interface program comes with the interface board. This program allows a simple communication of the interface board with the computer through a USB connection. Using appropriate functions on the computer, the uploading of the pictures, their storage and the display of the sequence can be easily done [136]. While installing the DMD, one has to take care that each micromirror tilts around it's diagonal axis when switched ON as shown in figure 3.6. The incident laser light gets reflected out of the plane that is horizontal to the optical table around a rotational axis that is at an angle of 45° from the vertical. Hence, the DMD should be titlted by 45° such that the rotational axis of the micromirrors gets aligned in the vertical direction. This makes the micromirror to be flipped along the vertical rotational axis to keep the reflcted beam in the same horizontal plane as that of the optical table. Hence, we mount DMD in 45° plane in order to keep the principal beam parallel to the plane of our optical table. As the DMD chip is composed of many tiny mirrors that are placed adjacent to each other, the entire mirror area behaves as a two-dimensional blazed grating [136] as shown in figure 3.6. This makes the DMD to diffract an incident laser light into several diffraction orders [136] as shown in figure 3.6. We block the other orders so they don't affect the experiment. We can find out the main order of diffraction 'm' that carries large amount of intensity for the provided geometry of blaze grating

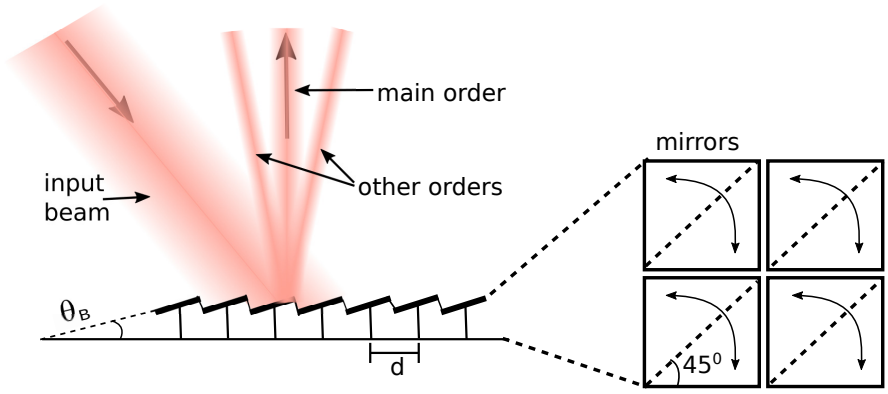

Fig. 3.6: DMD as a blazed grating The DMD mirrors constitute a blazed grating [136, 137]. Hence, an incident beam gets diffracted in different orders. Depending on the mirror spacing d, the mirror tilt angle and the wavelength of the laser light, a main order carries most of the reflected intensity and the other orders carry less. These mirrors tilt about its diagonal axis. The DMD should be mounted at 45° to keep the reflected laser beams in the same horizontal plane as that of the optical table.

under the blazing condition [136, 138],

$$2d(\sin\theta_B) = m\lambda. \tag{3.1}$$

where d is the spacing between the mirrors, λ is the wavelength of the laser and θ_B is the angle of tilt of the mirrors. only this main order m is used, to perform spatial light modulation. For a given m, we can follow the grating equation from [136, 138],

$$d(\sin\theta_{in} + \sin\theta_{out}) = m\lambda. \tag{3.2}$$

This relates the angle of the incident laser light θ_{in} in with the angle of the diffracted lightθ_{out} for the given m. Imposing the condition that the main diffracted order travels perpendicular to the area of the mirror. Hence, keeping $\theta_{out} = 0°$, we calculate the necessary θ_{in} in at which we make the beam incident on the DMD. The integration of DMD in the main experimental setup as a crucial component of our high resolution imaging system that focuses the DMD pattern on to the atomic plane has been discussed in the next section.

3.4 Integration of DMD in the high resolution imaging system

3.4.1 Imaging configurations of DMD

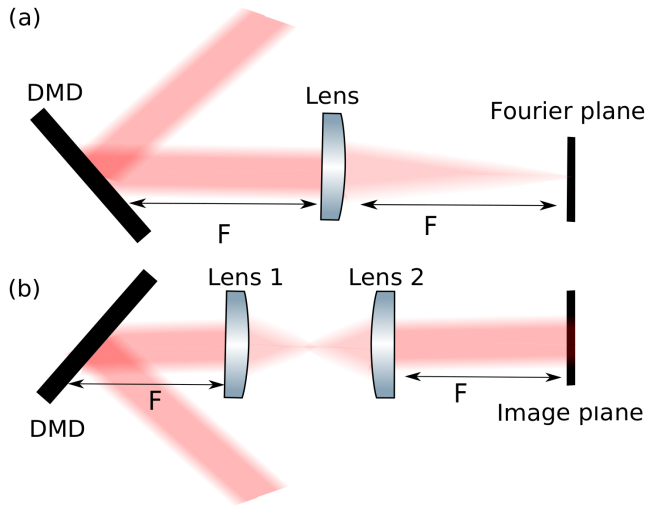

Fig. 3.7: Imaging configurations of DMD (a) Fourier plane of the DMD: The beam diffracted from the DMD is focussed in the Fourier plane of the lens shown. **(b)** Lens 1 focuses the incoming beam into a Fourier plane as above and then the lens 2 does the inverse-Fourier transformation of this beam to image the plane of the DMD pixels onto the plane of the image, where ultracold atoms are placed in the experiment [136].

There are mainly two configurations for integrating DMD in the high resolution imaging setup. One is the Fourier configuration as shown in figure 3.7. In this configuration, the light refracted from the DMD surface is Fourier transformed to the focal plane through a lens. The connection between the diffracted beam at the DMD mirror plane and the Fourier plane is given by the Fourier transformation, which is defined by a single lens.

The second configuration is to put DMD plane onto the so-called imaging plane. By this way, a direct mapping of the DMD plane onto the imaging plane is possible through a high-numerical objective lens as shown in figure 3.7. One advantage for imaging platform configuration is that if the effective pixel size of the DMD is much lower than the optical resolution, then the trap intensity can be adjusted accordingly. Another advantage is that it is possible to create infinitely sharp potentials i.e. box potential [136, 137]. Therefore, in our case, we chose the imaging plane configuration.

3.4.2 Estimating the resolution of the imaging system

Our main experimental set-up consists of a high-resolution imaging system as shown in figure 3.8. It is composed of DMD + two lenses of focal length 100 mm each forming a telescope with magnification = 1, an aspheric lens (also termed as "vacuum lens" in the figure 3.1) located inside the vacuum chamber with numerical aperture (NA) equal to 0.6 and focal length of 32 mm in combination with another lens of 1500 mm focal length (placed on a translation stage) to create an effective magnification of ≈ 53. This means the DMD pattern will be de-magnified by roughly 53 times to project on to the atomic cloud trapped in optical dipole trap. The effective DMD pixel size on the atom plane is 13.12/53 = 245 nm where 13.12 μm is a size of the DMD micromirror[8], and is obtained by multiplying DMD micromirror pitch[8] which is 13.68 μm with the fill factor of the DMD[8] which is 0.92. The resolution of this imaging system is set by the aspheric lens situated in the vacuum chamber (see figure 3.8) and can be estimated by the Rayleigh criteria as follows:

$$Resolution = \frac{0.61\lambda}{(NA)}. \tag{3.3}$$

Here λ = 780 nm, therefore the resolution is 0.79 μm. Due to this setup we cannot resolve a difference below 16 pixels of DMD in a square geometry, and thus this is the minimum we use. This implies that an area of 16 pixels of DMD is focused down to 0.79 μm^2 onto the atomic plane. An absorption shadow of the atoms from the tweezer traps is imaged onto a charge-coupled-device camera[9] using the same optics as used for the DMD light patterns. A dichroic mirror[10] is placed in front of the camera to differentiate between the 780 nm trap light and the 767 nm absorption imaging light.

The 780 nm laser system

As shown in figure 3.8, the light used to create the microtraps is obtained from the ECDL laser[11] at 780 nm with the output power of 50 mW. The power of the laser output is magnified to 2 W using a tapered amplifier[12]. The output light from the tapered amplifier is then fibre-coupled to make it incident on to the DMD plane. The output power of the light from the fibre is 300 mW. In

[9] Andor iXon Ultra 897 UCS-EXF
[10] Edmund optics: FILTER 769NM X 41NM BP 93T 25.0D
[11] Toptica DL pro
[12] Eagleyard: ETP-TPA-0780-03000-4006-CMT0

principle, the wavelength should be far-detuned from the resonant wavelength of the D2 atomic transition, for ^{39}K is 767 nm. However, we are limited by the coating of the aspheric lens. An AOM[13] is used for fast switching of this trap-light.

Image characterisation set-up

This is a test-setup (shown in figure 3.8) to characterise the tweezer trap patterns produced using DMD. Using a flip mirror after the lens of focal length 1500 mm, the trap beam of 780 nm is re-directed to an another aspheric lens (focal length of 32 mm) to de-magnify the DMD pattern by 53 times the original size. The resulting image is then observed on a beam profiler[15] using a microscope objective[14].

3.4.3 The pattern creator for DMD

To create the patterns to feed into the DMD, I have designed a Python based user interface to which we call "pattern generator". This interface includes a two dimensional array of zeros of the dimension 1024×768 that is the same as that of the array of the micromirrors of the DMD. Then this interface takes in an input of the number of pixels and the coordinates of the pixels inside a cluster of the DMD pixels which we want to switch ON onto the DMD plane. For different lattice geometries, the interface generates the coordinates of the lattice sites by itself by following the given lattice vectors for the given lattice periods, lattice dimensions and the number of pixels at each lattice sites. The interface then replaces the zeros from the two-dimensional array by ones at the given coordinates. This final two-dimensional array is then converted into a portable network graphics (.png) format where the black part of the image represents zeros of the array i.e. OFF - state of the DMD pixels and white color represents ones of the array i.e. the ON - state of the DMD pixels from which the light gets diffracted creating the desired pattern. These generated patterns are then fed to the DMD. Some examples of the created patterns are visualized in figure 3.9.

[13] AOMO 3110-120 Gooch and Housego
[14] Objective LD A-Plan 40x/0,55 Ph2 M27.

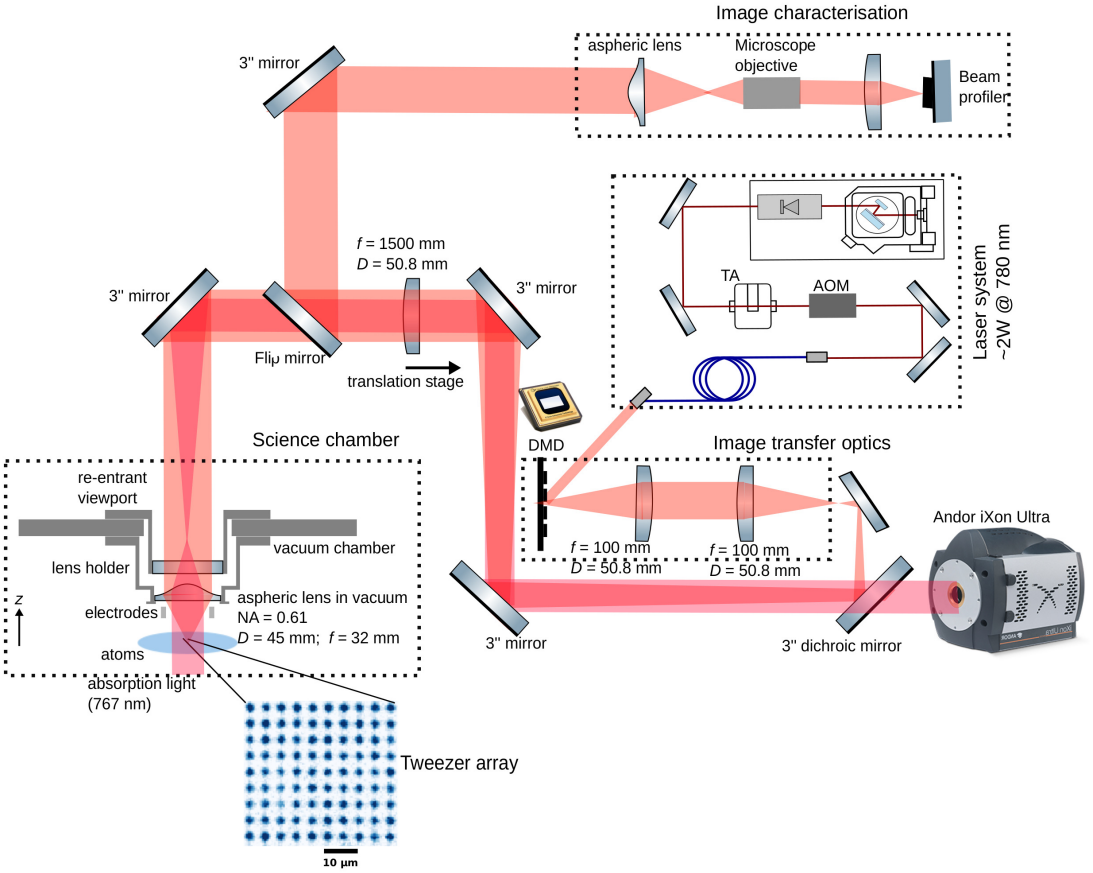

Fig. 3.8: Experimental setup showing the integration of DMD in the high resolution imaging system: The experimental setup shown above includes the imaging system for creating tweezer arrays consisting of **Image transfer optics**: DMD + two lenses of focal length 100 mm each forming a telescope with magnification = 1 then a lens with focal length of 1500 mm (situated on a translation stage) + an aspheric lens of focal length 32 mm inside the vacuum chamber (as shown in **Science chamber**) has an effective magnification of ≈ 53. Hence, at the focus of this high resolution imaging system is a DMD pattern that is de-magnified by 53 times to project on to the atomic cloud trapped in optical dipole trap. An absorption shadow of the atoms from the tweezer traps is imaged onto a charge-coupled-device camera[9] using the same optics as for the DMD light patterns. **The 780 nm laser system**: The light used to create the microtraps is obtained from the ECDL laser at 780 nm and the power of the laser output is magnified to ≈ 2 W using a tapered amplifier[12]. An AOM is used for fast switching of this trap-light. **Image characterisation**: This is a test-setup to characterise the tweezer trap patterns produced using DMD. Using a flip mirror after the lens of focal length 1500 mm, the trap beam of 780 nm is re-directed to an another aspheric lens (focal length of 32 mm) to de-magnify the DMD patterns by 53 times. The resulting image is then observed on the beam profiler[15] using a microscope objective[14].

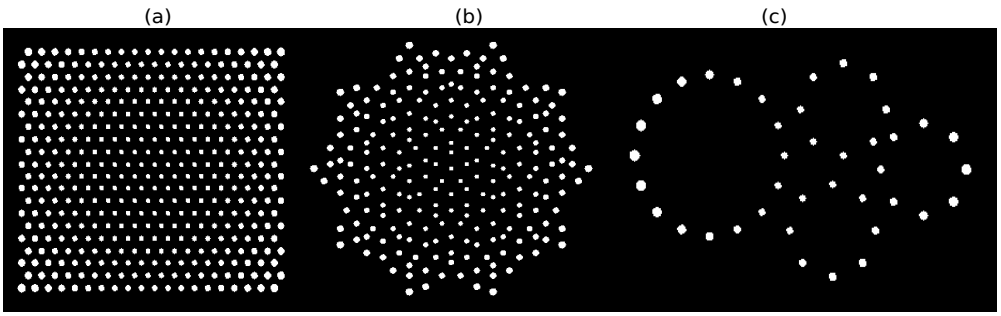

Fig. 3.9: Patterns of the format portable network graphics (.png) generated by a Python based user interface to feed to the DMD (a) Triangular lattice of dimension 20 ×20. **(b)** 226 site Penrose quasicrystal lattice. **(c)** 40 site ring structure. For all the three patterns, the pixels at each site follows an inverted Gaussian profile with A_{min} = 22, 25, 30 as described in the subsection 3.4.5.

3.4.4 Characterisation of an individual intensity pattern created by DMD

To observe the variation of Gaussian width of the intensity profiles generated by DMD, we vary the number of pixels in the microtrap. We start with the DMD cluster of 10 pixels. This means, we project a pattern of cluster size 10 pixels created using DMD on to the beam profiler[15]. We do the same process as above for different cluster sizes starting from 20 pixels to 100 pixels. We fit the resulting profiles with a Gaussian distribution and extract the width. Figure 3.10c displays a plot of the fitted Gaussian widths for different pixel cluster sizes. From this we can see that the smallest size of the cloud that we could achieve $\approx$ 0.8 μm and that is $\approx$ 16 pixels in the DMD plane as illustrated in figure 3.10. This data imply that using more pixels will give us more power at the edge of the Gaussian distribution but will degrade the resolution.

3.4.5 DMD pattern adaptation

The resolution of the imaging system puts a limit on the minimum number of pixels of DMD below which we cannot differentiate and that limit is 16 pixels. This provides us 16 adjustable intensity levels below resolution limit. Given that the effective pixel size of the DMD is much smaller than the optical resolution of the imaging system (see subsection 3.4.2), it allows us to generate uniformity in the trap-depths across large arrays of microtraps. This is done

[15]LBP2-HR-VIS2: array 1928*1448, pixel size 3.69 µm, sensor size 7.1*5.3 mm, resolution 37 µm $\sim$ 10 pixels

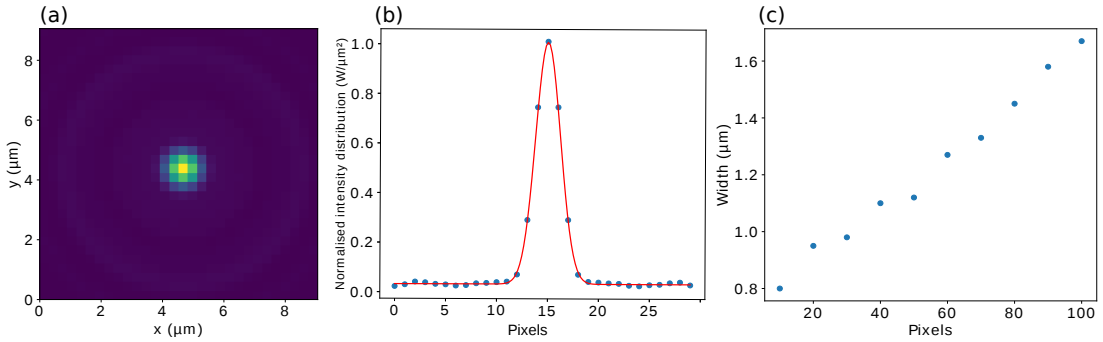

Fig. 3.10: Point spread function and intensity profile width of the DMD clusters with different pixels (a) The point spread function of the single pixel on DMD showing the optical resolution of ≈ 0.8 μm. **(b)** A Gaussian fit to the crossection of the point spread function. **(c)** Gaussian width of the intensity profiles created using the DMD by varying the number of pixels in the DMD cluster

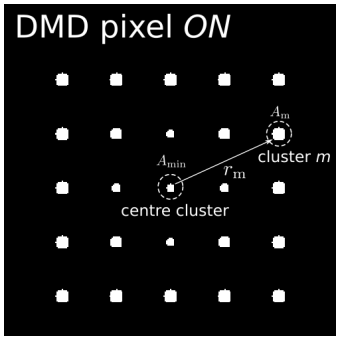

Fig. 3.11: DMD pattern adaptation. To maintain the uniformity in the trap depths of microtraps, we compensate for the Gaussian intensity profile of the microtrap laser. In the DMD plane, the number of pixels are adjusted in each DMD cluster A_m based on its distance(r_m) from the cluster at the center of the illumination A_{min} following the inverted Gaussian dependence $A_m = A_{min} \exp(g r_m^2)$. The figure depicts a square microtrap array of 5×5 with A_{min} = 20 pixels and A_m = 60 pixels with period = 4 μm. The parameter 'g' is manually adapted in the experiment to get equal optical depth.

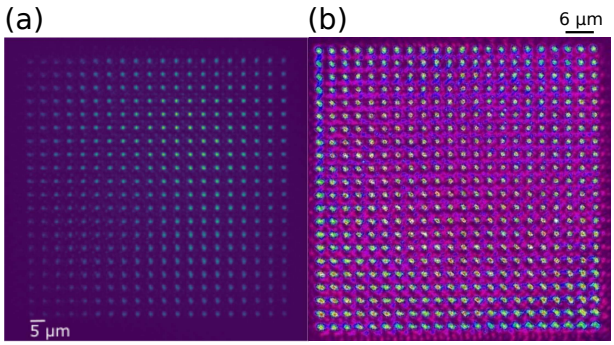

Fig. 3.12: Intensity profiles with and without Gaussian compensation. (a) An intensity profile observed on a beam profiler [15] created by DMD without using any Gaussian compensation i.e. parameter 'g' = 0. This image shows a 20 × 20 square lattice with lattice period of 5 μm. **(b)** An intensity profile of 22 × 22 square lattice created by DMD using the Gaussian compensation with A_{min} = 20 pixels and the parameter 'g' = 1.2 and the lattice period of 3 μm.

by compensating the Gaussian intensity distribution of the microtrap light. To do this, we adjust the number of pixels in each DMD cluster based on its distance from the center of the illumination following an inverted Gaussian dependence $A_m = A_{min} \exp(g r_m^2)$ as shown in figure 3.11. Some examples of the intensity profiles with and without using Gaussian compensation are shown in figure 3.12. The effects of this pattern adaptation on the uniformity of the trap depths are discussed in terms of the uniformity in loading of atoms across the large array of the tweezer traps in chapter 4 in section 4.2.

Intensity pattern gallery

When we feed an image file (.png) to DMD using the user interface (see subsection 3.4.3), the corresponding intensity patterns get generated by DMD after the light diffracts from the DMD surface. We observe this pattern using the beam profiler[15]. Some examples of the intensity patterns which are generated by DMD are shown in figure 3.13. The test-setup (shown in figure 3.8 in the box "image characterisation") has been used to observe these intensity patterns.

3.5 Estimation of microtrap parameters

Here we estimate the trap depth, the trap frequency and the scattering rate of the potassium-39 atoms in their ground state $4S_{1/2}$ as a function of the trap laser wavelength for different trap laser powers and waists to determine what

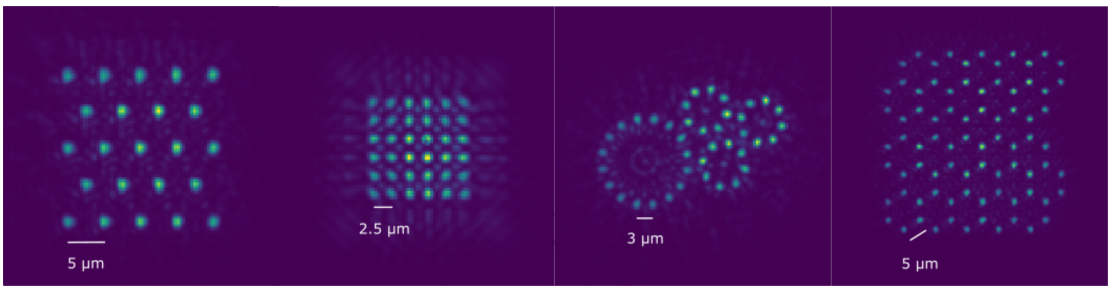

Fig. 3.13: Intensity patterns produced by DMD. From left to right: Triangular lattice (5×5), square lattice (6×6), the structure of light harvesting complex, Hexagonal lattice (6×6).

laser wavelengths and corresponding powers we need for microtraps. We want to maximize the trap frequency as it provides the better confinement of the atoms within the trap [107] and we want to lower the scattering rate for longer lifetime of atoms in the trap [107] (see figure 4.4d from chapter 4 for the lifetime measurements of the atoms in the microtrap). I assume a Gaussian intensity profile of the trap laser with the radial waist ω and power P.

In principle, as the scattering rate (R_{scat}) scales as $R_{scat} = \Gamma/(\hbar\Delta) \times$ trap-depth [107], it is beneficial to increase the detuning of the trapping laser from the $4S_{1/2} \rightarrow 4P_{3/2}$ transition of wavelength 767 nm and compensate the reduced trap depth by increasing the power of the trapping laser. However, we are limited by the aspheric objective lens on how much we can detune from 767 nm without losing too much optical resolution where the limit for the aspheric lens is set at 780 nm above which the resolution is degraded [139]. The estimation is plotted

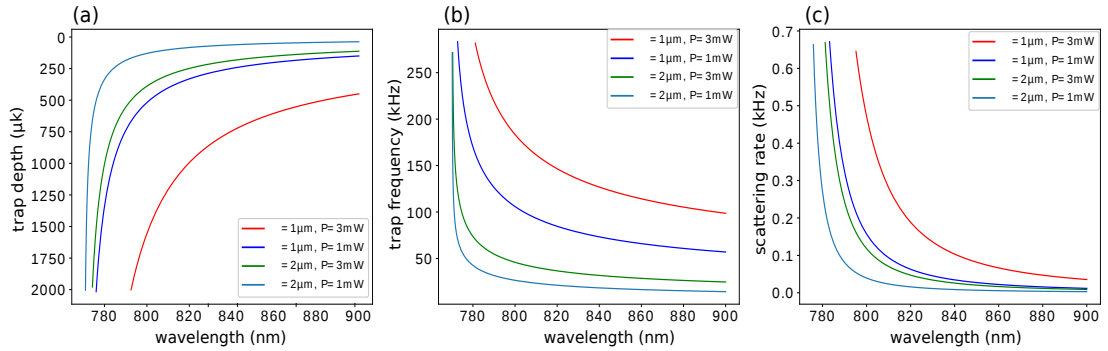

Fig. 3.14: Estimation of microtrap parameters. We make the choice of trap-wavelength of 780 nm to generate microtraps. From figure (a), we can see that the trap depth at 780 nm is ≈ 1 mK and trap-frequency of around 100 kHz, (figure (b)) which belongs to the beam waist in between 1-2 µm as the optical resolution is ≈ 1 μm (see figure 3.10) and power of around 1-2 mW as power efficiency of DMD is only a few percent of the incident power of the laser light [135] but a relatively higher photon scattering rate (figure (c)).

in figure 3.14. According to these plots, we choose 780 nm light to create microtrap. Because 780 nm is closer to the D2 resonance, so we get stronger atom-light interaction. Then for same amount of power we get deeper trap (to trap more atoms). The trap depth at 780 nm is $\approx$ 1 mK and trap-frequency of around 100 kHz which belongs to the beam waist in between 1-2 µm as the optical resolution is $\approx$ 1 μm (see figure 3.10) and power of around 1-2 mW as the power efficiency of DMD is only a few percent of the incident power of the laser light [135], but a relatively larger photon scattering rate (see figure 3.14c).

3.6 Summary

Following a brief overview of the vacuum apparatus, laser cooling and trapping techniques, I have described the integration of the DMD in the high resolution imaging system emphasizing three aspects: overview of the basic DMD technology, optical setup, and generation and characterisation of useful trapping configurations With the DMD technology, we are able to create hundreds of programmable arrays of optical tweezer traps. The resolution that we achieve is $\approx$ 1 μm that corresponds to approximately 4 pixels on the DMD plane. To maintain the uniformity of trap depths across the large arrays of microtraps, DMD patterns are adapted following an inverted Gaussian expression to compensate the Gaussian profile of the DMD illumination beam. The estimated trap depth is $\approx$ 1 mK, trap frequency is $\approx$ 100 kHz.

With this technology for creating large arrays of microscopic tweezer traps, the next chapter gives the full description of our novel approach of loading of the atoms into the microtraps created by the DMD by exploiting elastic collisions and the step-by-step characterisation of the loading process.

Chapter 4

Characterisation of hundreds of microscopic atomic ensembles

The work presented and reproduced in this chapter has been published in the following article:
Preparation of hundreds of microscopic atomic ensembles in optical tweezer arrays
Y. Wang, S. Shevate, T. M. Wintermantel, M. Morgado, G. Lochead and S. Whitlock
npj Quantum inf 6, 54 (2020).

In this chapter, I describe a novel approach to prepare large and uniformly filled arrays of hundreds of tweezers with large occupation numbers in a single step. This is based on the technology described in chapter 3, which enabled the realisation of large and almost uniformly filled array exemplified by the 400 site triangular array shown in figure. 4.1a, as well as more exotic geometries such as connected rings (figure. 4.1b) and quasi-ordered geometries (figure. 4.1c). These examples were chosen since they exhibit structures on different length scales making them difficult to produce using other methods such as use of optical lattices [140]. Our approach exploits elastic collisions transferring ultracold atoms from a quasi-2D optical reservoir trap into an array of optical tweezers produced by a digital micro-mirror device (DMD)To realize large arrays, it was necessary to optimize the loading process and the homogeneity across the lattice by adapting the DMD light patterns to control the trap depth of each tweezer. A key finding is that each atomic ensemble is localized well

within the typical Rydberg blockade volume $\sim 1\ \mu m^3$ and the typical inter-trap separations of several micrometers are compatible with Rydberg-blockade gates. Each atomic ensemble has a controllable occupation from 20 to 200 atoms and the fluctuations of the number of atoms in each tweezer is comparable to or below the shot-noise limit for uncorrelated atoms. This makes the system well suited for quantum simulation of quantum spin models [46, 47, 141–147] and dynamics [148–155] in novel geometries, as well as for realizing quantum registers with collectively enhanced atom-light interactions for quantum information processing [44, 143, 156–159].

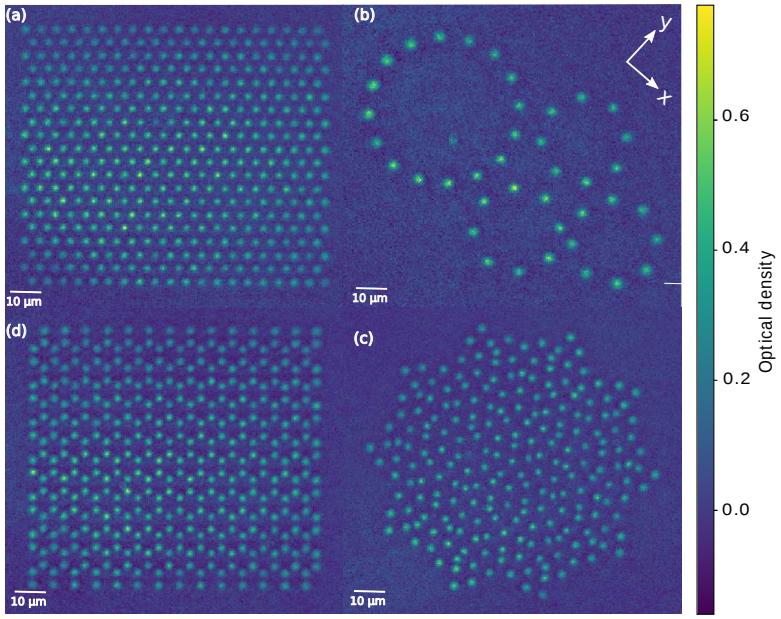

Fig. 4.1: Realization of large tweezer arrays with large occupation number in each tweezer. (a) Experimental absorption image of 400 site triangular lattice, where each spot corresponds to a microscopic ensemble of ≈ 30 ultracold ^{39}K atoms. The lattice spacing is $4\,\mu$m and the apparent size of each spot is $\sim 0.75\,\mu$m ($e^{-1/2}$ radius), mostly limited by recoil blurring during imaging. (b) 40 site ring structure (c) 226 site Penrose quasicrystal lattice. To improve the signal-to-noise ratio each image is an average of 20 absorption images (d) 196 site honeycomb lattice (see figure 4.3a for a typical single shot image).

4.1 Optimization of atom loading in tweezer traps

The experimental cycle starts with a three-dimensional magneto-optical trap (MOT) loaded from a beam of ^{39}K atoms produced by a two-dimensional MOT. This is overlapped with a far off-resonant pancake-shaped reservoir trap created by a 1064 nm single mode laser with a power of 16 W tightly focused by a cylindrical lens. The beam waists are $\omega_z = 7.6\,\mu$m, $\omega_x = 540\,\mu$m and

$\omega_y = 190\,\mu$m and the estimated trap depth is 330 μK. To maximize the number of atoms in the reservoir we apply an 8 ms gray-molasses cooling stage on the D_1 transition [131], yielding 3.3×10^5 atoms in the $|4s_{1/2}, F = 1\rangle$ state at an initial temperature of 45 μK.

Next we transfer the atoms to the tweezers from the reservoir trap. To generate the tweezers we illuminate a DMD with a collimated 780 nm Gaussian light beam with a 4.3 mm waist and a peak intensity of $1.44\,\mathrm{W/cm^2}$. We directly image the DMD plane onto the atoms with a calibrated demagnification factor of 53, using a 4f optical setup involving a 1500 mm focal length lens and a 32 mm focal length lens. The latter is a molded aspheric lens with a numerical aperture of 0.6, located inside the vacuum chamber. With this setup, each $(13\,\mu\mathrm{m})^2$ pixel of the DMD corresponds to $(245\,\mathrm{nm})^2$ in the atom plane. The details of the involved experimental set-up to realise the large arrays of tweezer traps can be found in chapter 3 (figure 3.8) (similar optical setup to Refs. [118, 160]).

The DMD can be programmed with arbitrary binary patterns to control the illumination in the atom plane. To generate the tweezer arrays shown in figure 4.1a-c we create different patterns of spots where each spot is formed by a small disk-shaped cluster of typically $A = 20 - 100$ pixels. To detect the atoms we use the saturated absorption imaging technique [161, 162]. The probe laser is resonant to the $4s_{1/2} \rightarrow 4p_{3/2}$ transition of ^{39}K at 767 nm and with an intensity of $I \approx 2.1 I_{\mathrm{sat}}^{\mathrm{eff}}$. The atoms are exposed for 10 μs and the absorption shadow is imaged onto a charge-coupled-device camera[1] using the same optics as for the DMD light patterns (figure 3.8). The fact that we are able to read out the atomic distribution in 10μs is an important advantage over the single atom tweezer experiments. The resulting optical depth of an image is well described by a sum of two-dimensional Gaussian distributions. The optical depth is defined as $OD = \ln(\frac{I_f}{I_i})$ where I_i is the initial intensity of the probe laser without the presence of the atoms and I_f is the final intensity of the probe laser in the presence of the atoms.

4.1.1 Estimation of atom number per tweezer

To determine the number of atoms, we fit the two-dimensional Gaussian distribution function as shown here to each of the tweezer sites visible from

[1] Andor iXon Ultra 897, active pixels: 512 x 512, pixel size: 16 x 16 μm^2, frame rate: 56 fps

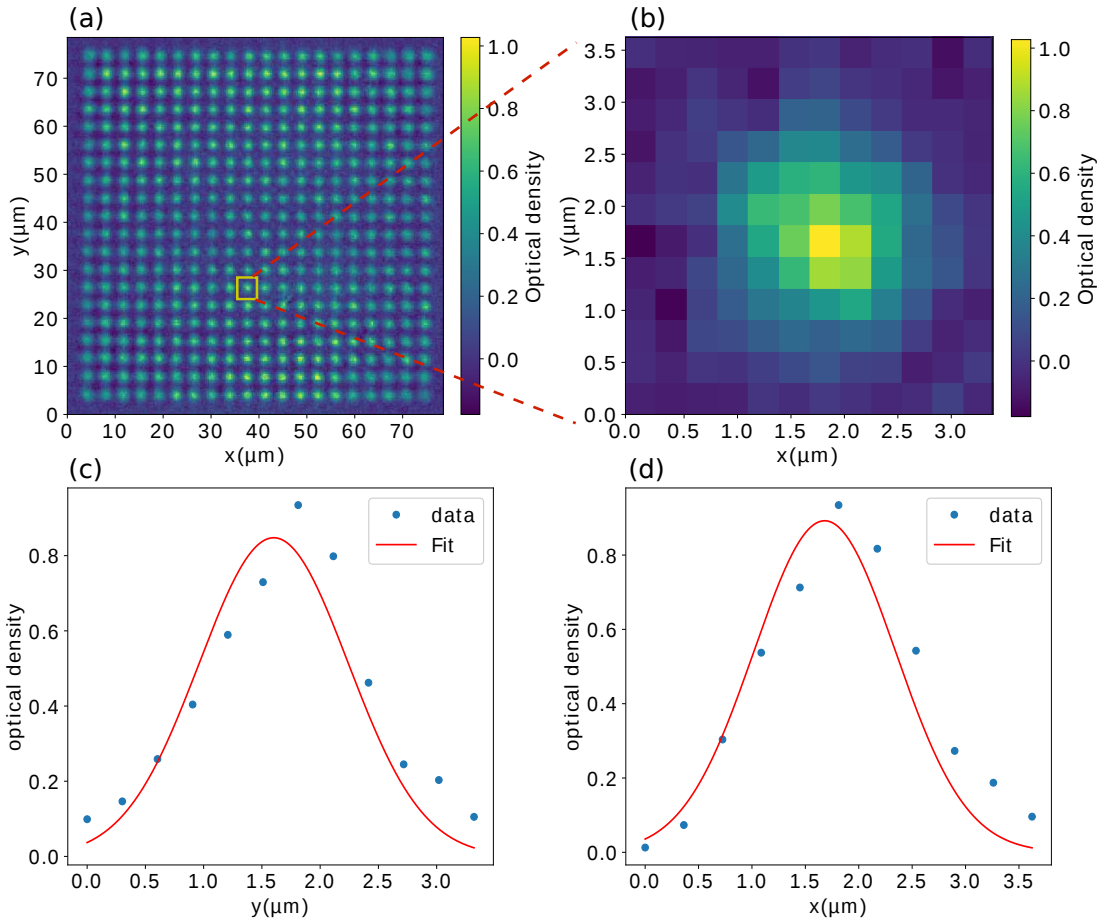

Fig. 4.2: Estimation of number of atoms in each tweezer. (a)Experimental absorption image of a 400 site square lattice, where each spot corresponds to a microscopic ensemble of ≈ 30 ultracold ^{39}K atoms. The lattice spacing is 3.5 μm and the apparent size of each spot is $\sim 1\,\mu$m ($e^{-1/2}$ radius) (b) Zoom-in of the marked spot. (c) Vertical-crossection of the marked spot with the fit of 2d Gaussian function. (d) Horizontal-crossection of the marked spot with the fit of 2d Gaussian function. By finding the fit results of σ_x, σ_y , we obtain the width of atomic cloud in x and y direction and the fit results of the amplitude of this function conveys the optical depth (OD) of the cloud. With these parameters, the number of atoms in each atomic cloud per tweezer are estimated (equation 4.5).

the absorption image (shown in figure 4.2).

$$f(x,y) = A \exp\left(-\frac{(x-x_0)^2}{2\sigma_x^2} - \frac{(y-y_0)^2}{2\sigma_y^2}\right) \tag{4.1}$$

Here x_0 and y_0 represent the position of a tweezer. The fit results of this function to each site gives us the best fit values of x_0 and y_0 that represent the position of each tweezer in the image plane. By obtaining result of the best fit value of the width of the Gaussian (σ_x and σ_y), the width of the atomic cloud within each tweezer is estimated as, $(\sigma_x)_{cloud} = \frac{P_x}{M} \times \text{fit}(\sigma_x)$ and $(\sigma_y)_{cloud} = \frac{P_y}{M} \times \text{fit}(\sigma_y)$ where $P_x = 16\mu$m and $P_y = 16\mu$m are the size of pixel of charge-coupled device camera[1] that we use to image the absorption shadow of atoms (absorption imaging). M = 53 is a magnification factor of our optical system as mentioned in Chapter 3. The optical depth ($OD(x,y)$) is estimated from the best fit of the amplitude (A) of the 2d Gaussian function (equation 4.1). We can understand the calculation of the number of atoms within each tweezer by following the approach from [161] by considering the Beer's law in the presence of saturation effect and for a resonant incident light as,

$$\frac{dI}{dz} = -n(x,y,z)\ \sigma(I)\ I \tag{4.2}$$

where $\sigma(I) = \frac{\sigma_{abs}}{\alpha} \frac{1}{1+I/I_{sat}^{eff}}$ is the effective absorption cross section including saturation correction α. $n(x,y,z)$ is the spatial atomic density of the cloud. Rearranging equation 4.2 and integrating it to both sides as,

$$-\int \frac{dI}{I} = \int \sigma(I)\ n\ dz \tag{4.3}$$

where OD = $-\int \frac{dI}{I}$ which is then equal to $\sigma(I)n(x,y)$ as obtained from the above integration. Integrating OD over x and y gives us the total number of atoms N as,

$$\frac{\int\int OD\ dx\ dy}{\sigma(I)} = \int\int n(x,y)\ dx\ dy = N \tag{4.4}$$

$$\text{Number of atoms}(N) = \frac{2\pi\ (\sigma_x)_{cloud}\ (\sigma_y)_{cloud}\ OD}{\sigma_{abs}} \alpha(1 + I/I_{sat}^{eff}) \tag{4.5}$$

where $\alpha(1 + I/I_{sat}^{eff})$ is a correction factor and it turns out to be 1 for our imaging system. The factor for saturation correction α accounts for corrections due to certain conditions during imaging [161] and that α = 1.38 for our experimental conditions. The σ_{abs} is an absorption cross section on resonance which is

expressed as

$$\sigma_{abs} = \frac{\hbar\omega_L\Gamma_K}{2I_{sat}} \tag{4.6}$$

where ω_L is an angular frequency of the laser that addresses D2 transition of ^{39}K. I_{sat} is a saturation intensity of D2 transition of ^{39}K which is 17.5 W/m^2. Γ_K is a natural linewidth of D2 transition of ^{39}K which is equal to $2\pi \times 6$ MHz. Substituting $\omega_L = \frac{2\pi c}{\lambda_K}$ and $I_{sat} = \frac{\pi hc\Gamma_K}{3\lambda_K}$ into equation 4.6, we obtain $\sigma_{abs} = \frac{3\lambda_K^2}{2\pi}$ with λ_K being the wavelength resonant with the D2 transition of ^{39}K which is 767 nm and c is the speed of light in vacuum.

4.1.2 Single shot detection sensitivity

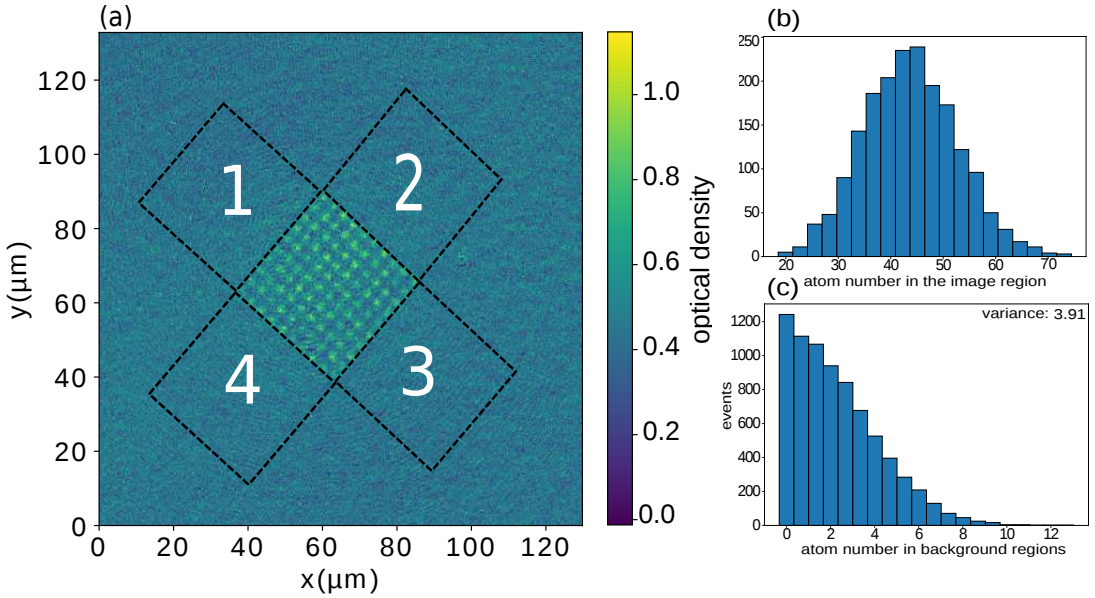

Fig. 4.3: Estimation of single shot detection sensitivity (a) Experimental absorption image of a 100 site square lattice, where each spot corresponds to a microscopic ensemble of $\approx$ 40 ultracold ^{39}K atoms. The lattice spacing is $\sim 4\,\mu$m and the apparent size of each spot is $\sim 0.74\ \mu$m ($e^{-1/2}$ radius). Regions 1, 2, 3 and 4 are the background regions of interest to estimate the single shot detection sensitivity of 3.9 atoms as explained in section 4.1.2. **(b)** Histogram of estimated atom number distribution in the image region. **(c)** Histogram of estimated atom number distribution in the background regions 1, 2, 3, 4 where the variance is 3.91 atoms.

Single shot detection sensitivity has been inferred by analysing the background region of the images. We choose background regions 1, 2, 3 and 4 for analysis as shown in figure 4.3. Referring to figure 4.3 of 100 site square lattice of microscopic atomic cloud, we fit 2d Gaussian distribution function (equation 4.1) to each spot to estimate the atom number, width of the atomic cloud at each tweezer site and position of each tweezer in the image plane as explained in

subsection 4.1.1. We repeat the fits with fixed widths and centroid positions, but shifted by the system size to a background region of the cloud (see figure 4.3). The resulting fit amplitudes give an estimate of the fitting errors induced by background imaging noise. Thus we obtain 100 values of single shot noise corresponding 100 tweezer sites per background region. We repeat this analysis for 20 absorption images. Therefore, in the end we average over 8000 values of single shot noise estimation. By calculating the standard error over these realisations, we obtain the uncertainty in the averaged value of the single shot detection sensitivity which is inferred as 3.9 atoms. It means that we can measure the atom number with an uncertainty of ± 3.9 atoms.

4.1.3 Analysis of atom loading into a single tweezer trap

It was found that optimal loading of the tweezers is achieved by evaporatively cooling the atoms in the reservoir trap while superimposing the DMD light pattern (figure 4.4a). At the end of the evaporation ramp the reservoir trap can be switched off leaving the atoms confined by the tweezers alone. The overall cycle time including MOT loading, evaporative cooling, transfer to the tweezers and imaging is $< 4\,\mathrm{s}$. Figures 4.4b,c show the characterization of the loading process for a single tweezer with $A = 100$ pixels, corresponding to an optical power of $90\,\mu\mathrm{W}$.

There is little difference if the tweezer is switched on suddenly or ramped slowly, however we found it is beneficial to turn on the tweezers at least 200 ms before the end of the evaporation ramp (as shown for a single tweezer in figure 4.4b), indicating a significant enhancement of the loading through elastic collisions with the reservoir atoms [163]. During the evaporative ramp-down of reservoir trap depth (figure 4.4a), the particles with average higher energy get selectively removed from the trap and subsequent thermalization of the remaining particles happens through elastic collisions. As our reservoir trap (pancake-shaped dipole trap) has been prepared using far-off resonant laser light, inelastic processes such as light-assisted inelastic collisions are greatly suppressed which minimizes loss and heating of atoms. Figure 4.4c shows that the mean occupation number $\bar{N} = \langle N \rangle_i$ (with i denoting different experimental realizations) strongly depends on the final temperature of the reservoir, with the maximal $\bar{N} = 120(5)$ found for $T_{\mathrm{res}} \approx 2\,\mu\mathrm{K}$. The temperature of the atoms after loading measured using the time-of-flight method for a single tweezer

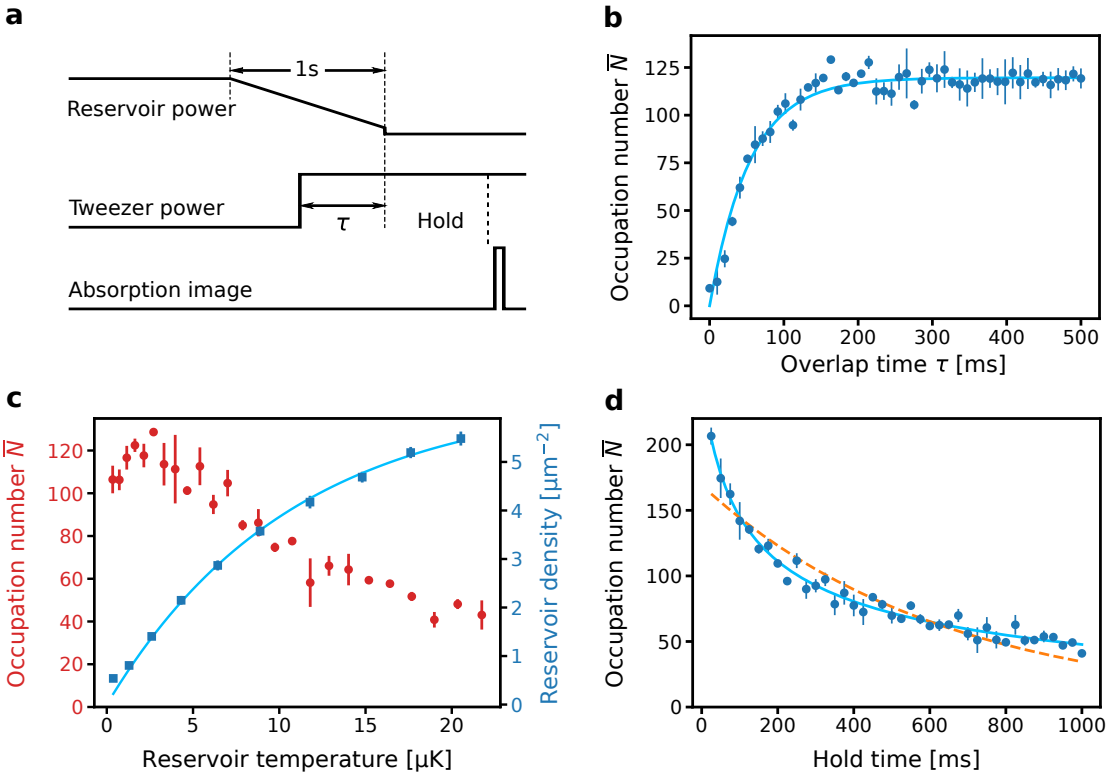

Fig. 4.4: Characterization of the loading process and lifetime of atoms in a single tweezer. (a) Sketch of the experimental sequence used to load the tweezers. (b) Mean occupation number in a single tweezer as a function of the overlap time τ between the end of the reservoir evaporation ramp and turning on the tweezer. For $\tau \approx 200\,\mathrm{ms}$ the occupation number reaches its maximum value of $\bar{N} = 120$. (c) Mean occupation and two-dimensional density of atoms in the reservoir as a function of the reservoir temperature after evaporation. Optimal loading is achieved for a final reservoir temperature of $2\,\mu$K, which is a compromise between temperature and the remaining density of atoms in the reservoir. (d) Measurement of the lifetime of atoms held in the tweezer. The solid line is a fit to a model accounting for one- and three-body loss processes, while the dashed line is an exponential fit assuming one-body loss only. In (b), (c) and (d) the error bars depict the standard deviation over three experimental repetitions.

is 17(1) μK. Figure 4.4d shows the lifetime of the atoms in the tweezer. An exponential fit describing pure one-body decay (dashed curve) is clearly ruled out by the data while a model which includes both three-body and one-body decay [164] provides an excellent fit (solid curve). The expression of the model is as follows:

$$\eta = \frac{\exp(-k_1 t)}{\sqrt{1 + (k_3/k_1)[1 - \exp(-2k_1 t)]}} \tag{4.7}$$

where k_3 is a three-body loss rate and k_1 is one-body loss rate. From this model we extract both the three-body and one-body decay constants $k_3^{-1} = 110\,\text{ms}$, $k_1^{-1} = 3100\,\text{ms}$, which are both orders of magnitude longer than typical timescales in Rydberg atom experiments.

4.2 Uniform loading across the tweezer array

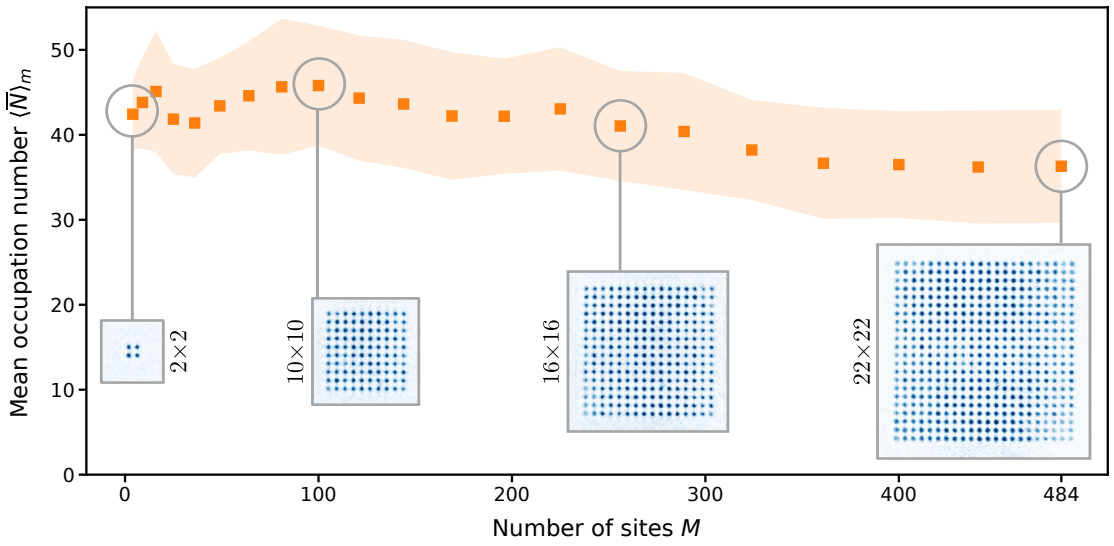

Fig. 4.5: Scaling up to hundreds of tweezers. The square data points show the array-averaged mean occupation number for square arrays with a period of 3.5 μm and different numbers of sites ranging from $M = 2 \times 2$ to $M = 22 \times 22$. Over this range the array averaged occupation number $\langle \bar{N} \rangle_m \approx 40$ is mostly homogeneous and insensitive to the number of tweezers. The shaded region represents the uniformity of each array, computed as the standard deviation of the mean occupation number. The insets show exemplary absorption images for 4 different sized arrays, each averaged over 20 experimental repetitions.

We now show that it is straightforward to scale up to a large number of sites while maintaining a uniformly high occupation of each tweezer. For arrays with more than approximately $M = (10 \times 10)$ sites we found it is beneficial to adapt the DMD pattern to compensate the Gaussian illumination profile. We adapt the number of pixels in each cluster according to its distance from the

center of the illumination region following an inverted Gaussian dependence as discussed in chapter 3 in subsection 3.4.5,

$$A_m = A_{\min} \exp\left(g r_m^2\right) \tag{4.8}$$

where m indexes a tweezer at position r_m in the DMD plane. The parameters $A_{\min} = 20$ pixels and $g = 2.3 \times 10^{-5}$ were manually adapted to obtain approximately equal optical depths for each tweezer, where $A_{\min} = 20$ corresponds to an optical power per tweezer of $18\,\mu$W. The maximum array size of $M = (22 \times 22)$ was fixed such that $\max(A_m) = 66$ pixels, due to larger spots increasing the apparent size of the atomic ensembles near the edge of the array. With an appropriate choice of parameters, the resulting approximately uniform trap depths across the array of tweezers can be expressed as the convolution of equation 4.8 and the Gaussian intensity distribution of the beam of the light that illuminates the DMD. Once the optimal compensation profile is found, it can be applied to different geometries without further adjustment.

Figure 4.5 shows the array averaged mean occupation number $\langle \bar{N} \rangle_m$ for square arrays with different numbers of sites. The solid orange symbols show the occupation number averaged over the entire lattice and over 20 experimental repetitions. The experiments show that $\langle \bar{N} \rangle_m \simeq 40$ is approximately constant for tweezer arrays with different numbers of sites $4 \leq M \leq 484$. As an example, for $M = 400$ the standard deviation calculated from the average of 20 images is $0.17\langle \bar{N} \rangle_m$, compared to $0.55\langle \bar{N} \rangle_m$ without any compensation as shown in Fig. 4.6. The uniformity could be further improved by adapting A_m for each tweezer individually, but it is already better than the expected intrinsic shot-to-shot fluctuations of the atom number in each site due to atom shot-noise for $\bar{N} > 36$. The apparent size of each atomic ensemble, found by analyzing the averaged absorption images, ranges from $0.64\,\mu$m near the center of the field to $0.93\,\mu$m at the edges ($e^{-1/2}$ radii of each absorption spot), limited by recoil blurring, the finite resolution of the imaging system including off axis blurring and the finite size of each DMD spot. By projecting the DMD light pattern onto a camera in an equivalent test setup we independently determine the beam waist of each tweezer to be $0.9\,\mu$m. Assuming each tweezer is described by a Gaussian beamlet and approximating the atomic cloud by a thermal gas with a temperature $\sim V_0/5$ (with trap depth V_0), we infer a cloud size of $\sigma_{r,z} = \{0.2, 1.0\}\,\mu$m. This is reasonably close to an independent estimate

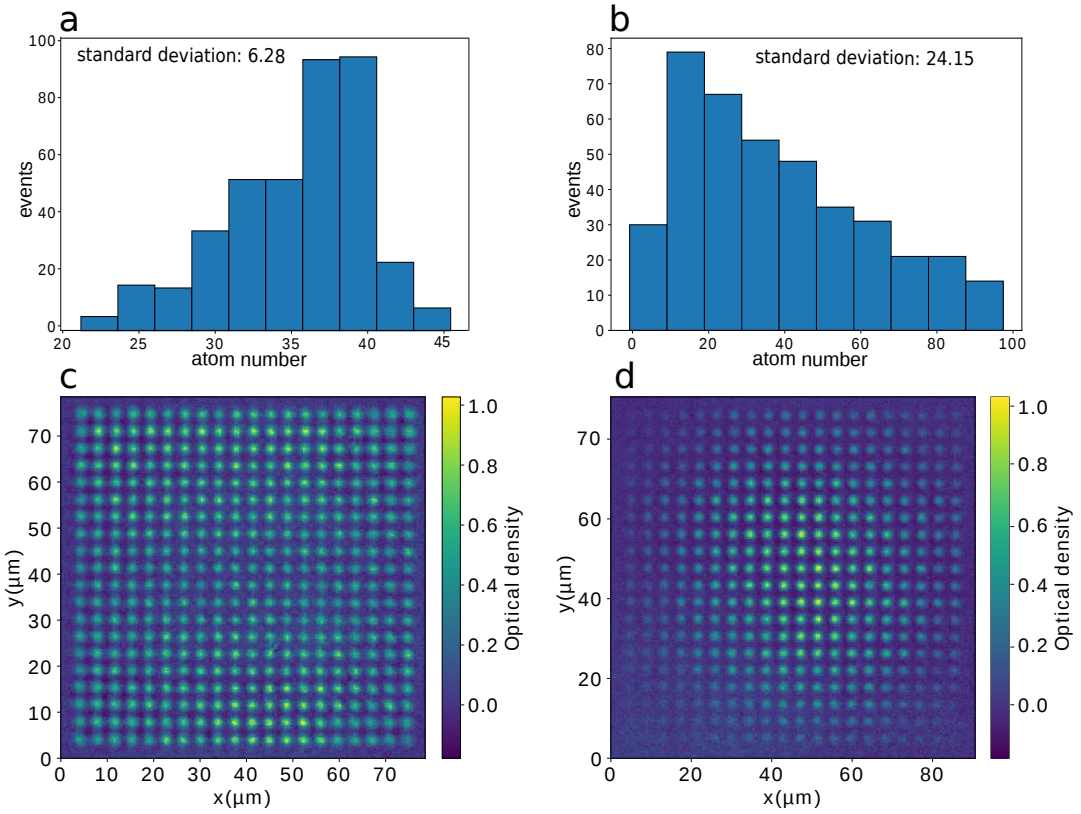

Fig. 4.6: Comparison of uniformity in atom loading into the array of tweezers produced using the DMD patterns with and without Gaussian gradient modification (a) and (b) are histograms of atom number extracted from the experimental absorption image shown in (c) and (d) respectively. (c) Experimental absorption image of a 400 site square lattice (averaged over 20 repetitions) produced using gradient (Gaussian) modified DMD pattern (see equation 4.8), where each spot corresponds to a microscopic ensemble of $\approx$ 30 ultracold ^{39}K atoms. The lattice spacing is 3 μm and the apparent size of each spot is $\sim$ 0.9 μm ($e^{-1/2}$ radius). (d) Experimental absorption image of a 400 site square lattice (averaged over 20 repetitions) produced without any gradient modification applied to DMD patterns. The lattice spacing is 4 μm The standard deviation calculated from the average of 20 images is $0.17\langle\bar{N}\rangle_m$ as shown in (a), compared to $0.55\langle\bar{N}\rangle_m$ without any gradient modification as shown in (b). Hence, gradient modification of the DMD patterns increses the uniformity of atom loading into the tweezers by $\approx$ 3 times.

$\sqrt[3]{\sigma_r^2\sigma_z} \approx 0.6\,\mu$m based on the experimentally measured three-body loss rate and a theoretical calculation of the zero field three-body loss coefficient for ^{39}K [165].

To understand this in more details, the theoretical calculation is given as follows. The three body decay rate can be described as

$$\frac{1}{N}\frac{dN}{dt} = -k_3\langle n^2\rangle \tag{4.9}$$

where K_3 is the constant of the three body recombination rate for a thermal gas (6 times higher than that for a Bose-Einstein condensate due to Bose statistics). $\langle n^2\rangle$ is the mean squared density of the atom cloud, $\langle n^2\rangle = \int n(r)^2 n(r) d^3r$ and N is the total number of atoms in the atomic cloud. The density of the Boltzmann distributed atomic cloud can be written as,

$$n(r) = \frac{\sqrt{2}N\exp\left(\frac{-r^2}{2\sigma_r^2}\right)}{4\pi^{\frac{3}{2}}\sigma_r^3} \tag{4.10}$$

where σ_r is an atomic cloud width, r is a radial distance from the center of the atomic cloud and N is the total number of atoms in the atomic cloud. The mean squared density is then obtained by integrating equation 4.10 as,

$$n^2 = \int_0^\infty 4\pi r^2 n^2 n d^3r = \frac{\sqrt{3}N^3}{72\pi^3\sigma_r^6} \tag{4.11}$$

Taking $N = 200$ atoms in a single tweezer trap and substituting equation 4.11 into equation 4.10 and using experimentally measured three-body loss rate which is 110ms as shown in figure 4.4d and using a calculated $k_3 = 9.2 \times 10^{-29}$for ^{39}K [165], we obtain geometric mean width of the atomic cloud as $\sigma_r \approx 0.63\mu m$. This is close to $\sqrt[3]{\sigma_r^2\sigma_z} = 0.44$ extracted from experimental absorption images.

4.3 Towards single Rydberg excitation within a microscopic atomic ensemble

The small spatial extent of each ensemble is encouraging for experiments which aim to prepare a single Rydberg excitation at each site (as illustrated in figure 4.7), as it is significantly smaller than the nearest neighbour distance

and the typical Rydberg blockade radius of $R_{bl} \sim 3 - 6\,\mu$m (depending on principal quantum number). Approximating the density distribution as quasi-one-dimensional since $\sigma_z = 1 \gg \sigma_r = 0.2$, we can estimate the fraction of blockaded atoms. Assuming a 2d Boltzmann density distribution function for

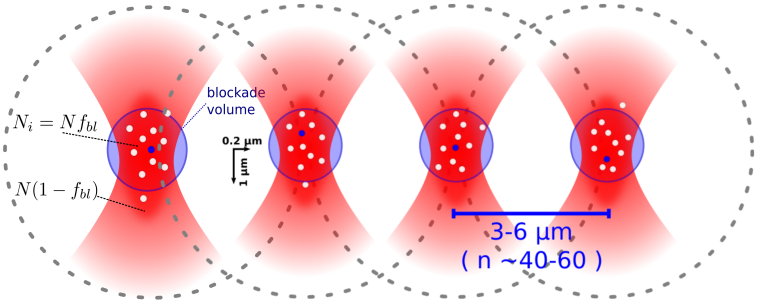

Fig. 4.7: Small spatial extent of microtraps The figure shows an array of 4 tweezer traps indicating the small spatial extent of tweezer trap of 1 μm in weak axis (z-axis) and 0.2 μm in tight axis. This small spatial extent of micro-trap lies well within the Rydberg blockade radius if the principle quantum number (n) = 40-60. The fraction of blockaded atoms are shown as Nf_{bl} and the fraction of unblockaded atoms are $N(1 - f_{bl})$ (equation 4.15).

the weak axis (z-axis),

$$n_z = n_0 \exp\left(-\frac{z^2}{2\sigma_z^2}\right) \tag{4.12}$$

where n_0 is the peak atomic density. To obtain total atom number in tweezer trap, the integration can be carried out over n_z.

$$\int_{-\infty}^{\infty} n_z dz = \sqrt{2}\sqrt{\pi} n_0 \sigma_z \tag{4.13}$$

The total number of atoms in the blockade region is given by

$$\int_{-\mathrm{R}_{bl}}^{\mathrm{R}_{bl}} n_z dz = \sqrt{2}\sqrt{\pi} n_0 \sigma_z \mathrm{erf}(R_{bl}/2\sigma_z) \tag{4.14}$$

where R_{bl} is the radius of Rydberg blockade. Therefore the fraction of blockaded atoms is

$$f_{bl} = \frac{\int_{-\mathrm{R}_{bl}}^{\mathrm{R}_{bl}} n_z dz}{\int_{-\infty}^{\infty} n_z dz} = \mathrm{erf}(R_{bl}/2\sigma_z) \tag{4.15}$$

where $\mathrm{erf}(x)$ is the Gauss-error function. For $R_{bl}/\sigma_z \geq 3$, $f_{bl} \geq 0.97$ which suggests that the blockade condition within a single tweezer should be well satisfied. To serve as effective two-level systems (comprised of the collective ground state and the state with a single Rydberg excitation shared amongst all

atoms in the ensemble), it is additionally important that the fluctuations of the atom number from shot-to-shot are relatively small otherwise the $\sqrt{N}$ collective coupling [157, 166, 167] will reduce the single atom excitation fidelity. Previous theoretical estimates have assumed Poisson distributed atom shot noise [143], which we generalize to the case of a stretched Poissonian distribution and imperfect blockade. However we neglect other possible imperfections such as spectral broadening due to laser linewidth or interactions between ground state and Rydberg atoms [143].

4.3.1 Infidelity of single Rydberg excitation within a single tweezer

To quantify how the fluctuations of the atom number in each microtrap influences the fidelity for preparing single Rydberg excitations, we follow the approach presented in [164]. We define a stretched Poisson distribution for atom number fluctuations as,

$$P_n = \frac{(\alpha\bar{N})^{n\alpha}}{(n\alpha)!}\exp^{-\alpha\bar{N}} \tag{4.16}$$

where α is a strectching factor. The mean of this stretched Poisson distribution is $\bar{N}$ and variance is $\frac{\bar{N}}{\alpha}$. We assume that within the blockade volume, the probability to excite a single atom undergoes collective Rabi oscillations

$$p_i = 1 - \cos^2(\sqrt{N_i}\Omega t/2) \tag{4.17}$$

where Ω is the single atom Rabi frequency [143]. In contrast the non-blockaded fraction of atoms $1 - f_{bl}$ undergoes Rabi oscillations at the frequency Ω. This can be obtained by solving optical Bloch equations for n-two level systems coupled by laser field of Rabi coupling Ω.

By expanding for $n - \bar{N}$ around the time for a collective π pulse: $t = \pi/(\sqrt{\bar{N}}\Omega)$, we obtain

$$p_i = 1 - \frac{\pi^2(n-\bar{N})^2}{16\bar{N}^2} \tag{4.18}$$

We can now define the average excitation probability as a weighted average

over a stretched Poisson statistical distribution for atom number fluctuations.

$$\langle p_i \rangle = \sum_n^{\infty} p_i P_n(\alpha, \bar{N}) = 1 - \frac{\pi^2}{16\alpha\bar{N}} \tag{4.19}$$

This can be understood as the fidelity for creating a single excitation when the number of atoms fluctuates with the mean of α and the variance $\bar{N}/\alpha$. The fidelity approaches 1 when the $\bar{N}$ is large, or the variance is small ($\alpha \to \infty$). Now we can define the infidelity as

$$\epsilon = 1 - \langle p_i \rangle \tag{4.20}$$

For Fano factor [164], $F = \alpha^{-1} = \frac{\mathrm{var}(n)}{\bar{N}}$, the infidelity for producing exactly one excitation (ϵ) will have an expression as,

$$\epsilon \approx \frac{\pi^2}{4}\frac{F}{4\bar{N}} + (1 - f_{bl}) \approx \frac{\pi^2}{16}\frac{\mathrm{var}(n)}{\bar{N}^2} + (1 - f_{bl}) \tag{4.21}$$

For $f_{bl} \to 1$, the infidelity is proportional to the relative variance $\mathrm{var}(N)/\bar{N}^2$.

4.3.2 Estimation of effects of fluctuations in atom number over the infidelity of single Rydberg excitation

To estimate the relative variance of the atom number fluctuations we prepare tweezer arrays with different numbers of sites and trap depths, corresponding to mean occupation numbers from $\bar{N} = 20$ to $\bar{N} = 200$. For each set of experimental conditions we take 20 absorption images from which we compute the mean occupation and the variance of the atom number in each tweezer. Fig. 4.8 shows the relative variance $\mathrm{var}(N)/\bar{N}^2$ calculated for 75880 tweezer realizations. We see that for smaller atom numbers the relative variance is consistent with the expected Poissonian atom shot noise for independent particles ($\mathrm{var}(N) = \bar{N}$, shown by the solid black line), while for $\bar{N} \gtrsim 50$ the fluctuations are sub-Poissonian, reaching the lower limit expected for three-body loss ($\mathrm{var}(N) = 0.6\bar{N}$, shown by the the dashed black line is a prediction assuming sub-Poissonian atom number fluctuations $\mathrm{var}(N)/\bar{N}^2 = 0.6/\bar{N}$) [164]. For $\bar{N} > 40$ the expected infidelity due to atom number fluctuations would be below 0.03, showing that this system should be compatible with high fidelity preparation of individual Rydberg excitations and quantum logic gates, and could still be further improved using adiabatic or composite pulse techniques [156].

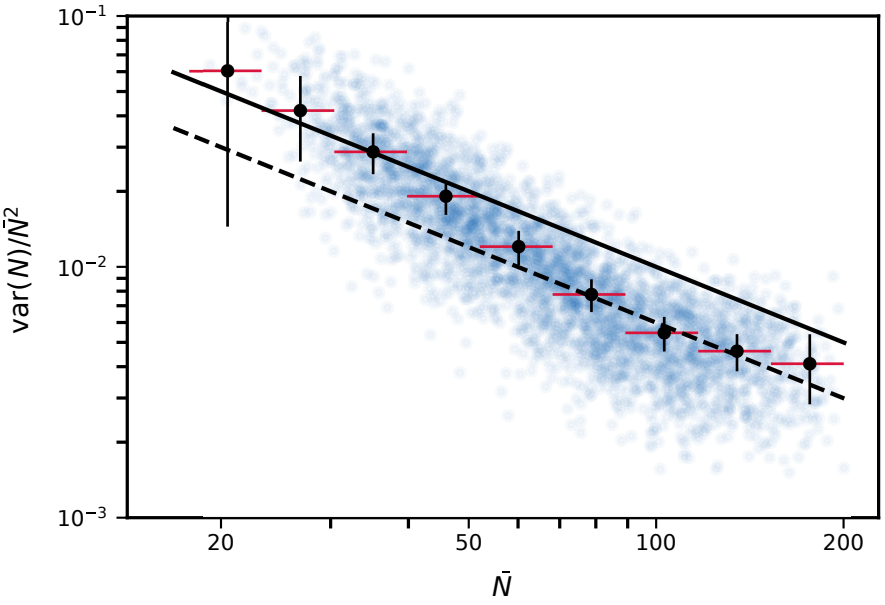

Fig. 4.8: Relative variance of the atom number in each tweezer $\mathrm{var}(N)/\bar{N}^2$ **as a function of the mean occupation number** $\bar{N}$**.** The blue points show the relative variance computed from 20 repetitions of the experiment and for different mean occupation numbers. The black symbols show the same data after binning, where the bin widths are indicated by the horizonal red bars. The vertical error-bars show the standard error computed over the values inside each bin multiplied by a scaling factor of 10 for better visibility. The solid black line is a prediction assuming Poissonian atom number fluctuations $\mathrm{var}(N)/\bar{N}^2 = 1/\bar{N}$ and the dashed black line is a prediction assuming sub-Poissonian atom number fluctuations $\mathrm{var}(N)/\bar{N}^2 = 0.6/\bar{N}$.

4.4 Summary

To summarize, this work demonstrates an approach for realizing hundreds of ultracold atomic ensembles in programmable two-dimensional arrays, where each tweezer has approximately uniform filling, small spatial extent and small fluctuations of the atom number from realization to realization. Compared to a stochastic loading of the tweezers via light assisted collisions from a MOT this has several advantages. First, it is possible to achieve very high occupation numbers $N \gg 1$ with relatively low power requirements per tweezer, since the temperature of the initial reservoir trap can be lower than the typical temperatures in a MOT and elastic, rather than inelastic, collisions lead to a high filling probability. This is beneficial for scaling up to hundreds or even thousands of tweezers as the large volume of the reservoir trap makes it possible to simultaneously fill many tweezers in parallel without the need for additional lasers and complex rearrangement protocols to fill empty sites.

Additionally, atomic ensembles present the possibility to evaporatively cool the atoms in each tweezer to reach high phase space densities or as a more controlled starting point for (quasi) deterministic single atom preparation schemes using controlled inelastic collisions [54, 57] or the Rydberg blockade effect [143, 168, 169]. The observation that the number of atoms inside each tweezer exhibits fluctuations below the Poissonian atom shot noise limit is especially promising for quantum information processing based on small Rydberg blockaded atomic ensembles benefiting from fast collectively enhanced light-matter couplings [44, 143, 158, 159, 168].

Chapter 5

Rydberg excitation of microscopic atomic ensembles

With the successful demonstration of large arrays of microscopic atomic ensembles prepared using digital micro-mirror device (as described in chapter 4), it is necessary to achieve the narrow-linewidth two-photon Rydberg excitation of these microscopic atomic ensembles. This is a required pre-requisite to achieve the aim to perform the coherent manipulation of Rydberg excitations among these atomic ensembles. For this purpose, chapter 5 focuses on the two-photon excitation of the Rydberg state $69S_{1/2}$ of ^{39}K from the arrays of microscopic atomic ensembles.

This chapter starts with an introduction of the two-photon energy level scheme for Rydberg excitation shown in figure 5.2. In the same section, I present the excitation laser set-up to address the two-photon transition described in figure 5.1 along with the detection scheme of Rydberg atoms via electric field ionization. In section 5.2, I present the experimental sequence for the spectroscopic measurements of the Rydberg excitation in the pancake-shaped optical dipole trap and subsequently I introduce the excitation-sequence in the array of microscopic atomic ensembles. In the same section, I present the spectral linewidth 1.39 MHz $\pm$ 0.08 MHz of the two-photon Rydberg excitation from the pancake-shaped optical dipole trap and 1.47 MHz $\pm$ 0.14 MHz from the array of microscopic atomic ensembles along with an investigation of the broadening mechanisms such as Doppler broadening, power broadening and inhomogeneity in the excitation laser that could possibly affect the spectral

line-width. In the same section, I present the recent results of the experiments of the geometry variation of these arrays of microscopic atomic ensembles on the Rydberg excitation spectrum in terms of the broadening of the spectral linewidth.

5.1 Two-photon excitation scheme

Figure 5.1 represents a schematic of the excitation laser-setup around the science chamber to address the two-photon excitation scheme as shown in figure 5.2 to perform Rydberg excitation experiment. It also consists of the detection scheme to detect the Rydberg atoms via electric field ionisation method.

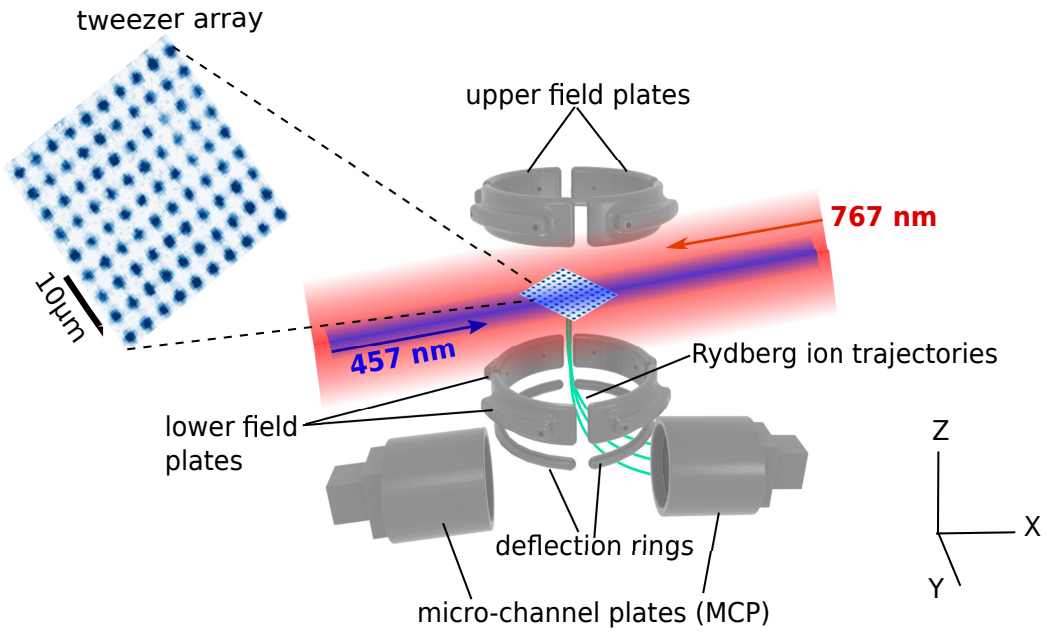

Fig. 5.1: Excitation laser setup to create Rydberg atoms: Schematic of counter-propagating two-photon excitation laser beams 767 nm (red arrow) + 457 nm (blue arrow) around the vacuum chamber to create Rydberg excitation in the microscopic atomic ensembles that are trapped within the large arrays of tweezer traps at the center of the vacuum chamber. The Rydberg detector assembly is composed of two sets of four electric field plates each, placed above and below the atomic cloud, that compensate the stray electric fields during Rydberg excitation and perform the ionization of the Rydberg states by the application of large voltages. The ions travel towards a micro-channel plate (MCP) detector by following the corresponding fields produced by the deflection rings (the trajectory of ions is shown using the green arrow). Figure modified from [134].

The 767 nm laser system

As explained in details in [117], the light used for the lower transition of the Rydberg excitation $4S_{1/2}$ F = 1 to $4P_{3/2}$ is obtained from a diode laser[1] that gives a maximum power output of $\approx$ 80 mW at a wavelength of 767 nm. A small part of the laser beam is derived using a beam sampler and is used for laser locking. A major part of the beam is used for cooling, trapping, imaging and excitation as described in chapter 3. After the diode laser, some light has been picked up and coupled into a fibre which then guides it to the experiment. The power output after the fiber is up to $\approx$ 0.3 mW at a beam waist of $\sim$ 900 μm which counter-propagates to the blue light as shown in figure 5.1. The beam then passes through an AOM, to have a fast switch, because the response of a mechanical shutter is not fast enough for precisely triggering the Rydberg excitation [170].

The 457 nm laser system

As explained in detail in [117], the light at 457 nm (blue light) to couple the atomic state $4P_{3/2}$ to the Rydberg state $69S_{1/2}$ is obtained by frequency doubling of the light at 913 nm obtained from a combined diode laser tapered amplifier system[2] , having a maximum power output of $\approx$ 1.7 W. The fundamental light at 913 nm is frequency doubled using second harmonic generation (SHG) through a non-linear crystal in a frequency-doubling unit[3]. The blue beam obtained from the SHG at 457 nm is then guided to the vacuum chamber via several mirrors and then focused down to $\sim$ 30 μm onto the atoms with the power of $\approx$ 400 mW. A shutter is placed to switch the 457 nm light off within 500 μs. An AOM would be useful for faster switching times $<$ 100 ns but it is also associated with a power loss due to its finite diffraction efficiency. The laser is situated next to the SHG and the laser beam is guided into the SHG with two folding mirrors.

Frequency stabilisation using reference cavity

For frequency stabilization, 767 nm and 913 nm lasers are locked to a stable reference cavity[4] through Pound-Drever-Hall stabilization scheme [171]. Fiber-

[1]Toptica DL pro
[2]Toptica TA pro
[3]Toptica SHG pro
[4]Stable Laser Systems ATF 6010-4

coupled electro-optical modulators (EOM)[5] have been used to generate the PDH modulation at 20 MHz. The EOMs generate sidebands of up to 600 MHz for blue excitation laser, to perform the spectroscopy of the Rydberg states. The reference cavity consists of two mirrors, which are separated by 100 mm of distance. They are stabilized passively by an ultra-low expansion (ULE) glass-spacer. The mirrors posses a special coating such that the transmission through them is low for the desired frequencies to stabilize to narrow linewidths. The resonator is placed inside an evacuated enclosing made of aluminium with temperature stabilization to decouple from the environment. More details on the ULE are given in [172]. The obtained linewidth of 767 nm is $\approx$ 20 kHz and the linewidth of 913 nm light is $\approx$ 30 kHz after frequency stabilisation with ULE cavity. For more detailed working of frequency stabilisation of 913 nm light using ULE cavity, please refer to the master's thesis of my colleague Henrik Hirzler [117].

5.2 Rydberg ion detection scheme

As explained in detail in [134], the detection scheme via electric field ionisation provides a direct access to the number of Rydberg atoms. The approach described here is based on electric field ionization with successive detection of the generated ions [173]. In another approach, the Rydberg atoms are pumped down to the ground state and detected using the fluorescence measurement [174].

Rydberg detector set-up

In reference to [134], figure 5.1 represents a schematic of our home-built Rydberg ion detection setup [175]. Because of the high sensitivity of Rydberg atoms to external electric fields, the setup consists of eight electrodes shown in figure 5.1 located around the atomic cloud to compensate stray electric fields. For cancellation of horizontal x-y components, the upper and lower four electrodes are interconnected to two pairs each, so that they are rotated by 90^o around z, and apply a cancellation voltage[6] to each of the two pairs. All four upper and lower electrodes are treated effectively as a pair of two opposing electrodes for compensation along the vertical axis. For more details on electric

[5] Qubig Q1603-UHD/1 (767 nm) and Jenoptik PM905 (913 nm)
[6] Omega OM-USB-3103, 8-channel, 16-bit analog voltage, output range ±10 V

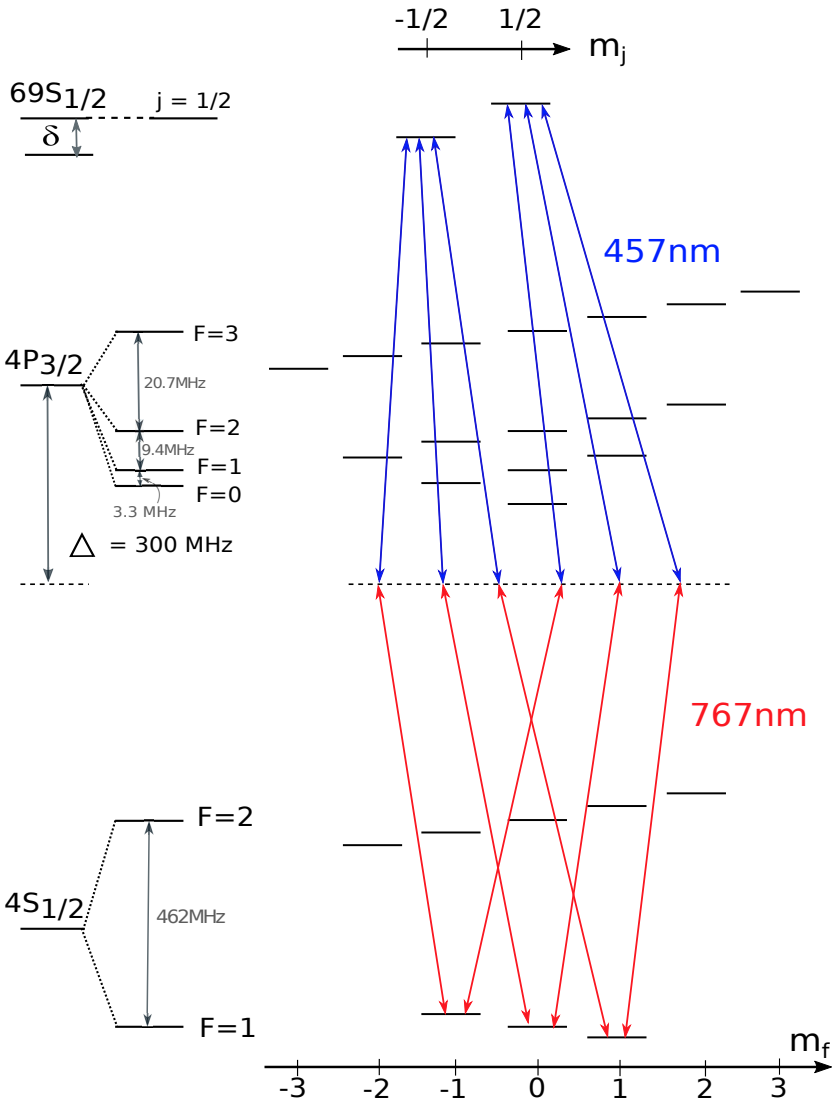

Fig. 5.2: Level schematic for two-photon Rydberg excitation: (Image reproduced from [117]) Level schematic for two-photon Rydberg excitation in a weak magnetic field. Atoms are prepared in the $F = 1$, $m_F = 0, \pm 1$ ground states and are then excited to the Rydberg state $69S_{1/2}$, $m_j = \pm 0.5$ via a two-photon transition, that is far detuned from the intermediate state by ≈ 300 MHz. A linear Zeeman shift is induced for the m_f and the m_j levels by a weak magnetic field, resulting in six transitions.

field nulling, please refer [117].

Electric field ionisation

Referring to [134], the compensation electrodes are rapidly switched to high voltages (up to $\pm$ 2.5 kV) with the help of fast switches[7] for electric field ionisation. The ions are then directed towards the micro-channel plate detector (MCP)[8], as visualised by the green flight trajectory in figure 5.1 following the applied voltage to one of the two deflection rings. After the Rydberg excitation pulse (as shown in the figure 5.3), the electric field plates are switched from the values of small compensation voltages to the values of large voltages for ionization and then also turn on the deflection voltage of one of the deflection rings. At the end of a time of flight of the ions of 3 μs , the generated ions hit the MCP creating voltage spikes, that get recorded on a fast oscilloscope[9]. This allows to extract the instantaneous number of Rydberg excitation at the end of the excitation pulse. We extract the time traces of ion events on the MCP from the fast oscilloscope. These traces are integrated over the mean arrival time of the ions. This integrated ion signal of MCP is related to the corresponding number of Rydberg excitations in the atomic cloud through a calibration factor. This calibration factor is determined by calculating the atom number from the corresponding absorption images by considering that once an atom is excited to the Rydberg state $69S_{1/2}$, it decays with the radiative lifetime of $\sim$ 190 μs out of trap i.e. all excitations are lost from the atom cloud. This implies that the loss in atom number from the traps is directly proportional to the cumulative ion signal of MCP via this calibration factor.

5.3 Rydberg excitation spectroscopy of $69S_{1/2}$ state in ^{39}K

We have performed two-photon spectroscopy of the Rydberg state $69S_{1/2}$ from microscopic atomic ensembles trapped in large arrays of tweezer traps as well as of the atoms from pancake shaped optical dipole trap to compare the linewidth between both. Following section describes the experimental sequence of the two photon spectroscopy of the atoms from pancake trap and reports on

[7] Behlke HV switches
[8] Hamamatsu F1551-21S
[9] TeledyneLeCroy WaveRunner 8254M-MS with up to 4 GHz bandwidth and 40 GS/s sampling rate

the achievement of the narrow spectral linewidth.

5.3.1 Rydberg excitation from pancake-shaped optical dipole trap

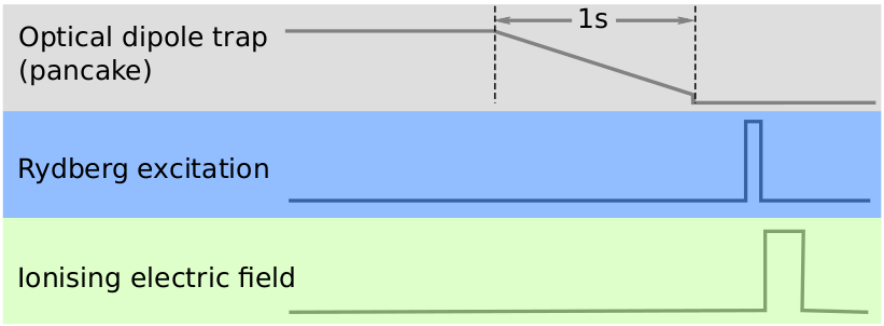

Fig. 5.3: Sequence of spectroscopic measurements from atoms trapped inside pancake-shaped optical dipole trap: The atoms are cooled down using evaporative cooling of the dipole trap. In these experiments, we use the 767 nm light plus the blue light to perform the Rydberg excitation. The excitation pulse length is 100 μs. The pancake trap stays on during the excitation to trap the atoms. The final Rydberg atom number is detected via electric field ionisation. The sequence is repeated for different detunings δ of the blue light around the Rydberg transition $69S_{1/2}$. This approach is similar to the one in [117].

In figure 5.3, the experimental sequence for taking a Rydberg excitation spectrum is shown. The approach followed here is similar to that given in [117]. We start in the pancake-shaped optical dipole trap with $\sim 10^5$ atoms. To begin with, the power of the pancake trap is set to $\sim$ 2.7 W. Then the power of the pancake-shaped dipole trap is slowly ramped down during the evaporative cooling. Viewing simplistically, the high energy atoms escape the trap potential which is lowered and the rest of the atoms get rethermalized to a lower temperature. This step is continuously repeated for a ramp cycle time of 1s. This stage of cooling is necessary to decrease the Doppler broadening. In the next step of Rydberg excitation, the atomic cloud is exposed to the two excitation beams (red + blue) for 100 μs. The red excitation beam is far-detuned corresponding to the intermediate state $4P_{3/2}$. The blue beam is near-resonant corresponding to the Rydberg state $69S_{1/2}$ having a small detuning of δ. The pancake trap stays on during the excitation time. Additionally a weak magnetic field is applied to observe the Zeeman splitting of the energy states as shown in figure 5.2. The details of step by step preparation of Zeeman sub-levels is described in [117]. An atom loss ocuurs due to Rydberg excitations decreasing the optical density inside the pancake trap. The sequence is repeated for different detunings of

blue light δ for the spectroscopic measurements.

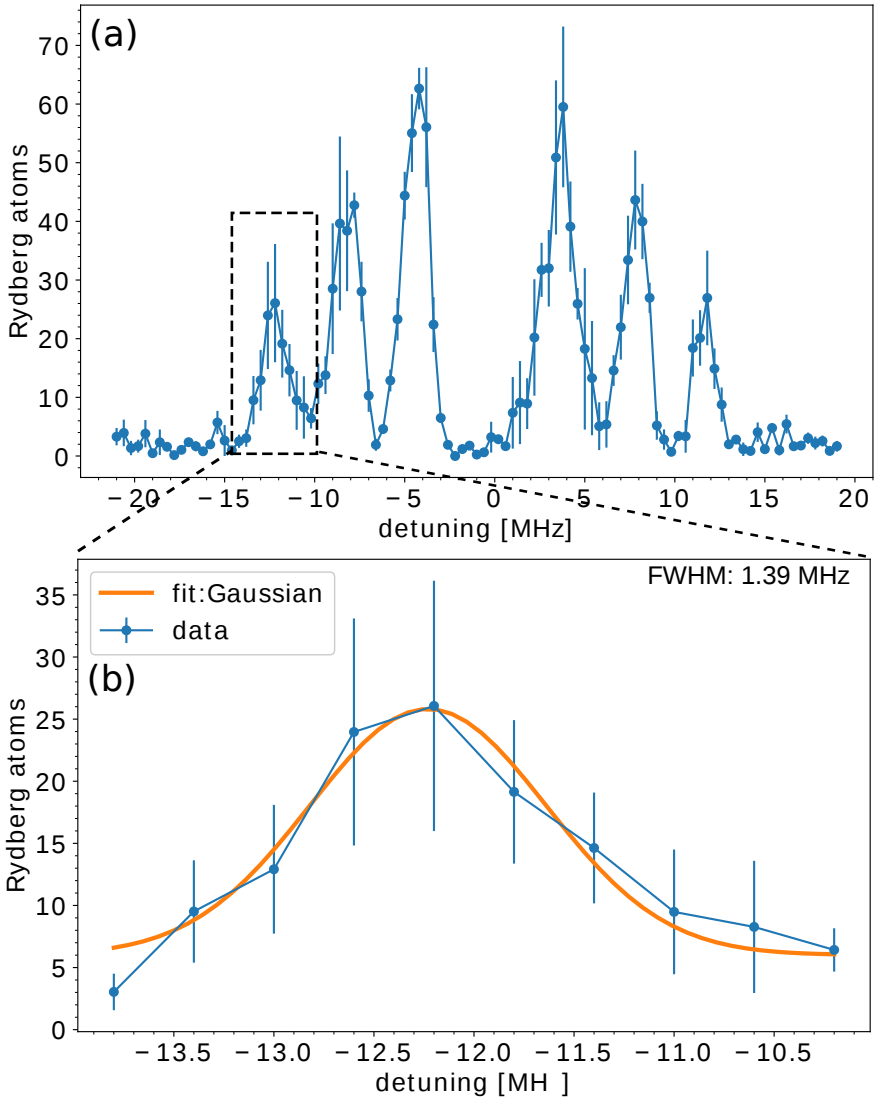

Fig. 5.4: Spectroscopic measurements of Rydberg excitation from atoms confined in pancake trap: (**a**) Two-photon Rydberg excitation spectrum of atoms from pancake trap obtained by scanning the detuning (x-axis) of the blue light (457 nm) across the Rydberg state $69S_{1/2}$. The spectrum contains six peaks that represent the Zeeman splitting of the corresponding energy transition of $4S_{1/2}$ to $69S_{1/2}$ via the intermediate state $4P_{3/2}$ as described in figure 5.2. (**b**) The zoom-in of the last peak from the spectrum to determine the spectral width of the transition. A full width half maximum (FWHM) of the Gaussian fit to this peak estimates the spectral width of the corresponding transition which is 1.39 MHz $\pm$ 0.08 MHz. These measurements are averaged over 5 repetitions and the error bars represent the standard error of the mean.

Figure 5.4 (a) describes the Rydberg excitation spectrum obtained from the atoms from pancake trap by scanning the detuning (x-axis) of the blue light (457 nm) across the Rydberg state $69S_{1/2}$. The spectrum contains six peaks

that represent the Zeeman splitting of the corresponding energy transition of $4S_{1/2}$ F = 1 to $69S_{1/2}$ via the intermediate state $4P_{3/2}$ as visualised in figure 5.2. The spectral resonances are distinguished into two sets with each containing three resonances. The set with the resonances with larger positive detuning are identified as the transitions to $m_j = +1/2$ of the Rydberg state $69S_{1/2}$ as it is shifted to the higher energies than the Rydberg state with m_j = -1/2. The ground state $m_f = +1$ is energetically shifted down. Hence, the transition from the ground states $m_f = +1$, $m_f = 0$, m_f = -1 to a desired m_j of the Rydberg state are identified from left to right in the spectrum. As shown in figure 5.4 (b), a full width half maximum (FWHM) of the Gaussian fit to one of the 6 peaks of the spectrum estimates the spectral width of the corresponding transition 1.39 MHz $\pm$ 0.08 MHz. The preliminary qualitative understanding of the factors that could possibly affect the linewidth of the spectrum is discussed in section 5.2.3.

5.3.2 Rydberg excitation from array of microscopic atomic ensembles

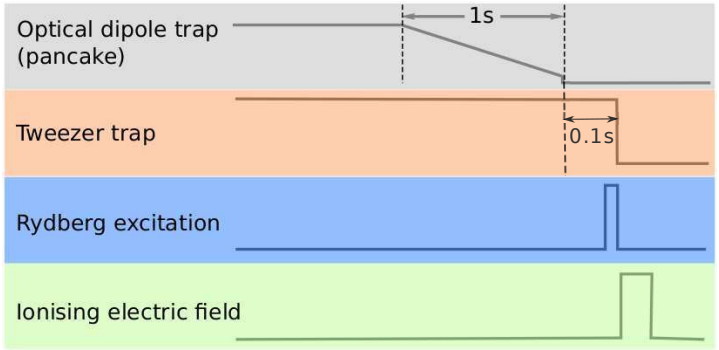

Fig. 5.5: Sequence of spectroscopic measurements from atoms trapped within the array of tweezer traps: The pancake trap power is ramped down during the atom-loading from pancake trap to the array of tweezer traps. The pancake trap is switched off for 100 ms before the Rydberg excitation pulse to avoid any excitation signal coming from background atoms from pancake trap. The tweezer trap stays on during Rydberg excitation pulse. We use the 767 nm light in addition with the blue light (457 nm) for Rydberg excitation. The excitation pulse length is 100 μs. The final Rydberg atom number is detected via electric field ionisation. The sequence is repeated for different detunings δ of the blue light from the Rydberg transition $69S_{1/2}$.

Figure 5.5 visualizes the experimental sequence for taking a Rydberg excitation spectrum from tweezer traps. To efficiently load the atoms from pancake trap into the tweezer traps, the pancake trap power is ramped down in the sequence

of evaporative cooling. This stage allows to re-thermalize the atoms within the tweezer traps at colder temperatures of 17 μk by exploiting elastic collisions. The detailed atom-loading process into the array of micro-traps is described in chapter 4. The pancake trap is switched off for 100 ms before the Rydberg excitation pulse to avoid any excitation signal coming from background atoms from pancake trap. The tweezer trap stays on during Rydberg excitation pulse for better confinement of the atoms. For the next step of Rydberg excitation, the array of tweezer traps are exposed to the two excitation beams (red+blue) for 100 μs. The red excitation beam is far-detuned corresponding to the intermediate state $4P_{3/2}$. The blue beam is near-resonant corresponding to the Rydberg state $69S_{1/2}$ with a small detuning of δ. Additionally, a weak magnetic field is applied to observe the Zeeman splitting of the energy states as shown in figure 5.2. The sequence is repeated for different detunings δ of blue light for a single spectroscopic measurement.

Figure 5.6 (a) describes the Rydberg excitation spectrum obtained from the array of tweezer traps by scanning the detuning (x-axis) of the blue light (457 nm) across the Rydberg state $69S_{1/2}$. As described in the previous section, the spectrum contains six peaks that represent the Zeeman splitting of the corresponding energy transition of $4S_{1/2}$ F = 1 to $69S_{1/2}$ via the intermediate state $4P_{3/2}$ as visualised in figure 5.2. As shown in figure 5.6 (b), a full width half maximum (FWHM) of the Gaussian fit to one of the 6 peaks of the spectrum estimates the spectral width of the corresponding transition which is 1.47 MHz $\pm$ 0.14 MHz. The spectral width of the Rydberg excitation of the atoms from tweezer traps is found to be comparable to that from pancake trapped atoms from figure 5.4. A discussion based on a qualitative preliminary understanding of the factors that could possibly contribute to such effects is presented in the next section.

5.4 Estimation of the factors responsible for the spectral broadening

Doppler broadening

In the rest frame of the moving atoms, the laser appears to have a slightly modified frequency. When averaging over the velocity distribution of atoms,

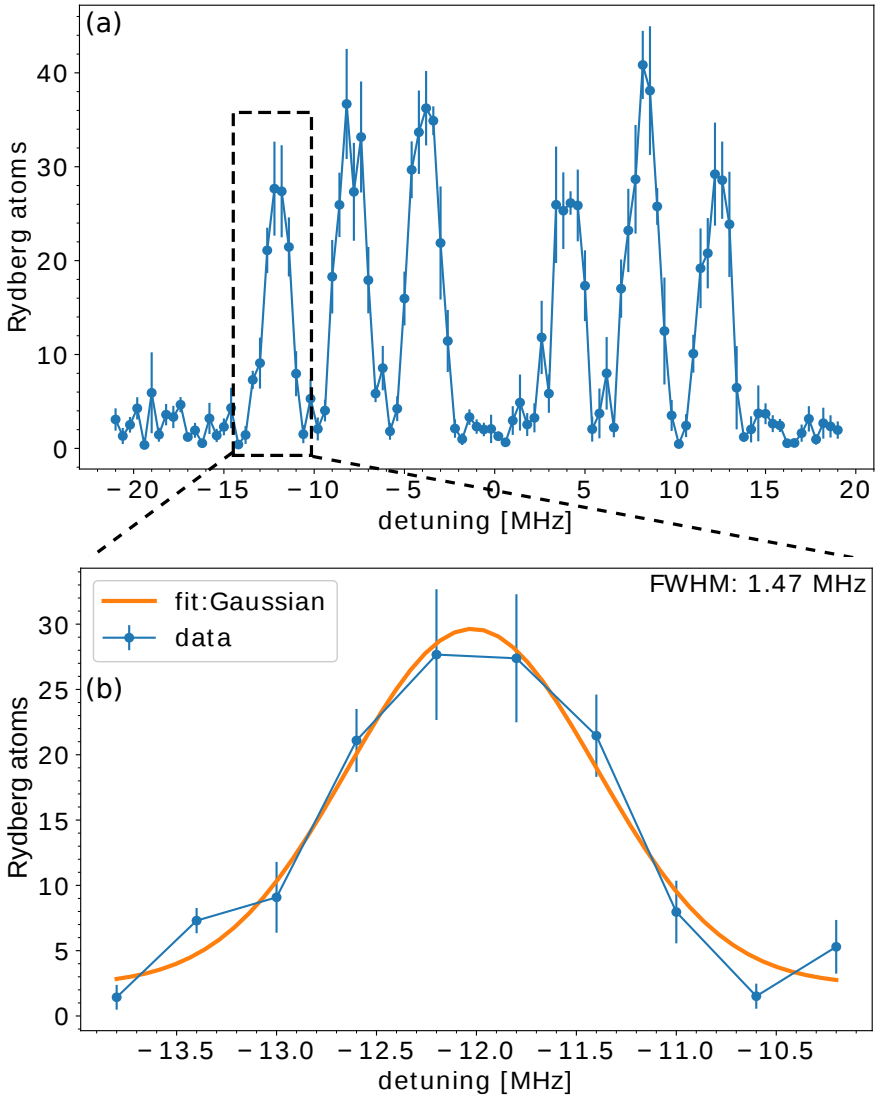

Fig. 5.6: Spectroscopic measurements of Rydberg excitation from atoms confined in tweezer traps: (**a**) Two-photon Rydberg excitation spectrum of atoms from array of tweezer traps obtained by scanning the detuning (x-axis) of the blue light (457 nm) across the Rydberg state $69S_{1/2}$. The spectrum contains six peaks that represent the Zeeman splitting of the corresponding energy transition of $4S_{1/2}$ to $69S_{1/2}$ via the intermediate state $4P_{3/2}$ as described in figure 5.2. (**b**) The zoom-in of one of the peaks from the spectrum to determine the spectral width of the transition. A full width half maximum (FWHM) of the Gaussian fit to this peak estimates the spectral width of the corresponding transition which is 1.47 MHz $\pm$ 0.14 MHz. These measurements are averaged over 5 repetitions and the error bars represent the standard error of the mean.

we obtain the temperature dependence of the spectral broadening which can be expressed as [117]:

$$\frac{\delta\omega}{2\pi} = \sqrt{8k_B T \ln 2/m}\sqrt{\lambda_1^{-2} + \lambda_2^{-2} + 2(\lambda_1\lambda_2)^{-1}\cos\theta} \tag{5.1}$$

where T is the temperature of atoms, k_B is the Boltzmann's constant, $\delta\omega$ is the spectral width, $m = 39u$ for ^{39}K with λ_1 = 767 nm and λ_2 = 457 nm for different beam alignments θ. The $\theta = \pi$ for counter-propagating alignment of excitation beams. The typical temperature of atoms in the tweezer traps is 17 μk and the expected spectral broadening at this temperature turns out to be 122 kHz following the scaling with $T^{1/2}$ (equation 5.1). Hence, to achieve the narrower spectral width of $\sim$ 80 kHz which is approximately equal to the excitation laser's (457 nm + 767 nm) linewidth, the temperature of atoms in the tweezer trap needs to be reduced to $\sim$ 2 μk.

Power broadening

The effective two-photon power broadening $d\Gamma$ can be expressed as [176],

$$d\Gamma = \Gamma\sqrt{1 + 2\frac{\Omega_{eff}^2}{\Gamma^2}} \tag{5.2}$$

where Γ is a natural linewidth of Rydberg state which in our case is $\approx$ 10 kHz [177]. The Ω_{eff} is an effective two photon Rabi coupling and is $\approx 2\pi \times 0.63$ MHz and can be calculated as $\frac{\Omega_r\Omega_b}{2\Delta}$ [117] where Ω_b is the Rabi coupling of blue beam i.e. $\approx 2\pi \times 30$ MHz and Ω_r is the Rabi coupling of red beam i.e. $\approx 2\pi \times 13$ MHz. The Δ is the detuning of the excitation beams with the intermediate state (see figure 5.2 and it is 300 MHz. With these parameters, an estimated spectral broadening of two-photon Rydberg excitation is $<$ 1 MHz.

Inhomogeneity in the intensity of the Rydberg excitation lasers

Assuming the Gaussian distribution of the intensity of the blue beam, I simulate a three-level system based on a simple single atom picture. This simulation consists of three level system (figure 5.2) optical Bloch equations (OBEs) obtained from master equation for density matrix ρ that includes Lindblad operator (as given in the chapter 2 section 2.2.1). This operator includes terms corresponding to the spontaneous decay of the intermediate state with rate Γ_e that is set at $2\pi \times 6$ MHz and to the dephasing of the Rydberg state with the rate γ_{deph}

that is set at 60 kHz which is the linewidth of the blue laser. I also include the γ_{deph} for the red laser which is set at $20kHz$ which is the laser linewidth and the spontaneous decay of the Rydberg state with rate Γ_r that is set at $2\pi \times 10$ kHz. The population in the Rydberg state is represented by ρ_{rr} and I calculate the steady state solution of these OBEs by varying the Δ_b for different values of Ω_b keeping Ω_r at 25 MHz similar to what we have in the experiment. Figure 5.7 represents the excited state population calculated using the quantum

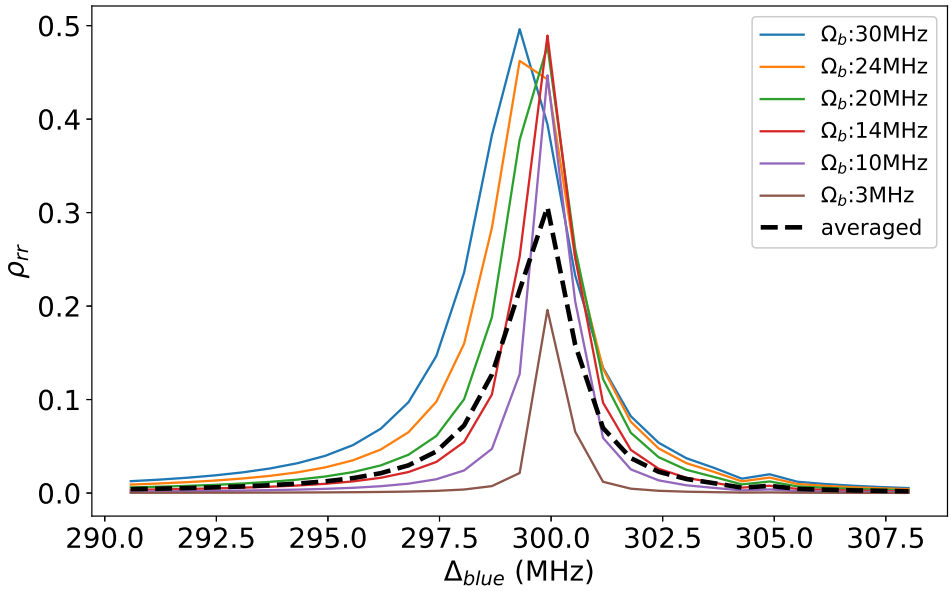

Fig. 5.7: Simulation of three-level Optical Bloch Equations for different Rabi frequencies of the upper transition: This figure represents the excited state population calculated using the quantum master equation from chapter 2 section 2.2.1 at steady state. Using the detuning of the lower transition (-300 MHz), two-photon resonance is achieved for an upper state detuning δ = 300 MHz. The different curves correspond to the different Rabi frequencies for the upper transition (Ω_b), from 30 MHz to 3 MHz. The position of the peak shifts due to the AC stark shift of the upper transition $\Omega_b^2/2\Delta$ [107]. Each spectral line has a width of $\approx$ 2 MHz. The little bump on the right is an artifact of the numerical calculation.

master equation from chapter 2 section 2.2.1 at steady state. Using the detuning of the lower transition (-300 MHz), two-photon resonance is achieved for an upper detuning δ = 300 MHz. The different curves correspond to different Rabi frequencies for the upper transition (Ω_b, from 30 MHz to 3 MHz). The position of the peak shifts due to the AC stark shift of the upper transition $\Omega_b^2/2\Delta$ [107]. Each spectral line has a width of $\approx$ 2 MHz. The little bump on the right is an artifact of the numerical calculation. Now, if we use a Gaussian

laser beam, then one can crudely average over all of these lines which would give a linewidth $\approx$ 2 MHz as shown in the figure 5.7 by the black dashed line (depending on the peak value of Ω_b). Hence probably we could also be limited by the inhomogeneous intensity in the excitation laser (457 nm) in achieving the spectral width narrower than 1.47 MHz.

Effects of power broadening can also be seen from figure 5.7. We observe that the width of each spectrum in that figure is increasing from left to right with the increase in the Rabi coupling Ω_b. This is due to the increase in the intensity of the coupling light (457 nm) as Rabi coupling is directly proportional to the intensity of the light [176]. Hence, we could also possibly be limited by the power broadening effects of the coupling laser (457 nm) that couples the intermediate state with the Rydberg state.

Assuming $\Delta \gg \Omega$, the AC-stark shift can be expressed as [107],

$$\Delta E = \frac{\Omega^2}{2\Delta} \tag{5.3}$$

Here, Δ is 300 MHz as mentioned in the previous subsection. The spectral broadening due to AC-stark shift caused by the red beam is estimated as $\approx$ 280 kHz using $\Omega_r = 2\pi \times 13$ MHz and by the blue beam is estimated as $<$ 1.5 MHz using $\Omega_b = 2\pi \times 30$ MHz.

5.4.1 Broadening due to the Rydberg interactions between the tweezer traps

The effects of modification of geometry are also observed on the spectral-width of the two-photon Rydberg excitation as shown in figure 5.8. Figure 5.8a and figure 5.8c represent the lattices with periods 3.5 μm and 5.5 μm respectively. Plots in the figure 5.8b and figure 5.8d represent the spectroscopic measurements of two photon Rydberg excitation of atoms in the tweezer arrays. The spectrum in figure 5.8d clearly shows the six peaks that represent the Zeeman splitting of the corresponding energy transition of $4S_{1/2}$ to $69S_{1/2}$ via the intermediate state $4P_{3/2}$ as described in figure 5.2. But spectrum in figure 5.8b shows that the 6 peaks are merged together making the spectrum broader when the lattice period is reduced to 3.5 μm when the atomic ensembles start overlapping with each other. Plots in figure 5.8e shows the variation in the

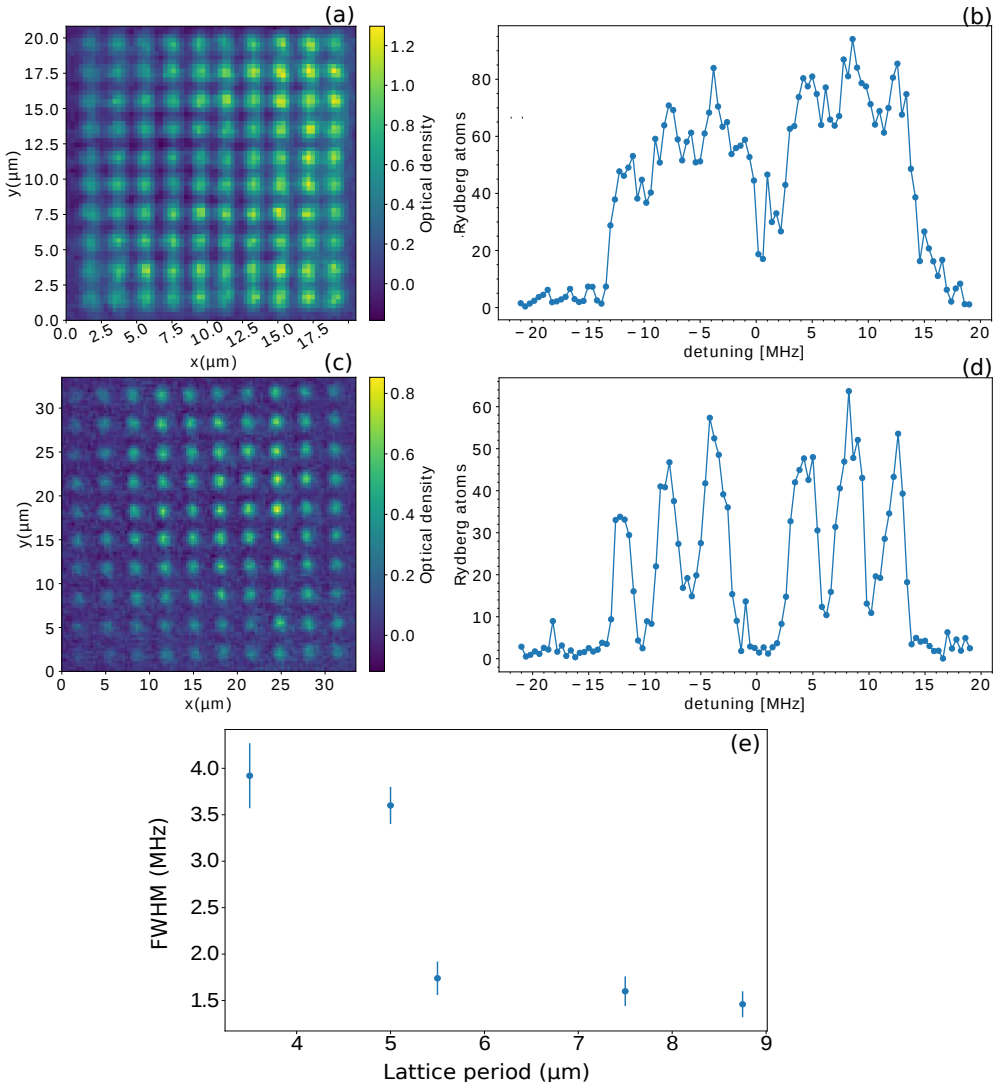

Fig. 5.8: Effects of variation of lattice period on spectral width. (**a**) and (**d**) are experimental absorption images of 100 site square lattice (averaged over 10 repetitions) produced using a DMD pattern. Here each spot corresponds to a microscopic ensemble of ≈ 30 ultracold ^{39}K atoms. The lattice spacing is 3.5 μm in (**a**) and 5.5 μm in (**c**) and the apparent size of each spot is ≈ 1.5 μm and ≈ 1 μm respectively. Plots (**b**) and (**d**) show the two-photon Rydberg excitation spectra of atoms in the array of tweezer traps from (**a**) and (**d**) respectively. These spectra are obtained by scanning the detuning (x-axis) of the blue light (457 nm) across the Rydberg state $69S_{1/2}$. The spectrum in (**d**) clearly shows the six peaks that represent the Zeeman splitting of the corresponding energy transition of $4S_{1/2}$ to $69S_{1/2}$ via the intermediate state $4P_{3/2}$ as described in figure 5.2. But spectrum in (**b**) shows that the 6 peaks are merged together making the spectrum broader. A variation in full width half maximum (FWHM) of the Gaussian fit to these peaks for different lattice period is shown in **(e)** and we see that the spectral width of ≈ 3.92 MHz for spectrum in (**b**) and ≈ 1.74 MHz for the spectrum in (**d**). It exhibits a clear spectral broadening due to decrease in lattice period. These measurements are averaged over 5 repetitions and the error bars represent the standard error over these experimental repetitions.

full width half maximum (FWHM) of the Gaussian fit to the spectra as the period of the array of tweezer traps vary. We see that the spectral width of the spectrum in figure 5.8b is $\approx$ 3.92 MHz and for spectrum in figure 5.8d is $\approx$ 1.74 MHz. This exhibits a clear spectral broadening due to decrease in lattice period. This could possibly indicate the presence of an interaction between the atomic ensembles and is comparable to the Van der Waals interaction strength (see chapter 2 section 2.2.2) of $\approx$ 4 MHz between the next to next nearest atomic ensembles separated by 7 μm shown in figure 5.8a. Due to the large blockadeof $\approx$ 10 μm as calculated in [134] for principle quantum number 69, we do not see any effects of nearest neighbour interaction as the 2 adjacent neighbours could be in the same blockade.

We have also observed that the density of atoms in the tweezer traps increase as the lattice period reduces as shown in the figure 5.9a. This also results in the increase in the spectral width of the two-photon Rydberg excitation spectra as shown in the figure 5.9b where the full width half maximum of the Gaussian fit to each of the spectra is observed to be increasing with the increase in the atomic density in the tweezer traps. This could also possibly contribute to the spectral broadening observed in the figure 5.8b. This could possibly be due to an increase in the Rydberg-Rydberg interaction for small lattice separations [178, 179].

5.5 Summary

To summarise, this chapter focuses on achieving narrow-linewidth two-photon Rydberg excitation spectrum of the microscopic atomic ensembles of ^{39}K trapped in large arrays of optical tweezer traps. We identify and discuss qualitatively (section 5.3) the possible mechanisms that could broaden and limit the spectral width of the transition such as Doppler broadening, power broadening, dephasing introduced by laser linewidth, inhomegeneity in the intensity of the excitation laser due to its Gaussian profile and an indication of interaction effects between the atomic ensembles from the tweezer traps via the measurements spectral broadening due to the geometry variation (figure 5.8) as summarised in the table 5.1.The improvements such as the use of a flat-top excitation beam with uniform intensity at its cross section could be useful in achieving uniform Rabi coupling experienced by the atoms within the cross section of the beam. Furthermore, the temperature of atomic ensembles should

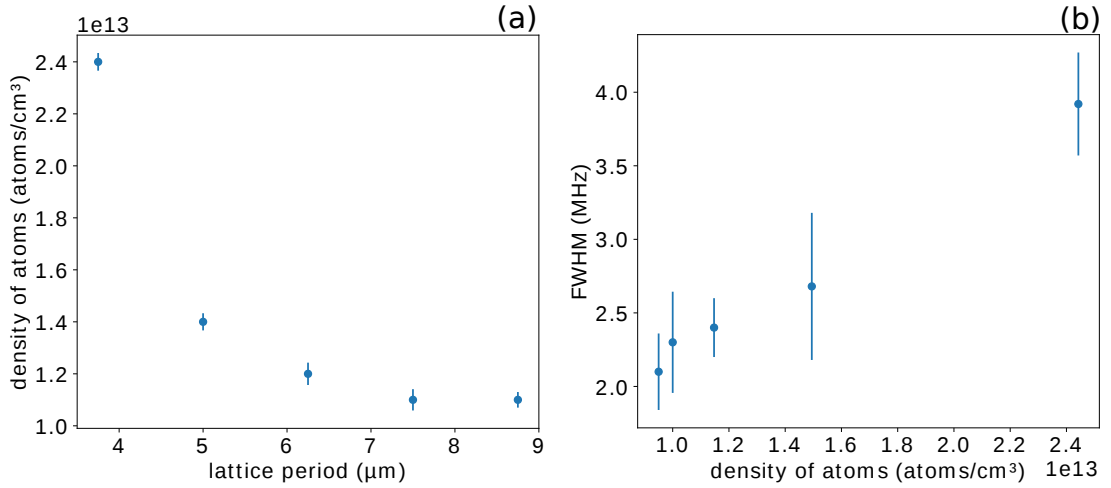

Fig. 5.9: Density effects on spectral broadening. (a) The atomic density in the tweezer traps increase with decrease in the lattice period where the adjacent atomic clouds start overlapping with each other. The error bars are the standard errors calculated by taking the average of atomic densities for an array of 100 site square tweezer traps as shown in the figure 5.8. **(b)** A full width half maximum is caulculated from the Gaussian fit to the spectra of the tweezer traps of period 3.5 μm by varying atomic densities as shown in (a). We can clearly observe the increase in the spectral broadening due to increase in atomic density as the lattice period reduces.

be reduced to 2 μk to achieve linewidth of $\sim$ 80 kHz that is approximately equal to the excitation laser linewidth to avoid thermal effects. To generalise,

Mechanism	Estimate
Doppler broadening	122 kHz
Power broadening	$<$ 1 MHz
Linewidth of the excitation laser	80 kHz
Inhomogeneous intensity of the Rydberg excitation lasers	$\approx$ 2 MHz

Tab. 5.1: Summarising the spectral broadening mechanisms This table shows an estimation of various mechanisms responsible for the spectral broadening of the two-photon Rydberg excitation of atomic ensembles from tweezer trap.

an experiment involving two-photon excitation of large tweezer traps of microscopic atomic ensembles, it is beneficial to expose atoms with homogeneous intensity of the two-photon excitation lasers, the beam alignment of the two excitation beams should be counter-propagating to avoid Doppler broadening and laser linewidth should be in the range of few tens of kHz, to achieve narrow linewidth of the transition.

Chapter 6

Conclusion and outlook

6.1 Summary:

Ultracold atoms confined in micro-trap arrays is a highly versatile platform for quantum many-body physics, quantum simulation and quantum computation because of the easy scalability, long coherence time, single site addressability and controllable interactions, e.g. using Rydberg states [32, 35–38]. With this motivation, during the course of this thesis, we have built an upgrade to our experimental setup based on ultracold potassium-39 atoms to generate the large arrays of microscopic atomic ensembles using digital micro-mirror device (DMD) (chapter 3). The integration of DMD in high resolution imaging system that is incorporated in our ultra-cold atomic experimental platform is presented along with the brief overview of the vacuum apparatus, laser cooling and trapping techniques. With the DMD technology, we are able to create hundreds of programmable arrays of optical tweezer traps. The resolution that we achieve is ~ 1 μm that corresponds to approximately 4 pixels on the DMD chip. To maintain the uniformity of trap depths across the large arrays of micro-traps, DMD patterns are adapted following an invertible Gaussian expression to compensate the Gaussian profile of the micro-trap beam. The estimated trap depth is ≈ 1 mK, trap frequency is $\approx$100 kHz.

Using this upgraded experimental setup, we have successfully demonstrated the experimental platform with more than 400 microscopic atomic ensembles trapped within optical tweezer arrays (chapter 4). We have presented an approach for realizing hundreds of ultracold atomic ensembles in programmable

two-dimensional arrays, where each tweezer has approximately uniform filling, small spatial extent and small fluctuations of the atom number from realization to realization. Compared to stochastic loading of the tweezers via light assisted collisions from a MOT this has several advantages. First, it is possible to achieve very high occupation numbers $N \gg 1$ with relatively low power requirements per tweezer, since the temperature of the initial reservoir trap can be lower than the typical temperatures in a MOT and elastic, rather than inelastic, collisions lead to a high filling probability. This is beneficial for scaling up to hundreds or even thousands of tweezers as the large volume of the reservoir trap makes it possible to simultaneously fill many tweezers in parallel without the need for additional lasers and complex rearrangement protocols to fill empty sites. The observation that the number of atoms inside each tweezer exhibits fluctuations below the Poissonian atom shot noise limit is especially promising for quantum information processing based on small Rydberg blockaded atomic ensembles benefiting from fast collectively enhanced light-matter couplings [44, 143, 158, 159, 168].

As the understanding of optical dipole trapping is essential for these experiments, chapter 2 describes the basic principles of optical dipole traps that are based on the electric dipole interaction with far-detuned light by considering the atom as a simple oscillator to derive the main equations for optical dipole interactions that include the dipole potential and the scattering rate. Later the second half of chapter 2 also describes the basic concepts of Rydberg atoms that help us introduce the long-range interactions among the tweezer traps that extend over the distance of several micro-meters.

We have also performed Rydberg excitation of these large arrays of atomic ensembles with the spectral width of 1.47 MHz $\pm$ 0.14 MHz (chapter 5). We focus on achieving narrow-linewidth two-photon Rydberg excitation spectrum of the microscopic atomic ensembles of ^{39}K trapped in large arrays of optical tweezer traps. We identify and discuss qualitatively (section 5.3) the possible mechanisms that could broaden and limit the spectral width of the transition such as Doppler broadening, power broadening, dephasing introduced by laser linewidth, inhomegeneity in the intensity of the excitation laser due to its Gaussian profile and an indication of interaction effects between the atomic ensembles from the tweezer traps via the measurements of geometry variation (figure 5.8). Here we are still yet to understand which mechanism could be the

dominating factor contributing to the spectral broadening.

6.2 Outlook:

6.2.1 Possible improvements in the current experimental set-up

In order to achieve narrow-linewidth Rydberg excitation, the improvements such as the use of a flat-top excitation beam with uniform intensity at its cross section could be useful to provide uniform Rabi coupling experienced by the atoms within the cross section of the beam. Furthermore, the temperature of atomic ensembles should be reduced to ~ 2 μk to achieve Doppler limited linewidth of ~ 80 kHz that is approximately equal to the excitation laser linewidth. The next steps in the experiment will likely be a more systematic experimental study of the various decoherence effects summarized in table 5.1 to observe Rabi oscillations between the ground state and the Rydberg state using two-photon excitation scheme (figure 5.2) by sitting at one of the resonance peaks shown in the spectrum in figure 5.6. The overall achievement would make it possible to experimentally explore coherent quantum dynamics in this set-up for both resonant and off-resonant Rydberg excitation.

There have been many ideas for which such a system of tweezer trap arrays could be used such as atomic sensors, light-matter interactions, quantum bits, Rydberg dressed quantum matter - all with programmable atomic geometries [15]. I will discuss three more specific applications that we have been developing in Strasbourg in the following paragraphs.

6.2.2 Complex system dynamics by Rydberg facilitation:

Spatial structuring of atoms via the large arrays of optical tweezer traps opens variety of new interesting research directions, such as to study the effect of different spatial atomic distributions on the complex many-body dynamics. In reference to [134], the effect of atomic motion on disorder and reloading could become obvious when we compare a continuous trap, in which the atoms move freely throughout the volume of the trap, with a spatially structured cloud that is quasi-continuous corresponding to the condition of facilitation

but constrains the motion of atoms to smaller volumes of traps [134]. Similarly, the facilitation shell could be experimentally mapped out by tuning the period of the lattice. It could be possible to explore the effects of disorder in the facilitation dynamics in a controlled manner using the irregular structures corresponding to the facilitation shell [134]. We have begun to study some these effects in a non-structured ultracold atomic medium [97] as illustrated in the figure 6.1 reproduced from [97].

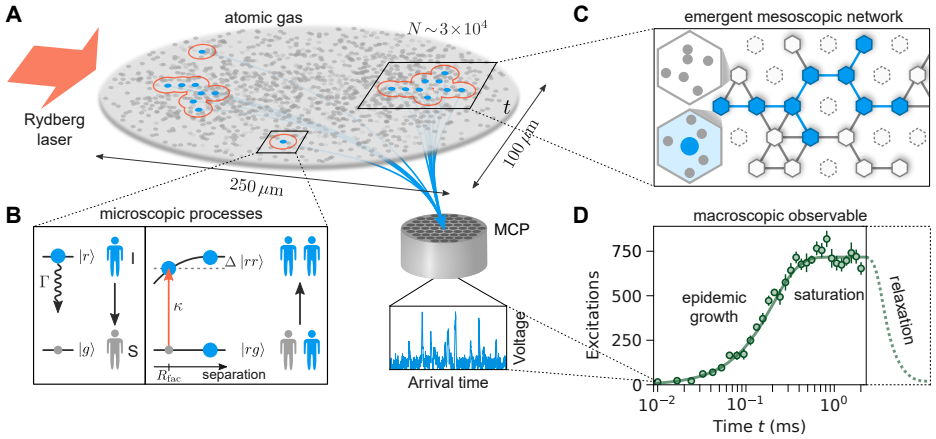

Fig. 6.1: Physical system for studying epidemic growth and dynamics on complex networks: (Image reproduced from [97]) **(A)** Experiments are performed on a two-dimensional continuous non-structured gas of potassium-39 atoms driven by an off-resonant laser field. The gas is initially prepared with a small number of seed excitations (blue disks) which then evolves according to the microscopic processes depicted in B, giving rise to growing excitation clusters that spread throughout the system. After different exposure times t, the Rydberg atoms are field ionized and detected on a microchannel plate detector (MCP), where the incident ions create voltage spikes (blue trace). **(B)** Each atom can be treated as a two-level system with a ground state $|g_i\rangle$ (gray disks) and excited Rydberg state $|r_i\rangle$ (larger blue disks). Excited atoms can decay with rate Γ or facilitate additional excitations with rate κ at a characteristic distance R_{fac} analogous to the transmission of an infection. **(C)** The dynamics of this system can be described by a susceptible-infected-susceptible (SIS) model on an emergent heterogeneous network. Each node represents a discrete cell of the coarse grained system, which can be infected (with excitation, blue) or susceptible (without excitation, white). The infection probability of each node is weighted by the number of atoms in that cell that can undergo facilitated excitation (disconnected nodes corresponding to vacant cells are depicted with dashed lines). **(D)** Exemplary data and numerical simulations (solid line) showing three different stages of dynamics: rapid growth, saturation, and eventual relaxation (data not shown). Error bars represent the standard error of the mean over typically 16 experiment repetitions.

6.2.3 Quantum simulation of energy transport

With the successful development of the platform that led us to achieve control over tailored geometries of microscopic atomic ensembles using large arrays of optical tweezer traps separated by several micrometers, we propose an approach (see figure 6.2) that could be implemented in prospective experiments that involve exciting Rydberg atoms in these tailored geometries capable of simulating energy transport with almost full control over the relevant disorder and coherence properties. The transport of charge, energy and information is fundamental to the behavior of electronic materials, complex molecules and information networks. Yet, it is still largely unknown which underlying properties of the system lead to the most efficient or robust transport, especially in the presence of quantum effects. Ultracold atoms excited to Rydberg states provide a unique approach to study fundamental energy transport processes via dipole interactions in a fully controllable environment [180]. While studies of transport

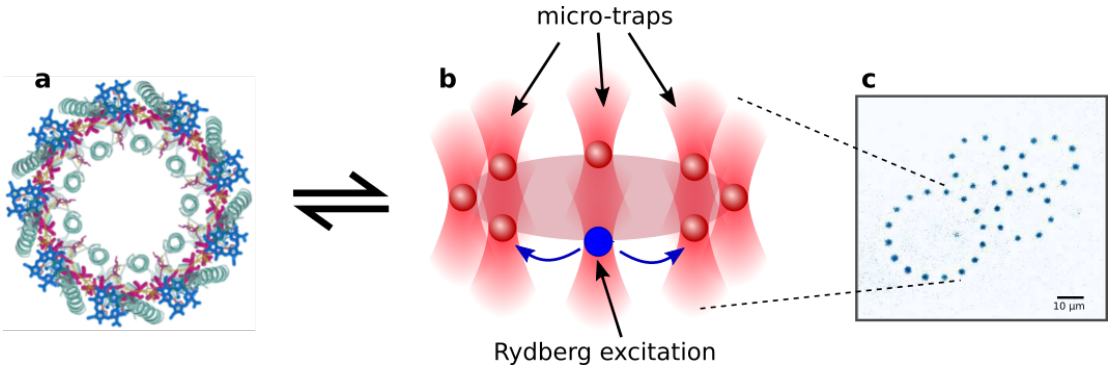

Fig. 6.2: Schematic representation of energy transport via Rydberg excitation hopping: **(a)** Molecular structure of the LH2 complex showing the ring-like arrangement of chromophores (hopping sites). **(b)** Proposed set-up of tweezer traps to simulate energy transport with controllable geometry **(c)** Experimental absorption image of a 40 site ring lattice structure, where each dark spot corresponds to a microscopic ensemble of $\approx$ 30 ultracold ^{39}K atoms. The lattice spacing is 4 μm and the apparent size of each spot is $\sim 0.75\,\mu$m ($e^{-1/2}$ radius), mostly limited by recoil blurring during imaging (reproduced from [51]).

in solids and molecules have been limited to naturally occurring interactions and disorder, Rydberg atoms experience giant electric dipole interactions which extend over much larger length and time scales than in ordinary materials. This provides the opportunity to achieve full control over the spatial and temporal configuration of hopping sites to realize physically relevant types of correlated disorder. The central questions that could be addressed are: 1) how do excitations migrate through quantum many-body system possessing non-trivial

correlations? 2) can spatially and temporally correlated noise enhance the robustness and efficiency of energy transport in synthetic quantum systems? The answers to these questions could help to find the ingredients which lead to efficient and robust energy transport as is relevant for the operation of natural and synthetic light harvesting materials. This requires a development of spatial detection scheme of the Rydberg excitations across the array of tweezer traps, similar to the high-resolution imaging setup for the atoms in the ground state. This can be done through down pumping followed by detection of ground state atoms or through the schemes of spatial detection of ions [45].

6.2.4 Experimental realisation of quantum cellular automata (QCA):

Another application would be towards studying controlled quantum dynamics. In the course of this thesis, I contributed to a theoretical proposal for quantum cellular automata (QCA) [96]. A theoretical proposal for the use of this platform of array of large tweezer traps of atomic ensembles involves the paradigm of quantum cellular automata (QCA). In case of classical cellular automata, we consider array of cells. In our case, it's a two-level system. And the evolution of each cell only depends on its neighborhood. For example, the elementary rule 150, the cell will remain the same, if the two neighbors have the same state. Otherwise, the cell will flip. At the counterpart, there lies the quantum cellular automata where the classical cell will be replaced by a qubit. The state of evolution, determined by quantum master equation, depends on including the decay process.The advantage lies in a global manipulation. So no local qubit control needed. It is an inherently parallelized operation. The key idea to implement the QCA with Rydberg array is to use multi-frequency Rydberg excitation and depumping. For simplicity, we consider one dimensional chain of tweezer, in this case. See figure 6.3 (image reproduced from [96]). V is the nearest neighbor Rydberg-Rydberg interaction. And there are two coupling fields, which consist of this frequency component, which couples transition from grand state $|g\rangle$ to Rydberg state $|r\rangle$ and also from $|r\rangle$ to an intermediate state $|e\rangle$. If the interaction V is dominant compared to the Γ and also the coupling strength ϕ and θ, then this three-level system can be reduced to effective two-level system. We did a numerical study of a nine-site system based on different QCA rules (details in [96]).

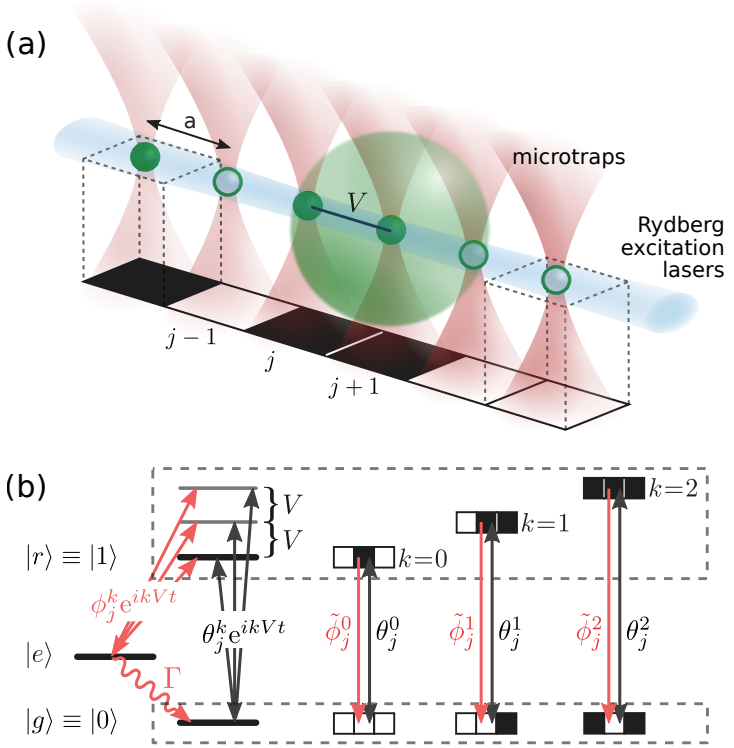

Fig. 6.3: Physical platform for quantum cellular automata based on arrays of Rydberg atoms: (Image reproduced from [96]) **(a)** Proposed setup showing a 1D array of atoms held in optical microtraps with period a and nearest-neighbor Rydberg-Rydberg interaction strength V. **(b)** Each atom can be described as a three-state system: $|g_i\rangle$ (open symbols) $|r_i\rangle$ (solid symbols) and an additional short lived state $|e_i\rangle$. The $|g_i\rangle$ to $|r_i\rangle$ and $|r_i\rangle$ to $|e_i\rangle$ transitions on site j are coupled by multifrequency fields with detunings kV and coupling strengths θ_j^k and ϕ_j^k respectively. This system can be reduced to an effective two-state system with programmable K-body interactions (shown on the right for K = 3) where the couplings θ_j^k and $\tilde{\phi}_j^k$ realize unitary (reversible) and non-unitary (dissipative) conditional interactions dependent on the number of excited neighbors k.

Referring to [134], for the application of quantum cellular automata, it is still an uanswered question if Rydberg blockaded ensembles in the superatom scenario or single atom trapped per tweezer would be beneficial because both come with challenges and advantages. The atomic ensembles permit the easier filling of the array avoiding defects such as emprty traps and under blockade picture, results in the $\sqrt{N}$ enhancement of the collective Rabi coupling [71], here N is the total atom number in the blockade [134]. Other Rydberg effects that could occur in the dense tweezer trap, such as trilobite molecules, fluctuations in the atom number between traps might cause problems [134]. Some technical improvements are still necessary in the case of unitary filling of the tweezer traps even though tweezers of single-atom offer established techniques of preparation and Rydberg excitation [134, 181]. The coherent manipulation of the atoms in the array of optical tweezer traps using Rydberg states along with the multifrequency Rydberg excitation scheme is necessary for quantum cellular automata (QCA). It is aimed to incorporate the setup of multiple radio frequencies for addressing the different states in the Rydberg level manifold [134].

In the final remarks of this thesis, I emphasize the successful demonstration of a platform of large arrays of hundreds of microscopic atomic ensembles trapped within optical tweezer traps where each tweezer has approximately uniform filling, small spatial extent and small fluctuations of the atom number between realizations. With this approach, it is possible for scaling up to hundreds or even thousands of tweezers as the large volume of the reservoir trap makes it possible to simultaneously fill many tweezers in parallel without the need for additional lasers and complex rearrangement protocols to fill empty sites. Atomic ensembles also offer enhanced Rabi coupling and greater robustness against particle loss, since the loss of one or several particles from each microtrap does not result in defects that would otherwise be difficult to repair. As a necessary pre-requisite towards the goal of performing the coherent manipulation of Rydberg excitations among these atomic ensembles, I have also presented the experiments concerning the narrow-linewidth Rydberg excitation of these arrays of microscopic atomic ensembles. I look forward to seeing how these contributions help advance the field, especially towards opening new research directions that could possibly include: study of collective light-matter coupling in interacting atomic ensembles, or for building better qubits that exploit these collective effects, simulation of quantum spin models

and complex systems with programmable disorder, exploring the role of quantum coherence in molecular quantum dynamics through quantum simulation, and harnessing quantum dynamics for engineering interesting quantum states for metrology and computing with programmable spatial configurations and versatile Rydberg mediated interactions.

Bibliography

[1] P. Kapitza, Viscosity of liquid helium below the λ-point, *Nature* **141**, 74 (1938).

[2] J. F. Allen, A. Misener, Flow of liquid helium ii, *Nature* **141**, 75 (1938).

[3] P. Nozières, D. Pines, The theory of quantum liquids, vol. ii, *Superfluid Bose Liquids* (1990).

[4] H. K. Onnes, *Proceedings of the KNAW* (1911), vol. 13, pp. 1910–1911.

[5] H. K. Onnes, Further experiments with liquid helium g. on the electrical resistance of pure metals etc. vi. on the sudden change in the rate at which the resistance of mercury disappears, *Koninklijke Nederlandse Akademie van Weteschappen Proceedings Series B Physical Sciences* **14**, 1911 (1911).

[6] F. London, H. London, The electromagnetic equations of the supraconductor, *Proc. R. Soc. Lond. A* **149**, 71 (1935).

[7] J. Bardeen, L. N. Cooper, J. R. Schrieffer, Theory of superconductivity, *Phys. Rev.* **108**, 1175 (1957).

[8] R. P. Feynman, Simulating physics with computers, *International journal of theoretical physics* **21**, 467 (1982).

[9] S. Lloyd, Universal quantum simulators, *Science* **273**, 1073 (1996).

[10] I. M. Georgescu, S. Ashhab, F. Nori, Quantum simulation, *Rev. Mod. Phys.* **86**, 153 (2014).

[11] R. Blatt, C. F. Roos, Quantum simulations with trapped ions, *Nature Phys.* **8**, 277 (2012).

[12] A. Aspuru-Guzik, P. Walther, Photonic quantum simulators, *Nature Phys.* **8**, 285 (2012).

[13] C. Gross, I. Bloch, Quantum simulations with ultracold atoms in optical lattices, *Science* **357**, 995 (2017).

[14] A. A. Houck, H. E. Türeci, J. Koch, On-chip quantum simulation with superconducting circuits, *Nature Phys.* **8**, 292 (2012).

[15] M. Morgado, S. Whitlock, Quantum simulation and computing with Rydberg qubits, *arXiv:2011.03031* (2020).

[16] I. Bloch, J. Dalibard, S. Nascimbene, Quantum simulations with ultracold quantum gases, *Nature Phys.* **8**, 267 (2012).

[17] C. A. Regal, M. Greiner, D. S. Jin, Observation of Resonance Condensation of Fermionic Atom Pairs, *Phys. Rev. Lett.* **92**, 040403 (2004).

[18] M. W. Zwierlein, *et al.*, Condensation of Pairs of Fermionic Atoms near a Feshbach Resonance, *Phys. Rev. Lett.* **92**, 120403 (2004).

[19] J. Kinast, S. L. Hemmer, M. E. Gehm, A. Turlapov, J. E. Thomas, Evidence for Superfluidity in a Resonantly Interacting Fermi Gas, *Phys. Rev. Lett.* **92**, 150402 (2004).

[20] T. Bourdel, *et al.*, Experimental Study of the BEC-BCS Crossover Region in Lithium 6, *Phys. Rev. Lett.* **93**, 050401 (2004).

[21] C. Chin, *et al.*, Observation of the pairing gap in a strongly interacting Fermi gas., *Science* **305**, 1128 (2004).

[22] D. Jaksch, C. Bruder, J. I. Cirac, C. W. Gardiner, P. Zoller, Cold bosonic atoms in optical lattices, *Phys. Rev. Lett.* **81**, 3108 (1998).

[23] M. Greiner, O. Mandel, T. Esslinger, T. W. Hänsch, I. Bloch, Quantum phase transition from a superfluid to a mott insulator in a gas of ultracold atoms, *Nature* **415**, 39 (2002).

[24] M. Köhl, H. Moritz, T. Stöferle, K. Günter, T. Esslinger, Fermionic atoms in a three dimensional optical lattice: Observing fermi surfaces, dynamics, and interactions, *Phys. Rev. Lett.* **94**, 080403 (2005).

[25] Z. Hadzibabic, P. Krüger, M. Cheneau, B. Battelier, J. Dalibard, Berezinskii-Kosterlitz-Thouless crossover in a trapped atomic gas, *Nature* **441**, 1118 (2006).

[26] R. J. Fletcher, *et al.*, Connecting berezinskii-kosterlitz-thouless and bec phase transitions by tuning interactions in a trapped gas, *Phys. Rev. Lett.* **114**, 255302 (2015).

[27] P. A. Murthy, *et al.*, Observation of the Berezinskii-Kosterlitz-Thouless phase transition in an ultracold Fermi gas, *Phys. Rev. Lett.* **115**, 010401 (2015).

[28] B. Paredes, *et al.*, Tonks–girardeau gas of ultracold atoms in an optical lattice, *Nature* **429**, 277 (2004).

[29] T. Kinoshita, T. Wenger, D. S. Weiss, Observation of a one-dimensional tonks-girardeau gas, *Science* **305**, 1125 (2004).

[30] W. D. Phillips, Nobel lecture: Laser cooling and trapping of neutral atoms, *Rev. Mod. Phys.* **70**, 721 (1998).

[31] M. A. Norcia, *et al.*, Seconds-scale coherence on an optical clock transition in a tweezer array, *Science* **366**, 93 (2019).

[32] M. Endres, *et al.*, Atom-by-atom assembly of defect-free one-dimensional cold atom arrays, *Science* **354**, 1024 (2016).

[33] D. Ohl de Mello, *et al.*, Defect-free assembly of 2D clusters of more than 100 single-atom quantum systems, *Phys. Rev. Lett.* **122**, 203601 (2019).

[34] D. Barredo, V. Lienhard, S. de Léséleuc, T. Lahaye, A. Browaeys, Synthetic three-dimensional atomic structures assembled atom by atom, *Nature* **561**, 79 (2018).

[35] R. Dumke, *et al.*, Micro-optical realization of arrays of selectively addressable dipole traps: A scalable configuration for quantum computation with atomic qubits, *Phys. Rev. Lett.* **89**, 097903 (2002).

[36] S. Bergamini, *et al.*, Holographic generation of microtrap arrays for single atoms by use of a programmable phase modulator, *J. Opt. Soc. Am. B* **21**, 1889 (2004).

[37] F. Nogrette, *et al.*, Single-atom trapping in holographic 2D arrays of microtraps with arbitrary geometries, *Phys. Rev. X* **4**, 021034 (2014).

[38] D. Barredo, S. de Léséleuc, V. Lienhard, T. Lahaye, A. Browaeys, An atom-by-atom assembler of defect-free arbitrary two-dimensional atomic arrays, *Science* **354**, 1021–1023 (2016).

[39] H. Kim, *et al.*, In situ single-atom array synthesis using dynamic holographic optical tweezers, *Nature Commun.* **7** (2016).

[40] H. Tamura, T. Unakami, J. He, Y. Miyamoto, K. Nakagawa, Highly uniform holographic microtrap arrays for single atom trapping using a feedback optimization of in-trap fluorescence measurements, *Opt. Express* **24**, 8132 (2016).

[41] M. A. Norcia, A. W. Young, A. M. Kaufman, Microscopic control and detection of ultracold strontium in optical-tweezer arrays, *Phys. Rev. X* **8**, 041054 (2018).

[42] A. Cooper, *et al.*, Alkaline-earth atoms in optical tweezers, *Phys. Rev. X* **8**, 041055 (2018).

[43] L. Anderegg, *et al.*, An optical tweezer array of ultracold molecules, *Science* **365**, 1156 (2019).

[44] M. Saffman, Quantum computing with atomic qubits and Rydberg interactions: progress and challenges, *J. Phys. B: At. Mol. Opt. Phys.* **49**, 202001 (2016).

[45] H. Labuhn, *et al.*, Tunable two-dimensional arrays of single Rydberg atoms for realizing quantum Ising models, *Nature* **534**, 667 (2016).

[46] V. Lienhard, *et al.*, Observing the space- and time-dependent growth of correlations in dynamically tuned synthetic Ising models with antiferromagnetic interactions, *Phys. Rev. X* **8**, 021070 (2018).

[47] E. Guardado-Sanchez, *et al.*, Probing the quench dynamics of antiferromagnetic correlations in a 2D quantum Ising spin system, *Phys. Rev. X* **8**, 021069 (2018).

[48] H. Kim, Y. Park, K. Kim, H.-S. Sim, J. Ahn, Detailed balance of thermalization dynamics in Rydberg-atom quantum simulators, *Phys. Rev. Lett.* **120**, 180502 (2018).

[49] T. M. Graham, *et al.*, Rydberg mediated entanglement in a two-dimensional neutral atom qubit array, *arXiv:1908.06103* (2019).

[50] S. de Léséleuc, *et al.*, Observation of a symmetry-protected topological phase of interacting bosons with Rydberg atoms, *Science* **365**, 775 (2019).

[51] Y. Wang, *et al.*, Preparation of hundreds of microscopic atomic ensembles in optical tweezer arrays, *npj Quantum Information* **6** (2020).

[52] D. Barredo, V. Lienhard, S. de Léséleuc, T. Lahaye, A. Browaeys, Synthetic three-dimensional atomic structures assembled atom by atom, *Nature* **561**, 79–82 (2018).

[53] N. Schlosser, G. Reymond, I. Protsenko, P. Grangier, Sub-poissonian loading of single atoms in a microscopic dipole trap, *Nature* **411**, 79–82 (2001).

[54] T. Grünzweig, A. Hilliard, M. McGovern, M. F. Andersen, Near-deterministic preparation of a single atom in an optical microtrap, *Nature Phys.* **6**, 951 (2010).

[55] B. J. Lester, N. Luick, A. M. Kaufman, C. M. Reynolds, C. A. Regal, Rapid production of uniformly filled arrays of neutral atoms, *Phys. Rev. Lett.* **115**, 073003 (2015).

[56] A. Kumar, T.-Y. Wu, F. Giraldo, D. S. Weiss, Sorting ultracold atoms in a three-dimensional optical lattice in a realization of Maxwell's demon, *Nature* **561**, 83 (2018).

[57] M. O. Brown, T. Thiele, C. Kiehl, T.-W. Hsu, C. A. Regal, Gray-molasses optical-tweezer loading: Controlling collisions for scaling atom-array assembly, *Phys. Rev. X* **9**, 011057 (2019).

[58] K.-N. Schymik, *et al.*, Enhanced atom-by-atom assembly of arbitrary tweezers arrays, *arXiv:2011.06827* (2020).

[59] A. N. Grigorenko, M. Polini, K. S. Novoselov, Graphene plasmonics, *Nature Photonics* **6**, 749 (2012).

[60] A. Griesmaier, J. Werner, S. Hensler, J. Stuhler, T. Pfau, Bose-einstein condensation of chromium, *Phys. Rev. Lett.* **94**, 160401 (2005).

[61] M. Lu, N. Q. Burdick, S. H. Youn, B. L. Lev, Strongly dipolar bose-einstein condensate of dysprosium, *Phys. Rev. Lett.* **107**, 190401 (2011).

[62] K. Aikawa, *et al.*, Bose-Einstein Condensation of Erbium, *Phys. Rev. Lett.* **108**, 210401 (2012).

[63] K.-K. Ni, *et al.*, A high phase-space-density gas of polar molecules, *Science* **322**, 231 (2008).

[64] J. G. Danzl, *et al.*, Reports 100 100, *Science* **321**, 1062 (2008).

[65] J. Deiglmayr, *et al.*, Formation of ultracold polar molecules in the rovibrational ground state, *Phys. Rev. Lett.* **101**, 133004 (2008).

[66] A. V. Gorshkov, *et al.*, Tunable superfluidity and quantum magnetism with ultracold polar molecules, *Phys. Rev. Lett.* **107**, 115301 (2011).

[67] B. Yan, *et al.*, Observation of dipolar spin-exchange interactions with lattice-confined polar molecules, *Nature* **501**, 521 (2013).

[68] D. Jaksch, *et al.*, Fast quantum gates for neutral atoms, *Phys. Rev. Lett.* **85**, 2208 (2000).

[69] M. D. Lukin, *et al.*, Dipole blockade and quantum information processing in mesoscopic atomic ensembles, *Phys. Rev. Lett.* **87**, 037901 (2001).

[70] E. Urban, *et al.*, Observation of rydberg blockade between two atoms, *Nature Phys.* **5**, 110 (2009).

[71] A. Gaëtan, *et al.*, Observation of collective excitation of two individual atoms in the rydberg blockade regime, *Nature Phys.* **5**, 115 (2009).

[72] T. F. Gallagher, *Rydberg atoms*, vol. 3 (Cambridge University Press, 2005).

[73] M. Saffman, K. Mølmer, Efficient multiparticle entanglement via asymmetric rydberg blockade, *Phys. Rev. Lett.* **102**, 240502 (2009).

[74] T. Amthor, C. Giese, C. S. Hofmann, M. Weidemüller, Evidence of antiblockade in an ultracold Rydberg gas, *Phys. Rev. Lett.* **104**, 13001 (2010).

[75] M. Saffman, T. G. Walker, K. Mølmer, Quantum information with rydberg atoms, *Rev. Mod. Phys.* **82**, 2313 (2010).

[76] N. Henkel, R. Nath, T. Pohl, Three-Dimensional Roton Excitations and Supersolid Formation in Rydberg-Excited Bose-Einstein Condensates, *Phys. Rev. Lett.* **104** ((2010)).

[77] G. Pupillo, A. Micheli, M. Boninsegni, I. Lesanovsky, P. Zoller, Strongly correlated gases of Rydberg-dressed atoms: Quantum and classical dynamics, *Phys. Rev. Lett.* **104** ((2010)).

[78] F. Cinti, *et al.*, Supersolid droplet crystal in a dipole-blockaded gas, *Phys. Rev. Lett.* **105** ((2010)).

[79] J. Honer, H. Weimer, T. Pfau, H. P. Büchler, Collective Many-Body Interaction in Rydberg Dressed Atoms, *Phys. Rev. Lett.* **105** ((2010)).

[80] C. Gaul, *et al.*, Resonant Rydberg-dressing of alkaline-earth atoms via electromagnetically induced transparency, *arXiv:1511.06424* ((2015)).

[81] Y.-Y. Jau, A. M. Hankin, T. Keating, I. H. Deutsch, G. W. Biedermann, Entangling atomic spins with a Rydberg-dressed spin-flip blockade, *Nature Phys.* **12**, 71 ((2015)).

[82] J. Zeiher, *et al.*, Many-body interferometry of a Rydberg-dressed spin lattice, *Nature Phys.* **12**, 1095 ((2016)).

[83] M. Płodzień, G. Lochead, J. de Hond, N. J. van Druten, S. Kokkelmans, Rydberg dressing of a one-dimensional bose-einstein condensate, *Phys. Rev. A* **95**, 043606 (2017).

[84] R. M. W. van Bijnen, T. Pohl, Quantum magnetism and topological ordering via Rydberg dressing near förster resonances, *Phys. Rev. Lett.* **114**, 243002 (2015).

[85] A. W. Glaetzle, *et al.*, Designing frustrated quantum magnets with laser-dressed Rydberg atoms, *Phys. Rev. Lett.* **114**, 173002 (2015).

[86] H. Labuhn, *et al.*, Tunable two-dimensional arrays of single rydberg atoms for realizing quantum ising models, *Nature* **534**, 667 (2016).

[87] J. Zeiher, *et al.*, Coherent many-body spin dynamics in a long-range interacting Ising chain, *Phys. Rev. X* **7**, 041063 (2017).

[88] L. Isenhower, *et al.*, Demonstration of a neutral atom controlled-NOT quantum gate, *Phys. Rev. Lett.* **104**, 010503 (2010).

[89] T. Wilk, *et al.*, Entanglement of two individual neutral atoms using Rydberg blockade, *Phys. Rev. Lett.* **104**, 010502 (2010).

[90] K. M. Maller, *et al.*, Rydberg-blockade controlled-NOT gate and entanglement in a two-dimensional array of neutral-atom qubits, *Phys. Rev. A* **92**, 022336 (2015).

[91] Y. Zeng, *et al.*, Entangling two individual atoms of different isotopes via Rydberg blockade, *Phys. Rev. Lett.* **119**, 160502 (2017).

[92] H. Levine, *et al.*, High-fidelity control and entanglement of Rydberg-atom qubits, *Phys. Rev. Lett.* **121**, 123603 (2018).

[93] H. Levine, *et al.*, Parallel implementation of high-fidelity multiqubit gates with neutral atoms, *Phys. Rev. Lett.* **123**, 170503 (2019).

[94] H. Bernien, *et al.*, Probing many-body dynamics on a 51-atom quantum simulator, *Nature* **551**, 579 (2017).

[95] A. Omran, *et al.*, Generation and manipulation of Schrödinger cat states in Rydberg atom arrays, *Science* **365**, 570 (2019).

[96] T. M. Wintermantel, *et al.*, Unitary and nonunitary quantum cellular automata with rydberg arrays, *Phys. Rev. Lett.* **124**, 070503 (2020).

[97] T. M. Wintermantel, *et al.*, Epidemic growth and Griffiths effects on an emergent network of excited atoms, *arXiv:2007.07697* (2020).

[98] K. B. Davis, *et al.*, Bose-Einstein condensation in a gas of sodium atoms, *Phys. Rev. Lett.* **75**, 3969 (1995).

[99] M. W. Zwierlein, *et al.*, Observation of Bose-Einstein condensation of molecules, *Phys. Rev. Lett.* **91**, 250401 (2003).

[100] C. H. Schunck, Y. Shin, A. Schirotzek, M. W. Zwierlein, W. Ketterle, Pairing without superfluidity: the ground state of an imbalanced Fermi mixture., *Science* **316**, 867 (2007).

[101] S. Chu, Nobel lecture: The manipulation of neutral particles, *Rev. Mod. Phys.* **70**, 685 (1998).

[102] C. N. Cohen-Tannoudji, Nobel lecture: Manipulating atoms with photons, *Rev. Mod. Phys.* **70**, 707 (1998).

[103] W. D. Phillips, Nobel lecture: Laser cooling and trapping of neutral atoms, *Rev. Mod. Phys.* **70**, 721 (1998).

[104] D. E. Pritchard, E. L. Raab, V. Bagnato, C. E. Wieman, R. N. Watts, Light traps using spontaneous forces, *Phys. Rev. Lett.* **57**, 310 (1986).

[105] A. L. Migdall, J. V. Prodan, W. D. Phillips, T. H. Bergeman, H. J. Metcalf, First observation of magnetically trapped neutral atoms, *Phys. Rev. Lett.* **54**, 2596 (1985).

[106] S. Chu, J. E. Bjorkholm, A. Ashkin, A. Cable, Experimental observation of optically trapped atoms, *Phys. Rev. Lett.* **57**, 314 (1986).

[107] R. Grimm, M. Weidemüller, Y. B. Ovchinnikov, Optical dipole traps for neutral atoms (Academic Press, 2000), vol. 42 of *Advances In Atomic, Molecular, and Optical Physics*, pp. 95 – 170.

[108] J. P. Gordon, A. Ashkin, Motion of atoms in a radiation trap, *Phys. Rev. A* **21**, 1606 (1980).

[109] M. Saffman, T. G. Walker, K. Mølmer, Quantum information with rydberg atoms, *Rev. Mod. Phys.* **82**, 2313 (2010).

[110] S. Helmrich, Phase structure and dynamics of driven-dissipative Rydberg spin systems, Ph.D. thesis, University of Heidelberg (2018).

[111] A. L. Arias Suarez, Probing the non-equilibrium dynamics and coherence properties of Rydberg-enhanced gases, Phd thesis, University of Heidelberg (2019).

[112] D. P. S. McCutcheon, N. S. Dattani, E. M. Gauger, B. W. Lovett, A. Nazir, A general approach to quantum dynamics using a variational master equation: Application to phonon-damped rabi rotations in quantum dots, *Phys. Rev. B* **84**, 081305 (2011).

[113] M. Tanasittikosol, Rydberg dark states in external fields, Phd thesis, University of Durham (2011).

[114] H.-P. Breuer, F. Petruccione, *et al.*, *The theory of open quantum systems* (Oxford University Press, 2002).

[115] G. Lindblad, On the generators of quantum dynamical semigroups, *Communications in Mathematical Physics* **48**, 119 (1976).

[116] C. Ates, T. Pohl, T. Pattard, J. M. Rost, Antiblockade in rydberg excitation of an ultracold lattice gas, *Phys. Rev. Lett.* **98**, 023002 (2007).

[117] H. Hirzler, Analysis and reduction of spectral broadening in high resolution Rydberg excitation, Master thesis, University of Heidelberg (2017).

[118] G. Gauthier, *et al.*, Direct imaging of a digital-micromirror device for configurable microscopic optical potentials, *Optica* **3**, 1136 (2016).

[119] C. Fort, Experiments With Potassium Isotopes, *Bose-Einstein Condensates and Atom Lasers* (Springer, 2002), pp. 291–300.

[120] N. Pehoviak, Strongly interacting ultracold potassium atoms via Rydberg dressing., Master thesis, University of Heidelberg (2015).

[121] T. M. Wintermantel, In-situ fluorescence imaging of ultracold potassium in an optical trap, Master thesis, University of Heidelberg (2016).

[122] S. Mezinska, Sub-Doppler spectroscopy of Rydberg states of potassium, Ph.D. thesis, University of Heidelberg (2014).

[123] J. H. Shirley, Modulation transfer processes in optical heterodyne saturation spectroscopy, *Opt. Lett* **7**, 537 ((1982)).

[124] Camy G., Borde Ch., Ducloy M., Heterodyne saturation spectroscopy through frequency modulation of the saturating beam, *Opt. Comm.* **41**, 325 (1982).

[125] G. Faraoni, Nonlinear light propagation through a strongly interacting Rydberg gas., Master thesis, Universitá di Pisa (2011).

[126] A. Sayer, Fiber-based beam-distribution-system for potassium magneto-optical traps, Bachelor thesis, University of Heidelberg (2014).

[127] C. J. Foot, *Atomic Physics* (OUP Oxford, 2005).

[128] B. Höltkemeier, 2d mot as a source of a cold atom target., Master thesis, University of Heidelberg (2011).

[129] G. Salomon, *et al.*, Gray-molasses cooling of 39K to a high phase-space density, *EPL* **104**, 63002 (2014).

[130] C. Cohen-Tannoudji, Laser cooling and trapping of neutral atoms: theory, *Physics Reports* **219**, 153 (1992).

[131] G. Salomon, *et al.*, Gray-molasses cooling of 39K to a high phase-space density, *EPL* **104**, 63002 (2013).

[132] D. Nath, R. K. Easwaran, G. Rajalakshmi, C. S. Unnikrishnan, Quantum-interference-enhanced deep sub-doppler cooling of ^{39}k atoms in gray molasses, *Phys. Rev. A* **88**, 053407 (2013).

[133] T. M. Wintermantel, In-situ fluorescence imaging of ultracold potassium in an optical trap, *Master thesis, University of Heidelberg* **3**, 556 (2016).

[134] T. M. Wintermantel, Complex systems dynamics in laser excited ensembles of rydberg atoms, Ph.d. thesis, University of Heidelberg (2020).

[135] V. GmbH, SuperSpeed V-Modules. Library Catalog: www.vialux.de.

[136] D. Petter, Spatial modulation of light for ultracold gas experiments with erbium atoms p. 88 (2015).

[137] P. P. J. Zupancic, Dynamic holography and beamshaping using digital micromirror devices, Master thesis, Ludwig-Maximilians-Universitat Munchen (2013).

[138] C. Palmer, Diffraction Grating Handbook, *Newport Corporation* p. 271 (2002).

[139] Standard Precision Aspheres SPA. CATALOG 2015.

[140] K. Viebahn, M. Sbroscia, E. Carter, J.-C. Yu, U. Schneider, Matter-wave diffraction from a quasicrystalline optical lattice, *Phys. Rev. Lett.* **122**, 110404 (2019).

[141] A. W. Glaetzle, *et al.*, Quantum spin-ice and dimer models with Rydberg atoms, *Phys. Rev. X* **4**, 041037 (2014).

[142] R. M. W. van Bijnen, T. Pohl, Quantum magnetism and topological ordering via Rydberg dressing near Förster resonances, *Phys. Rev. Lett.* **114**, 243002 (2015).

[143] S. Whitlock, A. W. Glaetzle, P. Hannaford, Simulating quantum spin models using Rydberg-excited atomic ensembles in magnetic microtrap arrays, *J. Phys. B: At. Mol. Opt. Phys.* **50**, 074001 (2017).

[144] M. Kiffner, E. O'Brien, D. Jaksch, Topological spin models in Rydberg lattices, *Appl. Phys. B* **123**, 46 (2017).

[145] F. Letscher, D. Petrosyan, M. Fleischhauer, Many-body dynamics of holes in a driven, dissipative spin chain of Rydberg superatoms, *New J. Phys.* **19**, 113014 (2017).

[146] J. Zeiher, *et al.*, Coherent many-body spin dynamics in a long-range interacting Ising chain, *Phys. Rev. X* **7**, 041063 (2017).

[147] S. de Léséleuc, *et al.*, Observation of a symmetry-protected topological phase of interacting bosons with Rydberg atoms, *Science* **365**, 775 (2019).

[148] G. Günter, *et al.*, Observing the dynamics of dipole-mediated energy transport by interaction-enhanced imaging, *Science* **342**, 954 (2013).

[149] F. Robicheaux, N. M. Gill, Effect of random positions for coherent dipole transport, *Phys. Rev. A* **89**, 053429 (2014).

[150] D. Barredo, *et al.*, Coherent excitation transfer in a spin chain of three Rydberg atoms, *Phys. Rev. Lett.* **114**, 113002 (2015).

[151] H. Schempp, G. Günter, S. Wüster, M. Weidemüller, S. Whitlock, Correlated exciton transport in Rydberg-dressed-atom spin chains, *Phys. Rev. Lett.* **115**, 093002 (2015).

[152] D. W. Schönleber, A. Eisfeld, M. Genkin, S. Whitlock, S. Wüster, Quantum simulation of energy transport with embedded Rydberg aggregates, *Phys. Rev. Lett.* **114**, 123005 (2015).

[153] M. Płodzień, T. Sowiński, S. Kokkelmans, Simulating polaron biophysics with Rydberg atoms, *Sci. Rep.* **8**, 9247 (2018).

[154] S. Whitlock, H. Wildhagen, H. Weimer, M. Weidemüller, Diffusive to nonergodic dipolar transport in a dissipative atomic medium, *Phys. Rev. Lett.* **123**, 213606 (2019).

[155] F. Yang, S. Yang, L. You, Quantum transport of Rydberg excitons with synthetic spin-exchange interactions, *Phys. Rev. Lett.* **123**, 063001 (2019).

[156] I. I. Beterov, *et al.*, Quantum gates in mesoscopic atomic ensembles based on adiabatic passage and Rydberg blockade, *Phys. Rev. A* **88**, 010303 (2013).

[157] M. Ebert, M. Kwon, T. G. Walker, M. Saffman, Coherence and Rydberg blockade of atomic ensemble qubits, *Phys. Rev. Lett.* **115**, 093601 (2015).

[158] E. Brion, K. Mølmer, M. Saffman, Quantum computing with collective ensembles of multilevel systems, *Phys. Rev. Lett.* **99**, 260501 (2007).

[159] T. M. Wintermantel, *et al.*, Unitary and nonunitary quantum cellular automata with rydberg arrays, *Phys. Rev. Lett.* **124**, 070503 (2020).

[160] C. Muldoon, *et al.*, Control and manipulation of cold atoms in optical tweezers, *New J. Phys.* **14**, 073051 (2012).

[161] G. Reinaudi, T. Lahaye, Z. Wang, D. Guéry-Odelin, Strong saturation absorption imaging of dense clouds of ultracold atoms, *Opt. Lett.* **32**, 3143 (2007).

[162] C. F. Ockeloen, A. F. Tauschinsky, R. J. C. Spreeuw, S. Whitlock, Detection of small atom numbers through image processing, *Phys. Rev. A* **82**, 061606 (2010).

[163] D. Comparat, *et al.*, Optimized production of large Bose-Einstein condensates, *Phys. Rev. A* **73**, 043410 (2006).

[164] S. Whitlock, C. F. Ockeloen, R. J. C. Spreeuw, Sub-poissonian atom-number fluctuations by three-body loss in mesoscopic ensembles, *Phys. Rev. Lett.* **104**, 120402 (2010).

[165] B. D. Esry, C. H. Greene, J. P. Burke, Recombination of three atoms in the ultracold limit, *Phys. Rev. Lett.* **83**, 1751 (1999).

[166] Y. O. Dudin, L. Li, F. Bariani, A. Kuzmich, Observation of coherent many-body Rabi oscillations, *Nature Phys.* **8**, 790 (2012).

[167] J. Zeiher, *et al.*, Microscopic characterization of scalable coherent Rydberg superatoms, *Phys. Rev. X* **5**, 031015 (2015).

[168] M. Ebert, *et al.*, Atomic Fock state preparation using Rydberg blockade, *Phys. Rev. Lett.* **112**, 043602 (2014).

[169] T. Weber, *et al.*, Mesoscopic Rydberg-blockaded ensembles in the super-atom regime and beyond, *Nature Phys.* **11**, 157 (2015).

[170] C. Schweiger, Laser excitation of ultracold potassium Rydberg atoms, Ph.D. thesis, University of Heidelberg (2015).

[171] E. D. Black, An introduction to Pound-Drever-Hall laser frequency stabilization, *American Journal of Physics* **69**, 79 (2001).

[172] M. Koppinger, Creation of ultracold RbCs molecules, Ph.d. thesis, Durham University (2014).

[173] R. Löw, *et al.*, An experimental and theoretical guide to strongly interacting rydberg gases, *Journal of Physics B: Atomic, Molecular and Optical Physics* **45**, 113001 (2012).

[174] P. Schauß, *et al.*, Observation of spatially ordered structures in a two-dimensional Rydberg gas, *Nature* **491**, 87 (2012).

[175] C. S. Hofmann, *et al.*, An experimental approach for investigating many-body phenomena in Rydberg-interacting quantum systems, *Frontiers of Physics* **9**, 571 (2014).

[176] H. J. Metcalf, P. v. d. Straten, P. v. d. Straten, *Laser Cooling and Trapping*, Graduate Texts in Contemporary Physics (Springer-Verlag, New York, 1999).

[177] N. Šibalić, J. D. Pritchard, C. S. Adams, K. J. Weatherill, ARC: An open-source library for calculating properties of alkali Rydberg atoms, *Computer Physics Communications* **220**, 319 (2017).

[178] E. A. Goldschmidt, *et al.*, Anomalous broadening in driven dissipative Rydberg systems, *Phys. Rev. Lett.* **116**, 113001 (2016).

[179] J. T. Young, *et al.*, Dissipation induced dipole blockade and anti-blockade in driven Rydberg systems, *Phys. Rev. A* **97**, 023424 (2018).

[180] G. Günter, *et al.*, Observing the dynamics of dipole-mediated energy transport by interaction-enhanced imaging., *Science (New York, N.Y.)* **342**, 954 (2013).

[181] A. Browaeys, T. Lahaye, Many-body physics with individually controlled Rydberg atoms, *Nature Phys.* **16**, 132 (2020).

Sayali SHEVATE

Preparation and Rydberg excitation of large arrays of microscopic atomicensembles

Résumé

Insérer votre résumé en français suivi des mots-clés

Des atomes froids dans des réseaux de pinces optiques sont apparus comme l'un des plates-formesles plus polyvalent es pour la physique quantique à N-corps, la simulation et l'informatiquequantiques. Dans cette thèse, je rapporte un moyen de réaliser des réseaux de pièges optiquesoccupés uniformément, de tailles bien supérieures à ~200 sites, en utilisant des collisions élastiquespar opposition aux collisions inélastiques assistées par la lumière et je fais progresserconsidérablement la faisabilité des qubits basés sur des ensembles atomiques piégés. Nousdémontrons, pour la première fois, des réseaux polyvalents entièrement remplis d'ensemblesatomiques de plus de 400 pièges optiques préparés à l'aide d'une matrice de micro-miroirs, où piègemicroscopiques contient ~60 atomes, un nombre d'atomes élevé et des fluctuations étonnammentfaibles du nombre d'atomes. En utilisant des atomes de Rydberg en forte interaction, j'étudie ladynamique d'excitation de Rydberg et les interactions à longue distance dans les grands réseauxd'ensembles atomiques. Cela ouvre la voie à la réalisation de simulateurs quantiques basés sur desensembles atomiques.

Mot-clés : atomes-froids, Rydberg, la physique quantique à N-corps, simulateurs quantiques,ensembles atomiques, pinces optiques

Résumé en anglais

Insérer votre résumé en anglais suivi des mots-clés

Ultracold atoms in optical tweezer arrays have emerged as one of the most versatile platformsfor quantum many-body physics, quantum simulation and quantum computation. In this thesis,I report a way to achieve fully occupied tweezer arrays to sizes well beyond 200 sites byexploiting elastic collisions as compared to light-assisted inelastic collisions and along the waygreatly advance the feasibility of quantum simulations based on trapped atomic ensembles withprogrammable geometries. We demonstrate, for the first time, fully filled versatile arrays ofatomic ensembles > 400 tweezers prepared using a digital micromirror device, where eachtweezer contains ~ 60 atoms in a microscopic volume, high atom number and remarkably lowatom number fluctuations. As a necessary pre-requisite to performing the coherentmanipulation of the Rydberg excitation of these atomic ensembles, I present experiments onnarrow linewidth two-photon Rydberg excitation of these large arrays of atomic ensembles. Ialso discuss an analysis of the effects causing spectral broadening. This work paves the waytowards detailed analysis of many-body effects in a structured Rydberg gas-an important steptowards building a quantum simulator based on trapped atomic ensembles in optical tweezerarrays. This opens up applications ranging from quantum simulation of exotic quantum spinmodels, quantum dynamics including transport and many-body localization and quantumcellular automata with programmable spatial configurations and versatile Rydberg mediated interactions. **Keywords** : Ultracold atoms, Rydberg, Tweezer trap.